Adsorption of Small Molecules in Advanced Material Systems

Fei Zhang

Dissertation submitted to the faculty of the Virginia Polytechnic Institute and State University in partial fulfillment of the requirements for the degree of

Doctor of Philosophy
In
Mechanical Engineering

Rui Qiao, Chair

Mark R. Paul

Jiangtao Cheng

Shengfeng Cheng

Jonathan Boreyko

05/07/2018
Blacksburg, VA

Keywords: adsorption, ionic liquids, porous liquids, molecularly sharp electrodes, molecular dynamics simulations

Adsorption of Small Molecules in Advanced Material Systems

Fei Zhang

ABSTRACT

Adsorption is an omnipresent phenomenon and plays an essential role in numerous applications including molecule separation, energy storage, catalysis, and lubrications. Developing a molecular scale understanding of adsorption is essential for the development and application of many new materials. In this dissertation, adsorption is considered for three emerging materials systems: porous liquids, room-temperature ionic liquids, and atomically sharp electrodes immersed in aqueous electrolytes. Molecular dynamics simulations are used to gain molecular insights.

First, thermodynamics and kinetics in adsorption of small gas molecules in recently synthesized porous liquids featuring crown-ether-substituted cage molecules was studied. Capacity of gas storage in cage molecules was found to be governed by the non-electrostatic (dispersive) intermolecular interactions between gas and cage molecule and size/shape of gas molecules. The cage molecule shows selectivity of CO_2 over CH_4/N_2, which revealed the potential of porous liquids in molecule separation. All gas molecules considered can enter the cage essentially without energy barriers and leave the cage rapidly by overcoming modest energy penalties.

Second, the effect of water adsorption on three-dimensional structure of mica-ionic liquid interfaces were studied. It was shown that the adsorbed water alters not only the layering of ions near mica surface but also their lateral and orientation ordering. The multifaceted impact of water on the interfacial structure of ionic liquids can be traced back

to the fact water is both a dielectric solvent and a molecular liquid. Based on additional observations that adsorption of water at mica−ionic liquid interfaces is enhanced by ionic liquids and surface charge, it was suggested that the structure of ionic liquids near solid surfaces is governed by the three-way coupling between self-organization of ions, adsorption of interfacial water, and electrification of the solid surfaces.

Finally, the adsorption of dissolved N_2 in EDLs near planar and atomically sharp electrodes was investigated. The adsorption of N_2 was found to be enriched near neutral electrode. In comparison, the adsorption of N_2 in the EDL near negatively charged electrodes was found to increase under moderate surface charge density, but decrease under high surface charge density. By analyzing PMF for N_2 molecule, the solvent-induced effects were found to play important roles in influencing adsorption of N_2. The adsorption of N_2, especially their dependence on the surface charge and curvature, was rationalized by examining the structure of interfacial water, their interference with the hydration shell of N_2, and their modification by electrification of the electrodes.

Adsorption of Small Molecules in Advanced Material Systems

Fei Zhang

GENERAL AUDIENCE ABSTRACT

Adsorption is a ubiquitous phenomenon that plays key roles in numerous applications including molecule separation, energy storage, catalysis, and lubrications. Since adsorption is sensitive to molecular details of adsorbate molecule and adsorbent materials, it is often difficult to describe theoretically. Molecular modeling capable of resolving physical processes at atomistic scales is an effective method for studying adsorption. In this dissertation, the adsorption of small molecules in three emerging materials systems: porous liquids, room-temperature ionic liquids, and atomically sharp electrodes immersed in aqueous electrolytes, are investigated to understand the physics of adsorption as well as to help design and optimize these materials systems.

Thermodynamics and kinetics of gas storage in the recently synthesized porous liquids (crown-ether-substituted cage molecules dispersed in an organic solvent) were studied. Gas molecules were found to store differently in cage molecules with gas storage capacity per cage in the following order: CO_2>CH_4>N_2. The cage molecules show selectivity of CO_2 over CH_4/N_2 and demonstrate capability in gas separation. These studies suggest that porous liquids can be useful for CO_2 capture from power plants and CH_4 separation from shale gas.

The effect of adsorbed water on the three-dimensional structure of ionic liquids [BMIM][Tf_2N] near mica surfaces was investigated. It was shown that water, as a dielectric solvent and a molecular liquid, can alter layering and ordering of ions near mica surfaces.

A three-way coupling between the self-organization of ions, the adsorption of interfacial water, and the electrification of the solid surfaces was suggested to govern the structure of ionic liquid near solid surfaces.

The effects of electrode charge and surface curvature on adsorption of N_2 molecules near electrodes immersed in water were studied. N_2 molecules are enriched near neutral electrodes. Their enrichment is enhanced as the electrode becomes moderately charged but is reduced when the electrode becomes highly charged. Near highly charged electrodes, the amount of N_2 molecules available for electrochemical reduction is an order of magnitude higher near spherical electrodes with radius ~1nm than near planar electrodes. The underlying molecular mechanisms are elucidated and their implications for development of electrodes for electrochemical reduction of N_2 are discussed.

Dedication

To my family and friends

Acknowledgments

I would like to express my sincere gratitude to my advisor Dr. Rui Qiao for his kind support and encouragement throughout my doctoral study. He inspired me in research and in life during my study in the states. His guidance and patience made this work possible. I would also like to thank the members of my committee: Dr. Mark Paul, Dr. Jiangtao Cheng, Dr. Shengfeng Cheng and Dr. Jonathan Boreyko for their time and valuable suggestions on my research and coursework.

I am very grateful to all the research collaborators, especially Dr. Bobby G. Sumpter, Dr. Jingsong Huang from Oak Ridge National Lab.

I would also like to extend my thanks to my lab mates, Dr. Xikai Jiang, Dr. Ying Liu, Dr. Yadong He, Dr. Fengchang Yang, Dr. Zhou Yu, Mr. Haiyi Wu, and Mr. Chao Fang. I have learned a lot in research from Dr. Yadong He at the beginning of my doctoral research.

I would like to thank the National Science Foundation for financial support, the Advanced Research Computing at VT for computing resources, and the staffs at the mechanical engineering department and graduate school for kind help.

Last but not least, I would like to thank my family for their love and support.

Table of Contents

Chapter 1: Introduction **1**

1.1 Concept and Applications of Adsorption **1**

1.1.1 Basic concept 1

1.1.2 Applications 2

1.2 Theoretical studies of adsorption **4**

1.2.1 Theoretical models of adsorption 4

1.2.2 Limitations of theoretical adsorption models 6

1.3 Molecular simulations for adsorption **7**

1.3.1 Monte Carlo molecular simulations 7

1.3.2 Molecular dynamics simulations 10

1.4 Emerging material systems and issues related to adsorption **14**

1.4.1 Gas storage in porous liquids 14

1.4.2 Water adsorption at mica-ionic liquid interfaces 17

1.4.3 N_2 adsorption near atomically sharp electrodes 19

1.5 Outline of the dissertation work **21**

Chapter 2: Thermodynamics and Kinetics of Gas Storage in Porous Liquids **23**

2.1 Introduction **23**

2.2 Simulation System and Methods **25**

2.3 Results and Discussion **28**

2.3.1 Capacity and mode of gas storage. 28

2.3.2 Kinetics of gas storage. 34

2.4 Conclusions **36**

Chapter 3: Multi-Component Gas Storage in Organic Cage Molecules **38**

3.1 Introduction **38**

3.2 Simulation System and Methods **41**

3.3 Results and Discussion **45**

3.3.1 Cage molecule's accessible space 45

3.3.2 Storage of pure gas molecules. 46
3.3.3 Storage of multi-component gas molecules. 48
3.4 Conclusion 54
Chapter 4: Effects of Water on Mica-Ionic Liquid Interfaces 57
4.1 Introduction 57
4.2 Simulation System, Models, and Methods 61
4.3 Results and Discussion 64
4.3.1 Interfacial structure near neutral mica surfaces 64
4.3.2 Interfacial structure near charged mica surfaces 70
4.3.3 A general picture of ionic liquid structure near "wet" surfaces 78
4.4 Conclusions 80
Chapter 5: Adsorption of Molecular Nitrogen in Electrical Double Layers near Planar and Atomically Sharp Electrodes 83
5.1 Introduction 83
5.2 Simulation Systems, Models, and Methods 87
5.3 Results and Discussion 90
5.3.1 Macroscopic N_2 adsorption behavior in EDLs 90
5.3.2 Molecular details of N_2 adsorption near planar electrodes 93
5.3.3 Molecular details of N_2 adsorption near spherical electrodes 104
5.4 Conclusions 106
Chapter 6: Summary of Contributions 109
Appendix A: Supporting Information for Chapter 2 115
Appendix B: Supporting Information for Chapter 3 118
Appendix C: Supporting Information for Chapter 4 120
Appendix D: Supporting Information for Chapter 5 125
Reference 127

Chapter 1: Introduction

1.1 Concept and Applications of Adsorption

1.1.1 Basic concept

Adsorption generally refers to the enrichment of one material (termed *adsorbate*) near the surface of another material (termed *adsorbent*). Adsorption occurs, almost inevitably, when an adsorbent (often with a continuous surface) is exposed to atoms, ions, molecules, or cluster of particles, either in the gas or the liquid phase.[1] A concept closely related to adsorption is absorption. The key difference is that adsorption is a surface phenomenon when adsorbates come into contact with adsorbents, but absorption is a bulk phenomenon when one material is dispersed into another material (see Figure 1-1). While adsorption almost always occurs in practical material systems, the extent of adsorption in a specific system depends on adsorbents' surface characteristics, adsorbates' properties, and external conditions such as temperature and adsorbate concentration.

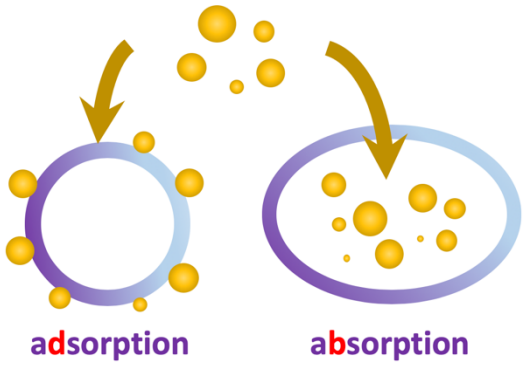

Figure 1-1. Difference between adsorption and absorption. The thick black lines denote surface of the absorbent.

Understanding the mechanism of adsorption is essential for numerous applications, e.g., gas separation and storage, purification, and catalysis,[2-10] to name just a few. Fundamentally, adsorption is largely driven by the interactions between adsorbates and adsorbents. Their interactions can involve physical and chemical forces.[11] Examples of the physical forces include the van der Waals force and the electrostatic force. The latter can arise between charges, between charges and dipoles, between dipoles, or between other charged entities, e.g., an ion and a CO_2 molecule can interact through the charge-quadrupole interactions. Chemical forces include covalent bonding, π-π stacking, etc, and usually involves quantum effects. Some interactions between molecules, e.g., the hydrogen bonding between water molecules, can involve both physical and chemical origins. Generally speaking, physical forces are weaker than chemical forces. Depending on which type of these forces dominate the adsorbate-adsorbent interactions, adsorption can be classified as the physisorption and the chemisorption.

1.1.2 Applications

Adsorption, an omnipresent process, is of great technological importance. Similar to absorption, the applications of adsorption can involve either the removal of some molecules ('foe') or the enrichment of certain molecules ('friends').

The applications of adsorption in the removal of target substances from liquid phase can be traced back to at least 2000 years ago, when ancient Hindus and Phoenicians used charcoal, a highly porous material with large specific surface area, to purify water. Today, adsorption is still considered a superior method for water purification in some wastewater treatment situations. The applications for adsorption, however, have expanded far beyond

liquid purification, e.g., adsorption is now widely used in gas separation for applications such as odor removal and flue gas treatment in traditional fuel power plant.

Adsorption is also widely used to enrich target substances on the surface of adsorbents. For example, it was proposed to use CO_2 to displace shale gas/oil from shale formations so that gas/oil is extracted while CO_2 is sequestered into the shale formation.[12] Such a concept makes use of the strong adsorption of CO2 on shale's interior surfaces and simultaneously reduces CO_2 release and enhances hydrocarbon extraction. Another example of application of adsorption in the form of enriching target molecules is the hydrogen storage. One of the keys to popularize the use of hydrogen as a clean energy carrier is the development of safe, efficient, and low-cost hydrogen storage systems. Among the materials developed in the past decades, metal-organic frameworks (MOFs)[13-16] (see Figure 1-2) have shown significant promise due to their large surface area and high specific adsorption capacity.

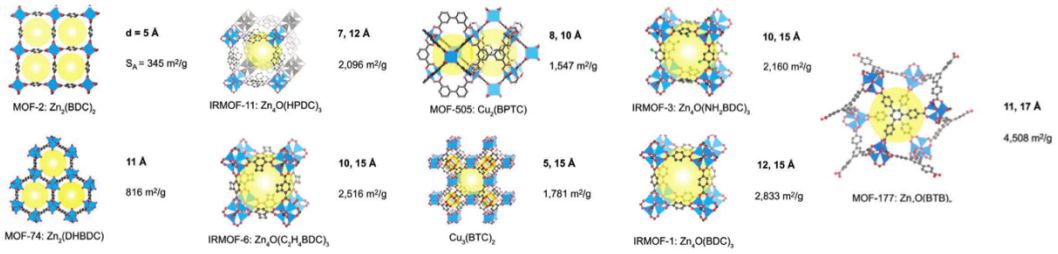

Figure 1-2. Crystal structures of MOFs examined for CO2 storage capacity at room temperature. For each MOF, the framework formula, pore size, and surface area are given. This figure is reproduced from Ref. [17].

In addition to the above two classes of applications, adsorption also plays a key role in numerous other applications. For example, in heterogeneous catalysis, the reaction of the reactant molecules takes place at solid-liquid or solid-gas interfaces. Adsorption of reactant molecules at these interfaces, the first step in a catalytic cycle, often dictates the efficacy of the catalyst.[18] When molecules are adsorbed onto surface, they can form mono-layer or even multi-layer structures, which can significantly modify the structure of the

adsorbent's surface. Therefore, adsorption can also be leveraged for surface modification. For example, the adsorption of water molecules on beta-alumina solid electrolyte's surface and their subsequent penetration into the electrolyte are known to reduce their ion conductivity.[19]

1.2 Theoretical studies of adsorption

Because of its ubiquity and technological importance, adsorption has been studied for centuries. Here, some of the key advances in the theoretical studies of adsorption research are surveyed and their limitations discussed.

1.2.1 Theoretical models of adsorption

The early study of adsorption mainly focuses on developing analytical models. In 1909, Herbert Freundlich proposed an empirical equation, known as the Freundlich equation to relate the amount of adsorption on an adsorbent surface to the concentration of adsorbates in the contacting fluid phase.[20] In 1916, Polanyi published the Polanyi adsorption potential theory. His theory assumes that the attraction between gas and surface is due to the van der Waals forces and gas behaves as ideal gas before condensation. The adsorption isotherm is then worked out based on the chemical potential difference between the gas on the surface and far away from the surface.[21] Polanyi's theory has been recognized as a powerful model for vapor adsorption on energetically heterogeneous solid surfaces. Quite recently, Manes and co-workers related liquid-phase and vapor-phase adsorption and extended the Polanyi theory from the vapor-phase to the liquid-phase (Polanyi-Manes model).[22-23]

Parallel to the Polanyi theory, in 1918, Langmuir considered the adsorption of gases or vapors on a planar surface with a fixed number of identical active (adsorption) sites and proposed a model for monolayer and sub-monolayer adsorption on energetically homogeneous surface, which is later known as the Langmuir model. In his model, the adsorbate molecules are assumed to behave as ideal gas and the net adsorption is determined by the competition between the adsorption and desorption under isothermal conditions.[24] Aiming to elucidate the physical adsorption of gas molecules on a solid surfaces, in 1938, Brunauer, Emmett, and Teller proposed the Brunauer–Emmett–Teller (BET) theory[25], which extends Langmuir's theory from monolayer adsorption to multilayer adsorption based on statistical analysis on the adsorption sites. To date, the BET theory remains the standard approach for surface area calculation of porous solids.

The kinetics of adsorption is another key topic in adsorption research. Many models have been developed to delineate the reaction and diffusion process in adsorption.[26] In 1898, Lagergren presented a first-order rate equation to describe the kinetics of liquid-solid phase adsorption, which is one of the earliest works to relate the adsorption rate to the adsorption capacity.[27] In 1934, Zeldowitsch established a kinetic equation of chemisorption, Elovich's equation, and it was later applied to describe adsorption of carbon monoxide on manganese dioxide, where an exponential decrease of gas adsorption was observed with increasing in the adsorbate.[28] As an extension of first-order rate equation, Ho *et al*. assumed that the adsorption may be a second-order kinetic process, which was later widely applied in soil reactions.[29-30] For the kinetics of physical adsorption, model was developed to illustrate the process of film and/or intraparticle diffusion. In 1947, Boyd et al. experimentally revealed two processes governing the adsorption rate: at high

adsorbate concentration, adsorption is controlled by diffusion in and through adsorbent particles; at low adsorbate concentration, adsorption is controlled by diffusion through a liquid film at the periphery of particles.[31] They also presented equations to describe the film diffusion rate and successfully modeled several liquid/solid adsorption systems. Another film diffusion model is the linear driving force-rate law, which is based on the mass balance law and equates the rate of solute accumulation at solid surface to solute transfer across the liquid film.[32] In addition to the film diffusion models, intraparticle diffusion model, which deals with diffusion-adsorption inside particles, have also been developed. Typical intraparticle diffusion model includes homogeneous solid diffusion model, Web-Morris model, and Dumwald-Wagner model. Details of the intraparticle diffusion models can be found in the review of Ref. [26].

1.2.2 Limitations of theoretical adsorption models

Although many models and theories have been developed to describe and explain adsorption process, it remains a challenging task to predict adsorption from first principles, especially when new materials are involved. As an example, consider the adsorption of small molecules in microporous materials. The large amounts of molecule-sized pores make them perfect candidate for applications in adsorption storage, molecule separation, and chemical catalysis. The confined space in these pores leads to complicated physical and chemical mechanisms governing the adsorption of molecules, which is exceedingly difficult to describe using existing analytical theories. This is especially true when the adsorbate has complex structures and when multi-component adsorption is involved. To further compound the difficulty in predicting the adsorption behavior, there are numerous classes of microporous materials and each class further has many, sometimes almost

unlimited varieties. For example, MOFs, as a new class of porous materials, has attracted much attention in the past 30 years.[33] Consisted of metal ions or clusters coordinated to organic ligands, MOFs can have numerous variations in their structure, and consequently different adsorption behavior. Exploring the adsorption behavior of all the existing MOFs experimentally is a mission that can hardly be accomplished, and predicting the adsorption in these materials using a single or several theories is equally challenging.

A key reason that many theories are not highly effective for predicting the adsorption is that the molecular level details of the adsorbent and adsorbate are not easily incorporated into these theories, despite that these details largely govern the adsorption. While these details are naturally considered in experimental studies, these studies do not directly reveal the molecular mechanisms behind the observed adsorption behavior, thus may not offer the insight needed for the rational design and optimization of new materials.

1.3 Molecular simulations for adsorption

The limitations of experimental and theoretical methods on adsorption call for new methods for studying adsorption. In the past decades, molecular simulations have emerged as a powerful tool for studying adsorption. Molecular simulations can be considered as computer "experiments" in which the chemical structure of molecules and the interactions between molecules are explicitly described (often in the form of pair interactions). The two most important class of molecular simulations are the Monte Carlo (MC) simulations and the molecular dynamics (MD) simulations.[34] In this section, previous MC and MD research on adsorption is briefly reviewed to highlight their power for understanding adsorption.

1.3.1 Monte Carlo molecular simulations

MC simulations sample the equilibrium states (configurations) of molecular systems.[34] An MC move is formulated in each step and the energy of system is computed. The move is then accepted or rejected according to the Boltzmann distribution. Thermodynamic properties of the molecular system (e.g., adsorption) can then be derived from the collected configurations. Among all ensembles in MC simulations, the grand-canonical ensemble[35] is the most frequently used one for studying adsorption. In such simulations, usually termed GCMC simulations, the number of adsorbate molecules in the adsorbent can be directly computed by specifying the chemical potential of the adsorbate molecules, temperature, *etc*.

In early years, MC simulations were used to predict the conformation of polymers adsorbed on solid surfaces. McCrackin simulated the configurations of adsorbed polymer molecules with excluded volume on a four-choice simple cubic lattice and found the critical adsorption energy for polymer to lie on the surface to be $0.25k_BT$.[36] Eisenriegler *et al*. studied the effect of hard wall on the configurations of long polymer chains in the presence of short-range attractive forces. They developed a new sampling technique with a bias in favor of adsorbed polymer configurations.[37] Their result from MC studies of self-avoiding walks on tetrahedral lattices with a free surface confirmed the scaling theory of polymer statistics.

Later, MC simulations found broader applications in adsorption research. In 1981, Soto reported a GCMC simulation of adsorption in zeolite molecular sieves.[38] By taking both dispersion and electrostatic energies in zeolite cavities into consideration, their work highlighted the importance of heterogeneity in zeolite and intermolecular forces between adsorbate molecules in controlling the adsorption. In 1989, Finn used an isobaric-

isothermal MC simulation method to investigate the wetting process of fluid Ar near solid CO_2.[39] They presented the first conclusive evidence for prewetting in a continuum system and the results are in qualitative agreement with the predictions of density-functional and related theories of wetting phenomena. In 1994, Delville simulated the adsorption of vapor on the clay surfaces using MC, where strong hydration force exists.[40] It was found that the wettability of the clay minerals is related to their surface charge and chemical compositions and a moderate decrease in the clay-water interactions can lead to remarkable difference in the clay's wetting performance. In some applications, the adsorbents and adsorbates can carry charges and strong electrostatic interactions control the adsorption behavior. For example, Yamakov et al. studied the adsorption of charged polymer chain on an oppositely charged surface using off-lattice MC simulations in 1999.[41] Their simulations provided the first verification of the scaling laws of the polyelectrolyte adsorption with various chain ionization and salt contents.

While early MC simulations generally predict the qualitative features of adsorption and scaling laws, MC simulations have matured greatly since the early 80's and can now be used to guide the design of molecular materials for adsorption. In particular, the adsorption of hydrogen and other small molecules in carbon nanomaterials,[42-45] zeolites,[46-50] and MOFs has been extensively studies in recent years.[13, 51-52] For example, Yang performed GCMC simulations in combination with density function theory calculations to study the adsorption of hydrogen in MOF-505.[53] The simulations revealed that hydrogen molecules prefer sites with metal-oxygen clusters and provided evidence for the favorable impact of open metal sites on hydrogen adsorption. Dubbeldam *et al*. explored MOFs for separation of alkanes using GCMC simulations.[54] Using a general tunable pore structure,

they demonstrated the possibility of "molecular traffic control", where different molecular species in a mixture diffuse preferentially along different directions based on their properties. More recently, Li *et al*. reported an uncommon carboxyl-decorated MOF for selective gas adsorption and catalytic conversion of CO_2 and confirmed multiple CO_2- and C_2H_6-phillic sites in the newly synthesized MOF using GCMC simulations.[55]

1.3.2 Molecular dynamics simulations

MD generate configurations (or trajectories) of a molecular system using determining laws (e.g., Newton's law).[34] Usually, the interactions between molecules are described by empirical force fields and the trajectories are propagated in time. Therefore, different from the MC simulations, MD simulation can provide information on the dynamic evolution of the molecule systems investigated. MD simulations were first reported in the 70's and have since become a major tool in understanding molecular and interfacial phenomena. Below their application in adsorption research is briefly reviewed.

In 1980, Severin and Tildesley simulated a single methane molecule adsorbed on a graphite surface.[56] Their work extended the use of MD simulations from homogeneous bulk phase to the modeling of interfaces between phases. The height of the monolayer above the surface were predicted by an effective pairwise potential, and both translational and rotational dynamics of the methane molecules were described. Later in 1985, Tildesley and Talbot continued their work to perform a series of simulations of fluid N_2 on graphite in the microcanonical ensemble. Their simulations revealed the translational structure of N_2 fluid with respect to the graphite surface and reproduced the isosteric enthalpy measured in experiments.[57]

Since then, MD simulations found many applications in adsorption related researches. In 1987, Sikkenk *et al*. studied wetting and drying at solid-fluid interfaces for Lennard-Jones fluids and identified both wetting and drying phase transition for the first time in simulations.[58] In 1995, Langel and Parrinello presented their *ab initio* MD simulation of water adsorption on MgO slabs,[59] which made it a popular method for studying adsorbed molecules.[60-62]. Their simulations showed that, under comparable conditions, physisorption is only observed on the (001) plane of solid MgO, which verified that disordered surfaces are more active in the dissociation of water molecules.

While early MD simulations focused on adsorption on planar surfaces, they soon found applications in microporous materials. Magda *et al.* studied narrow, liquid-filled pores in 1988.[63] The multi-layer adsorption structure was indicated by the density profile, and solvation forces and self-diffusion coefficient were computed. In 1990, Grofalini studied water adsorption on silicate glasses, which demonstrated the power of probing surface property changes through MD simulations.[64] In 1991, Yashonath *et al*. studied the temperature and concentration dependence of adsorption properties of methane in NaY zeolite using MD simulations.[65] Methane molecules was found to preferentially occupy the region near the inner surface of the α-cage, which is a general characteristic of adsorption in faujasites irrespective of methane molecules. Later, Sarkisov and Monson modeled the adsorption-desorption process in mesoporous materials, in which the pore geometries were chosen to test the classical theories of hysteresis in adsorption.[66] It was shown that MD simulations can be used to test many classical concepts of adsorption and desorption in simple pore geometries. It was shown that the adsorption computed by MD simulations matched that computed in GCMC simulations in all the pore geometries examined.

Most recently, as MOFs becomes one of the most popular porous material platforms, adsorption in them has been extensively studied by MD simulations. In 2004, Skoulidas first studied the diffusion of Argon adsorbed in CuBTC and reported that the structural similarity of CuBTC and silica zeolites leads to similar gas diffusion behavior in terms of their strength-, concentration-, and temperature-dependence.[67] MD simulations are often used to investigate self-diffusion and transport diffusion of molecules adsorbed in MOFs.[68-70] In addition to classical MD simulations, *ab initio* MD simulations are also being used to probe the adsorption in MOFs. For example, Cheng *et al*. used such type of simulations to provide a molecular picture of the breathing behavior of MIL-53(Sc), which combines "regularity" with "softness" by exhibiting reversible deformations in response to external stimuli.[71] The nature of structural responses of MIL-53(Sc) was revealed and the energetic behind the structure response was clarified.

In all the adsorption simulations surveyed above, the adsorption of molecules occurs in a "gas" phase in the sense that there are no solvent molecules to compete with the adsorbate molecules for adsorption. In practice, the adsorption of molecules on a surface immersed in liquids is also widely encountered and plays important role in problems such as bubble nucleation. An important case of this type of adsorption phenomenon that has been studied extensively is the ion adsorption near electrified surfaces. When an electrified surface is brought into contact with an electrolyte, the counter-ions (co-ions) are attracted to (repelled from) the surface and an electrical double layer (EDL), in which charge neutrality is broken, appears (see Figure 1-3). The ion adsorption in the EDL plays a foundational role in a host of electrochemical problems, e.g., electrochemical reactions, capacitive energy storage, to name just two.

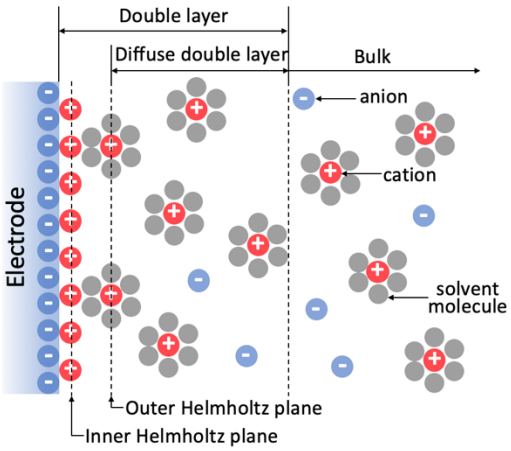

Figure 1-3. A schematic representation of the electrical double layer (EDL) near an electrode.

After earlier investigations of water adsorption on neutral platinum electrodes[72-73] and between charged mica and lecithin layers,[74-75] Glosli and Philpott studied the ion adsorption near charged surface using a simple model in 1992.[76] Their work gave microscopic insight on how ions and water molecules distribute (and orient, in the case of water molecules) in presence of an electric field and demonstrated the capability of MD simulation in revealing many aspects of EDLs. Later in 1995, Philpott *et al*. examined the structure and dynamics of EDLs in aqueous electrolytes near electrode and further showed MD simulations to be a powerful tool to qualitatively reproduce many aspects of electrochemical interfaces.[77]

After the pioneering works in the 1990s, MD simulations of the ion adsorption near electrified interfaces received relatively less attention compared to simulation of adsorption in other systems. However, research on adsorption near electrified interfaces experienced a resurgence since the 2009, largely because of the surging interest in supercapacitors, especially those based on room-temperature ionic liquids (RTILs). In particular, the work by Fedorov and Kornyshev ushered a decade of intensive research on the EDLs in RTILs. In their pioneering work, they probed the effects of ion size asymmetry on the structure and capacitance of the EDLs in RTILs by performing MD simulation of a model RTIL

confined between two electrodes.[78] Their simulations qualitatively reproduced the asymmetric "bell-shape" character of capacitance-voltage curve reported experimentally and provided a basis for rationalizing the capacitance behavior in EDLs formed by more sophisticated, realistic RTILs. Shortly after, Feng *et al*. simulated the EDLs at the interface of an RTIL [BMIM][NO_3] and planar electrodes. They characterized the interfacial ion structure and capacitance at various surface charge density, and qualitatively reproduced the concave capacitance-voltage curve reported in many experimental studies.[79] Their simulations revealed a Helmholtz-like interfacial counterion layer in addition to the alternating layering of counter-ions and co-ions near the electrode. It was found that the smaller $[NO_3]^-$ ions dominate the response of the EDL structure to the change of surface charge density, both near the positive and negative electrodes. The above papers were followed by an explosive growth of research on the EDLs in RTILs and a comprehensive review of the related progress can be found in several review papers.[80-82]

1.4 Emerging material systems and issues related to adsorption

The ever increasing demand from engineering applications drives the development of new materials. Many applications of the newly emerged materials are related to adsorption of small molecules in them. In this dissertation, the adsorption of small molecules in several advanced materials (porous liquids, ionic liquids, and atomically sharp electrodes) has been investigated using molecular dynamics simulations to elucidate the mechanisms behind the adsorption behavior in these materials.

1.4.1 Gas storage in porous liquids

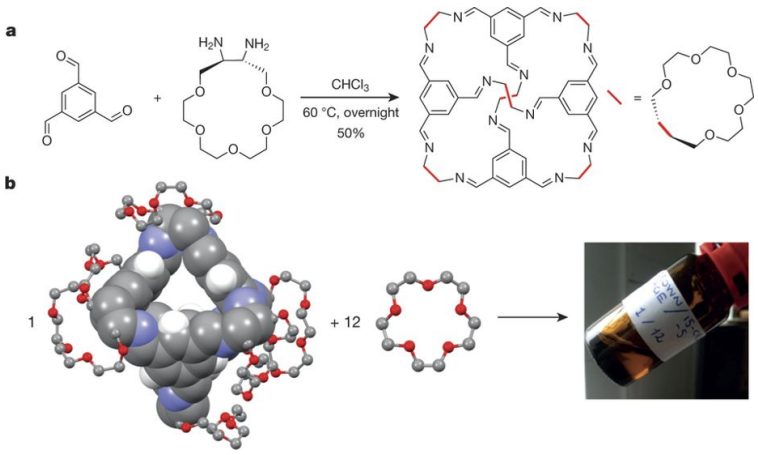

Figure 1-4. a. Synthesis of the crown-ether cage. **b**. The empty, highly soluble cage molecule (left) defines the pore space; the 15-crown-5 solvent (middle) provides fluidity but cannot enter the cage cavities. The concentrated solution (porous liquid) flows at room temperature (right). The figure is reproduced from Ref. [83].

Porous materials are indispensable in applications such as molecular separation, energy storage, and catalysis.[84-86] However, the solid nature of most of the porous materials could sometimes, especially at large scales, limits their applications by imposing constraints in their processing and transport. The long-standing interest in developing liquids with permanent, nanoscale porosity to prevent the restrictions in processing and transport of existing porous solids has led to several breakthroughs in recent years.[87-91] For example, the synthesis of rigid organic cage molecules[87] marked "a new branch in the evolutionary tree of porous materials" beyond zeolites and MOFs.[92] The intensive research on developing porous liquids culminated in the successful synthesis of the first porous liquid in 2015.[83] Figure 1-4 shows the preparation of the porous liquids. Specifically, crown-ether functionalized diamines are coupled with 1,3,5-triformylbeznenes, resulting in hollow organic cage molecules. The porous liquid was then produced by dissolving the organic cage molecules (i.e., the porosity units) at high concentration into a 15-crown-5 solvent. Neither the crown-ether side groups nor the solvent molecules can enter the organic cage molecule due to steric restrictions, which makes it possible for such liquids

to contain permanent cavities. It was demonstrated that the permanent cavities in these liquids afford an eight-fold increase of the solubility of methane molecules compared to that of the neat solvents.

Exciting new avenues for gas capture, storage, and separation are opened up by the successful synthesis of the above porous liquids. Nevertheless, there is still significant room to improve the performance of existing porous liquids and it is desirable to develop new porous liquids with improved gas storage capacity and superior selectivity toward different molecules. To these ends, it is crucial to understand the molecular mechanisms of gas storage in porous liquids. Previous studies have provided valuable insights into some of these issues, e.g., the distribution of nanoscale cavities in the porous liquids has been clarified by MD simulations (Figure 1-5).[83] However, many important issues, in particular, the fundamental thermodynamics and kinetics of gas storage in the porous organic cage molecules, remain to be clarified. In addition to single gas storage inside individual cage molecules, it is also critical to understand how the presence of multiple gas species affects the adsorption of gas molecules inside individual cage molecules, i.e., how different gas molecules compete each other for adsorption inside a cage molecule, and how a cage molecule accommodates more than one molecule inside it. The former aspect is relevant to the application of porous liquids for gas adsorption and separation. The latter aspect is potentially relevant to applications in which the organic cage molecules in the porous liquids are used as a medium for confining small molecules to study their fundamental properties or as a nanoscale reactor.

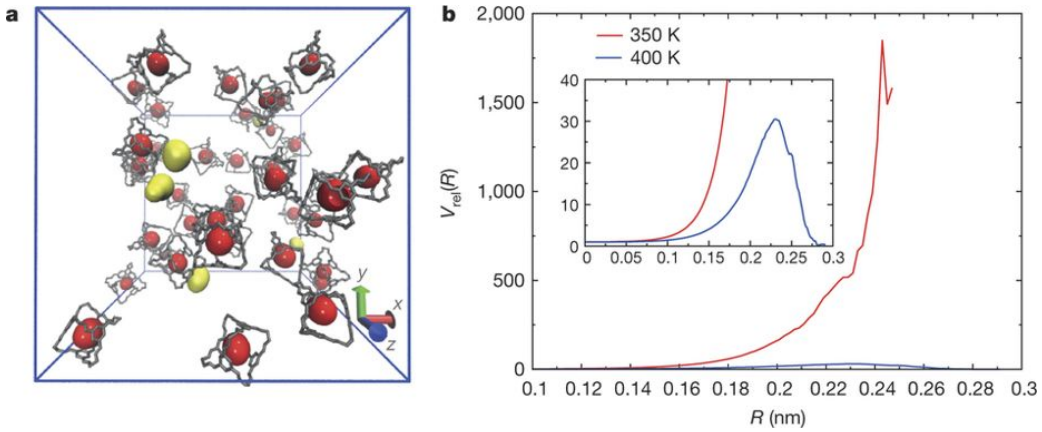

Figure 1-5. a. Some representative configurations of a porous liquid at 350 K. The red and yellow volumes indicate empty pores inside or outside the cages, respectively. **B**. Relative porosity, $V_{rel}(R)$, of the porous liquid at 350 K and 400 K. Inset, a zoom-in view of the data at 400 K. At 350 K, the porous liquid has around 1,900 times as many methane-sized cavities (probe radius ~0.24 nm) than does the pure solvent. The figure is reproduced from Ref. [83].

1.4.2 Water adsorption at mica-ionic liquid interfaces

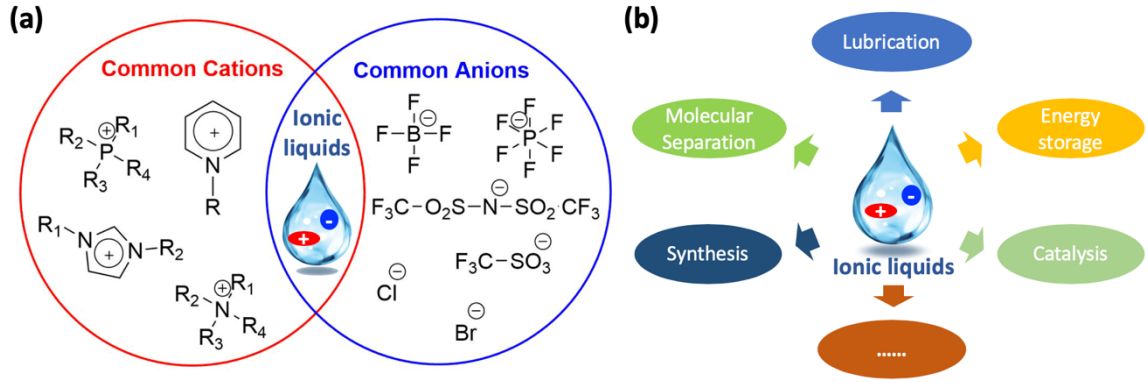

Figure 1-6. (**a**) The structure of some popular room-temperature ionic liquids (RTILs). (**b**) Some potential applications of room-temperature ionic liquids.

Pure room-temperature ionic liquids (RTILs) are a new class of materials consist of only ions but remain in the liquid state at temperature below 100°C (Figure 1-6a).[93-94] Because RTILs offer properties such as wide electrochemical window, low vapor pressure, excellent thermal stability, and flexibility in design, they have shown great promise in applications such as capacitive energy storage and lubrication (Figure 1-6b).[2-9] The performance of RTILs in many of these applications depends greatly on the interfacial

structures of RTILs adsorbed on solid surfaces.[93] Therefore, it is crucial to gain a fundamental understanding of these interfacial structures.

The interfacial structures of RTILs near solid surfaces have been investigated extensively using experimental,[3, 95-102] theoretical,[81, 103-106] and simulation methods.[9, 78-79, 107-117] Few of these studies, however, paid attention to the possible existence of water in RTILs and how the interfacial structures of RTILs can be affected by water. In reality, most RTILs are hygroscopic and can absorb noticeable amount of water from the environment.[118] Since 2014, these issues have received significant attention.[101-102, 105, 119-125] The impact of water on the interfacial structure of RTILs reported in these studies has been observed in recent studies,[123-124, 126] and it has been further shown that water also greatly modifies other macroscopic observables such as the capacitance of the EDLs near electrodes.[105] While the importance of water on interfacial structure of RTILs is generally recognized, difference in opinion does exist. For example, based on a study of mica-propylammonium nitrate (PAN) interfaces using amplitude modulated atomic force microscopy, McDonald *et al*. suggested that the adsorption of water at mica-RTIL interfaces is not essential for the electrification of mica surfaces in contact with some RTILs.[127]

The above experimental and simulation studies triggered many simulation studies of the solid-RTIL interfaces in presence of water. Among all solids, mica offers an ideal model surface and muscovite mica surface is one of the most studied surfaces. Previous work suggested that water alter the RTIL structure at mica surfaces.[101-102, 128] However, directly visualizing the change of interfacial RTIL structure experimentally is difficult, and the available experimental insight on such structure change is mostly inferred indirectly

from other macroscopic observables such as the force vs. distance curves. Such a limitation can be addressed using MD simulations. At present, such simulations are rather limited [121, 125] and focused mostly on the distribution of ion and water molecules normal to the mica surface. Limited attention has been paid to the 3D structure of *RTILs and water* near open mica surfaces. Understanding the 3D structure of RTILs and how it is affected by the water is important because recent experimental and simulation studies revealed that RTILs can exhibit rich 3D structures near solid surfaces.[3, 93, 129-133]

1.4.3 N_2 adsorption near atomically sharp electrodes

A recent report of electrochemical synthesis of NH_3 from N_2[134] by Song *et al.* showed that the N_2 gas dissolved in aqueous electrolytes can be electrochemically reduced on the surface of N-doped carbon electrode materials that exist in the form of carbon nanospikes with tip sizes as small as ~1 nm (as shown in Figure 1-7). It was shown that NH_3 can be synthesized electrochemically with a Faradaic efficiency of 11.5% and a production rate of 97.2 $\mu g\, hr^{-1}\, cm^{-2}$ under ambient conditions.[134] It was found that the reaction occurs only on the sharp tips of the carbon nanospikes, e.g., etching the sharp carbon nanospikes away results in a dramatic decrease in N_2 electrochemical reduction process. MD simulations in combination with *ab initio* calculations showed that electrical fields near the nanospikes are strongly enhanced and may be responsible for the observed reactivity of the otherwise inert N_2 molecules.[134] Regardless of the chemical details of the electrochemical reduction of N_2 near the carbon nanospikes, the adsorption of N_2 at the interface of carbon nanospikes and electrolyte solutions is an essential step of the electrochemical reactions. Understanding this phenomenon would thus help us better understand the electrochemical N_2 reduction on the carbon nanospikes.

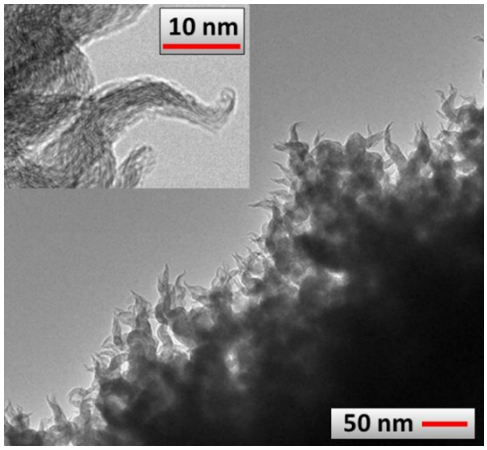

Figure 1-7. Representative TEM images of the carbon nanospikes electrode. The inset shows an HR-TEM image of an individual spike. This figure is reproduced from Ref. [134].

Prior works on the gas adsorption at solid-liquid interfaces can lend some help toward understanding of the adsorption of N_2 on/near carbon nanospikes. For instance, based on the prior simulations of dissolved N_2 and other similar gas molecules,[135-136] it is expected that N_2 molecules are locally enriched near carbon nanospikes compared to their distribution in bulk electrolytes. However, the adsorption of N_2 on carbon nanospikes in the experiments by Song *et al*. exhibits several features not explored in previous studies of gas adsorption at solid-liquid interfaces, and therefore some important questions remain open. First, during the electrochemical reduction of N_2, the carbon nanospikes are electrified and thus EDLs are established at the electrode-electrolyte interfaces. Within the EDLs, the structure of the solvent (water in the study by Song *et al*.), which can affect the gas adsorption based on prior research,[137] can deviate strongly from that near neutral solid surfaces and in bulk electrolytes. However, to our best knowledge, the adsorption of gas molecules near electrified electrodes, or equivalently in EDLs at the electrode-electrolyte interfaces, has not been studied. Second, the carbon nanospikes have tip sizes as small as ~1 nm. How gas adsorption is affected by the large curvature of these surfaces is not clear because most prior studies focused on gas adsorption near planar walls. The advent of

electrochemical catalysts with nanotextures has thus opened new opportunities for applications along with challenges for understandings.

1.5 Outline of the dissertation work

In this dissertation, the molecular adsorption in three novel material systems was explored using MD simulations. These works share the commonalities that they all feature small molecule adsorption in presence of a molecular liquid. The central line of the dissertation is to understand the molecular mechanisms underlying the adsorption behavior in these systems, with a focus on the issues raised in Sections 1.3. The goal of the work is that, by understanding the adsorption at the atomistic scale, to provide theoretical guidance on how to tailor these materials through rational material design to optimize their performance in target applications. The rest of the dissertation is organized as follows.

In Chapter 2, the thermodynamics and kinetics for the storage of three prototypical small molecules, CH_4, CO_2, and N_2, in porous liquids consisting of crown-ether substituted cage molecules in a 15-crown-5 solvent was studied. Different gas molecules were found to store inside the cage differently. All gas molecules considered can enter the cage essentially without energy barriers and leave the cage on nanosecond time scale by overcoming a modest energy penalty. The molecular mechanisms of these observations are clarified.

In Chapter 3, we extended our work in Chapter 2 and examined the multi-component gas storage in the same porous liquids. Storage of CO_2, CH_4, and N_2 molecules, and their binary mixtures in individual cage molecules was computed. A molecular picture of how gas molecules are stored in the cage molecule and how the storage of one type of gas

molecule is affected by other types of gas molecules was provided. The results clarify the molecular mechanisms behind the selectivity of such cage molecules toward different gases.

In Chapter 4, how water affects the three-dimensional structure of an RTIL [BMIM][Tf_2N] near mica surfaces with two different charge densities was investigated. The results indicate that water not only can alter the layering of ions near the mica surface, but also their lateral and orientation ordering and the aggregation of cations' hydrophobic tails. The structure of ionic liquids near solid surfaces was suggested to be governed by the three-way coupling between the self-organization of ions, the adsorption of interfacial water, and the electrification of the solid surfaces.

In Chapter 5, the adsorption of dissolved N_2 in the electrical double layers (EDLs) of an aqueous electrolyte near planar and 1-nm-radius spherical carbon electrodes was studied. The adsorption behavior of N_2 molecules, especially their dependence on the surface charge and curvature of electrodes, was rationalized by examining the structure of interfacial water molecules, their interference with the hydration shell of N_2, and their modification by the electrification of electrodes

In Chapter 6, the major contributions of this dissertation are summarized.

Chapter 2: Thermodynamics and Kinetics of Gas Storage in Porous Liquids

Disclosure

This work has been published by the American Chemical Society: F. Zhang, F. Yang, J. Huang, B. G. Sumpter, and R. Qiao, "Thermodynamics and kinetics of gas storage in porous liquids", The Journal of Physical Chemistry B, 120, 29, 2016.

2.1 Introduction

Porous materials are indispensable in numerous applications such as molecular separation, energy storage, and catalysis.[84-86] However, most porous materials with permanent porosity, e.g., zeolites[138] and metal-organic frameworks (MOFs),[13] exist as solids. The solid nature of these materials poses certain degrees of restrictions on their processing, transport, and integration into engineering systems, especially at large scales. In comparison, porous liquids can potentially circumvent many of these restrictions because they are relatively easy to transport and process. There has been a long-standing interest in developing liquids with permanent, nanoscale porosity, and related research has led to many breakthroughs in recent years.[87-91] For example, the synthesis of rigid organic cage molecules[87] was considered to have initiated "a new branch in the evolutionary tree of porous materials" that is beyond zeolites and MOFs.[92] The intensive research on developing porous liquids culminated in the synthesis of the first liquids with permanent porosity in 2015.[83] Specifically, crown-ether functionalized diamines are coupled with 1,3,5-triformylbeznenes, giving hollow organic cage molecules. The resulting molecules

(i.e., the porosity units) were dissolved at high concentration into a 15-crown-5 solvent to produce porous liquids. Such liquids contain permanent cavities because neither the crown-ether side groups nor the solvent molecules can enter the organic cage molecule due to steric restrictions. It was demonstrated that the permanent cavities in these liquids afford an eight-fold increase of the solubility of methane molecules compared to that of the neat solvents.

The successful synthesis of permanently porous liquids opens up exciting new avenues for gas capture, storage, and separation. Nevertheless, there remains significant room to improve the performance of porous liquids, e.g., it is desirable to develop new porous liquids with improved gas storage capacity and superior selectivity toward different gas molecules. To help rationally design these materials, it is crucial to understand the molecular mechanisms of gas storage in porous liquids. Previous studies have provided valuable insights into some of these issues, e.g., using molecular dynamics (MD) simulations, the distribution of nanoscale cavities in the porous liquids has been clarified.[83] However, many important issues, in particular, the fundamental thermodynamics and kinetics of gas storage in the porous organic cage molecules, remain to be clarified. In this work, we studied the storage of different gas molecules including CH_4, CO_2, and N_2 in porous liquids made of crown-ether substituted cage molecules dissolved in a 15-crown-5 solvent. Using MD simulations, we investigated the capacity and kinetics of the gas storage in the molecular cages. To elucidate the physics behind these macroscale characteristics, we also examined how gas molecules are stored inside the cage, the free energy landscape for gas molecules entering and leaving the cage, and the dynamic exchange between gas molecules inside and outside the cage.

2.2 Simulation System and Methods

Figure 2-1a shows the molecular structure of the crown-ether substituted cage and Fig. 2-1b highlights the functional motif of the cage for gas storage. Briefly, the cage has approximately an octahedral structure (marked with black lines in Fig. 2-1b), which consists of a non-spherical cavity and four access windows (one of them is marked by a shaded triangle in Fig. 2-1b) that allow gas molecules to enter/leave the cage. To facilitate discussions later, we define the entrance vectors of a cage as the vectors pointing from the center of the cage to the center of each of the four access windows (see Fig. 2-1b). Figure 2-1c shows the molecular structure of the solvent and the gas molecules studied. Figure 2-1d shows the partial atomic charges on the cage molecule as given by the force fields adopted here.

To study gas storage in the cage, we adopt a setup similar to the simulation system used by Giri et al.[83] Specifically, 20 cage molecules and 400 15-crown-5 solvents were mixed inside a periodical simulation box at a solvent-cage ratio of 20:1. Sixty gas molecules were dispersed into the cage-solvent mixture at a gas-cage ratio of 3:1, which creates an excess of gas molecules in the solvents. Compared to systems in which the porous liquids are in equilibrium with a gas reservoir, the present setup allows us to focus on studying the intrinsic gas storage capacity of molecular cages. The molecular structure of the solvent and three types of gases studied are shown in Fig. 2-1c. The CH_4 molecule is roughly spherical with a diameter of ~0.40 nm. The CO_2 molecule is rod-like, with a length and diameter of 0.53 nm and 0.34 nm, respectively. The N_2 molecule, also rod-like, is the smallest gas molecule considered here, with a length and diameter of 0.4 nm and 0.28 nm, respectively.

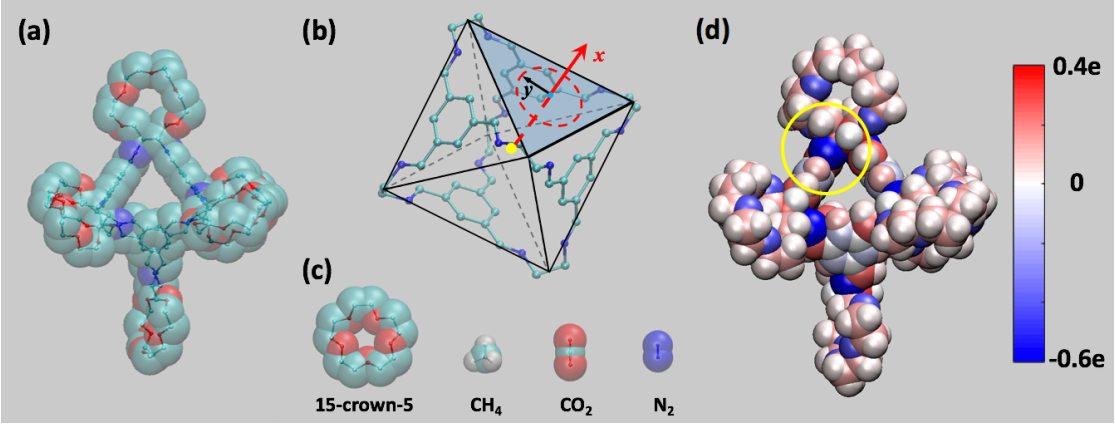

Figure 2-1. (a) The molecular structure of the cage molecule. (b) A schematic of the functional part of the cage molecule for gas storage. The yellow dot denotes the center of the cage cavity. The red arrow denotes the entrance vector of the cage molecule. (c) Molecular structure of the solvent molecule and the gas molecules. For clarity, hydrogen atoms of the cage molecule and the solvent molecule are not shown. (d) Partial atomic charge on the cage molecule (a list of the partial charge can be found in Reference [83]). The yellow circle highlights an imine atom with the largest partial charge, which is located near the vertex of the cage molecule.

The OPLS-AA force fields[139] were used to describe the cage, solvent, and CH_4 molecules. CO_2 and N_2 molecules were modeled using the EPM2 and TraPPE force fields, respectively.[140-141] Of these force fields, those for CH_4, CO_2, and N_2 molecules are well established in prior studies of gas adsorption in MOFs.[142] The force fields for the cage molecules and the 15-crown-5 solvent are the same as those used in Ref. [83]. To validate the force fields for the solvent, we simulated a pure 15-crown-5 solvent at 293.15 K and 1 atm. The solvent density was found to be 1.108 g/cm^3, in good agreement with the experimental value of 1.113 g/cm^3. In addition, simulations with the force fields used here for cage molecules reproduced the solubility of CH_4 gas in porous liquids.[83] Hence the force fields adopted in this study are adequate for the simulation of gas storage in porous liquids. We note that the flexibility of the cage molecules was taken into account in the force fields adopted here. However, simulations indicated that the cage molecule is rather rigid. Its

shape fluctuation is minor when dispersed in the solvents (see Figure A-1 in Appendix A) and thus does not play a significant role in the gas storage.

MD simulations were performed in the isobaric-isothermal ensemble (T=400K and P=1atm) using the Gromacs code.[143] The PME method was used to calculate the electrostatic interactions with a real space cutoff of 1.4 nm and an FFT spacing of 0.12 nm. Non-electrostatic interactions were computed with a cutoff length of 1.4 nm. Only the C-H bonds were constrained using the LINCS algorithm.[144] Simulations were performed using a time step of 1 fs, and neighbor list was updated every step. To build the MD system, the cage and solvent molecules were first packed into the simulation box using the Packmol code.[145] The system was equilibrated for 5 ns before gas molecules were randomly inserted into the simulation box. An equilibrium run of 5 ns was then performed. To ensure that the system was sufficiently equilibrated, we examined the mean-square-displacement of the solvent and cage molecules, which diffuse much slower than the gas molecules and are thus more difficult to equilibrate. The results (see Figure A-2 in Appendix A) showed that, over a time period of 2 ns, a solvent molecule already diffuses ~1 nm on average, which is larger than its size. Hence the solvent molecules are well equilibrated in the system. Over the same time period, a cage molecule diffused only several angstroms. However, since cage-cage separation is large in our system (thus the gas storage depends mostly on the solvent and gas structure near the cage molecules), the limited center-of-mass movement of a cage molecule does not affect the evaluation of its gas storage capacity as long as solvents and gas in the system are sufficiently equilibrated. The equilibration run was followed by a 20 ns production run. For each gas studied, the simulation was repeated five times with different initial configurations to obtain reliable statistics.

2.3 Results and Discussion

2.3.1 Capacity and mode of gas storage.

Figure 2-2 shows the accumulative count of gas molecules as a function of the distance from the center of the cage. Although the octahedral cage spans a maximum of ~0.8 nm radially, the accumulative gas count increases very slowly at radial distances larger than ~0.5 nm, indicating that few gas molecules are stored in this space. Examination of the structure of the cage (see Fig. 2-1b) shows that this space is either occupied by the cage atoms or outside of the cage cavity. Hence, gas molecules located within a distance of 0.5 nm from the cage center are defined as being stored inside the cage. Using this definition and the data shown in Fig. 2-2, the storage capacity of the cage was determined to be 1.47, 1.30 and 1.14 molecules for CH_4, CO_2 and N_2, respectively. These capacities are specific to the system studied here because they are affected by the overall density of the gas molecules in the *closed* MD system. Nevertheless, they provide an indication of the *relative* storage capability of the cage molecule for different gases and analysis of the gas distribution and energetics inside the cage molecule can provide insights into gas storage under practical conditions. Interestingly, the storage capacity does not correlate simply with the gas molecule's size: despite CH_4 being larger than N_2 molecule, the cage hosts more CH_4 molecules than N_2 molecules. To understand the mechanism behind this peculiar observation and more generally the net storage capacity of the molecular cages, we further studied the molecular details of gas storage inside the cage.

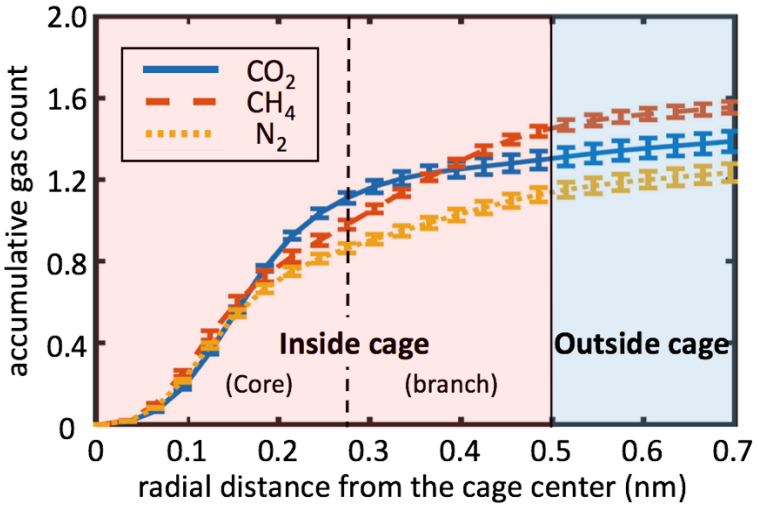

Figure 2-2. Accumulative gas molecule count as a function of the radial distance from the center of the cage. The position of a gas molecule is based on its center-of-mass.

Since the cavity inside a cage molecule is not spherical, how gas molecules are distributed inside a cage can greatly affect their storage. Hence, we examine the three-dimensional (3D) distribution of gas molecules inside the cage to delineate how they are stored. Figure 2-3 shows the isosurfaces of the number density of CH_4 and CO_2 molecules inside the cage (the distributions of the N_2 molecules exhibit a behavior intermediate to that of the CH_4 and CO_2 molecules and are thus not shown). To illustrate which region within the cage the gas molecules can *access*, the isosurface is set to a number density of 2.8 nm^{-3} in Fig. 2-3a, which is about 20 times of the gas density in bulk solvents, but nevertheless small compared to the high gas density in some parts of the cage. Compared to the CH_4 molecules, CO_2 molecules access more (less) space in the central (peripheral) portion of the cage. To illustrate which region within the cage a given gas *prefers*, the isosurface is set to a number density of 35.0 nm^{-3} in Fig. 2-3b. Figure 2-3b shows that CO_2 molecules favor the central part of the cage, whereas CH_4 molecules have similar preference to the central and peripheral parts of the cage. These observations suggest partition the space inside the cage into two types of regions: (1) a "core" region at the center

of the cage and (2) four rod-like "branch" regions close to the cage's four access windows (cf. Fig. 2-1b). Based on the results in Fig. 2-3, the boundary between these two types of regions can roughly be set at a distance of 0.28 nm from the cage's center (marked by the black dashed lines in Figs. 2-2 and 2-3). With this partition, the storage capacity of a single cage for CH_4, CO_2 and N_2 molecules was found to be 1.0, 1.12 and 0.87 in its core region and 0.47, 0.18 and 0.27 in its branch regions.

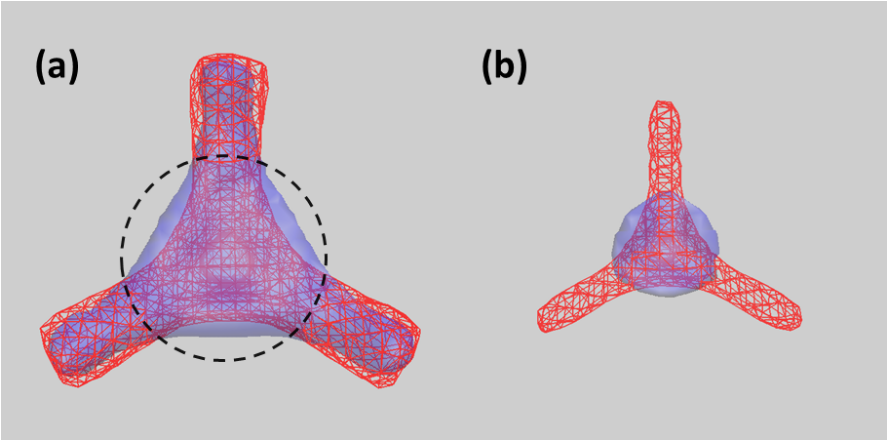

Figure 2-3. Isosurfaces of CO_2 (blue) and CH_4 (red) gas density inside the organic cage molecule. (a) Isosurfaces for gas density of 2.8 nm^{-3}. (b) Isosurfaces for gas density of 35 nm^{-3}. The black dashed line (radius: 0.28 nm) marks the boundary between the cage's core region and branch regions.

The different storage capacity of the various gas molecules inside the cage's core region depends on the different gas-cage interactions. Specifically, the potential of a CO_2 molecule in the cage's core region due to its non-electrostatic interactions (its attractive component represents the van der Waals interactions) with the cage was found to be -21.8 kJ/mol, which is stronger than that of a CH_4 molecule (-17.02 kJ/mol) and N_2 molecule (-12.95 kJ/mol). Therefore, gas molecules are energetically favored in the cage's core region in the order of $CO_2 > CH_4 > N_2$. Since both CO_2 and N_2 molecules have notable quadrupole moments and charge-quadrupolar interactions play an important role in gas storage in porous materials such as zeolites,[146] we examine the distribution of the partial charges on

the cage atoms and the electrostatic gas-cage interaction energy for the gas molecules in the cage's core region. We found that, while some atoms of the cage molecule carry notable charge (up to -0.6e, see the Fig. 2-1d), the electrostatic gas-cage interactions are rather weak (-2.7 kJ/mol for the CO_2 molecules and -0.3 kJ/mol for the N_2 molecules) and thus play a very limited role in controlling gas storage in the cage. The weak electrostatic interactions are caused by two effects. First, gas molecules cannot approach closely the cage atoms carrying notable partial charges (mostly located near the vertices of the cage molecule, as highlighted by the yellow circle in Fig. 2-1d) due to the obstruction by other atoms. Second, the electrostatic interactions between quadrupolar gas molecules CO_2 (or N_2) and charged cage atoms decay rapidly with charge-gas separation r (i.e., $\sim 1/r^3$).[146]

The storage capacity of different gas in the cage's branch region is affected by both the steric and the van der Waals interactions. For the CO_2 molecules, which are considerably longer than the N_2 molecules, because of their steric interactions with the cage atoms in the branch region, they mostly align with the cage's entrance vector upon entering the narrow branch regions (see Fig. 2-4). This restricts the CO_2 molecule's rotation and thus incurs an entropic penalty. Consequently, few CO_2 molecules are stored in the branch regions. For the nearly spherical CH_4 molecule, such an entropic penalty is minor. For the N_2 molecules, which are nearly randomly oriented with respect to the cage's entrance vector (see Fig. 2-4), such an entropic penalty is likewise minor. However, the CH_4 molecules interact with the cage atoms in the branch region through van der Waals forces more strongly than the N_2 molecules. This, along with the fact that the electrostatic interactions between the cage and gas molecules (N_2, CH_4, and CO_2) in the branch region

are very weak, makes the storage capacity of CH_4 molecules higher than that of the N_2 molecules in the branch regions.

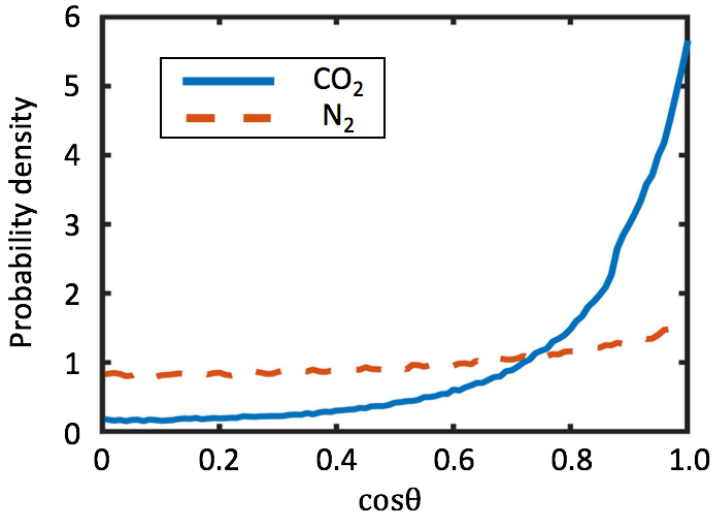

Figure 2-4. The distribution of the angle θ formed between a gas molecule's axis (O-C-O for CO_2 and N-N for N_2) and the cage molecule's entrance vector when the gas molecule resides in the branch region of the cage molecule.

Because gas molecules can distribute in different parts of a cage, it is possible that several gas molecules occupy the cage simultaneously. Figure 2-5 shows the probability distribution of the cage being occupied by different number of gas molecules. Overall, the probability of finding multiple molecules within a single cage is the highest for the CH_4 molecules. This can be attributed to the facts that (1) CH_4 molecules favor both the cage's core and branch regions (2) CH_4 molecules are small enough that a cage can accommodate one CH_4 molecule in its core and a few more CH_4 molecules in its branch regions. For the CO_2 molecules, since they rarely reside in the cage's branch regions due to the large entropic penalty, storing two CO_2 molecules simultaneously inside the cage requires both molecules to be packed into the cage's core region, which is rather difficult. Consequently, finding multiple CO_2 molecules simultaneously inside one cage is more difficult than the case of CH_4 molecules. Although N_2 molecules are small enough for a cage to

accommodate one N_2 molecule in its core and several other N_2 molecules in its branches, multiple occupancy is rare because they are attracted to the cage rather weakly. Also due to the weak interaction, N_2 has the highest probability of leaving a cage molecule.

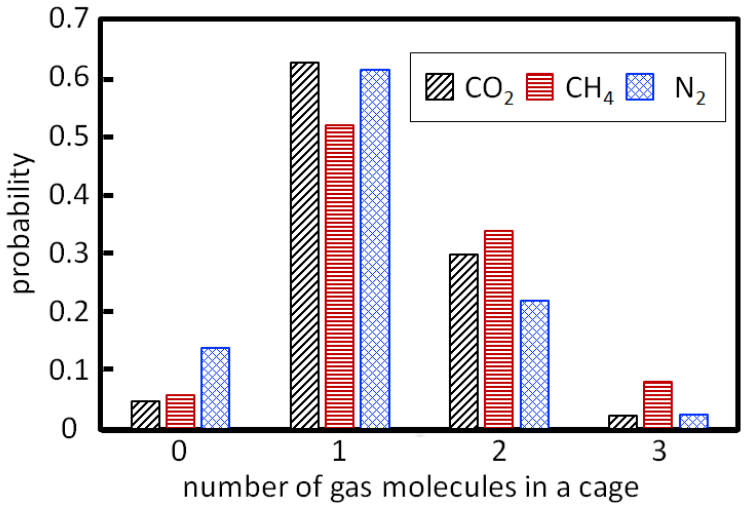

Figure 2-5. The probability distribution of the number of gas molecules inside a cage. The probability that four gas molecules occupy the same cage is <0.1% in the present system and is thus not shown.

Based on these results, we suggest that the storage of simple gas molecules in a given cage is controlled mainly by two factors: molecular gas-cage interactions that determine how strongly gas molecules are favored energetically inside the cage and the size/shape of the gas molecules which determine to what extent different storage spaces inside a given cage (i.e., the core and the branch regions) can be used *simultaneously*. The storage capacity is the highest for the CH_4 molecules because both factors are favorable for them. The storage capacity is lower for the CO_2 molecules because they cannot effectively make use of the cage's storage space in the narrow branch regions due to large entropic penalty. The storage capacity is the lowest for the N_2 molecules because their molecular interactions with the cage are weak, hence providing limited energetic benefit for N_2 molecules to be stored inside the cage.

2.3.2 Kinetics of gas storage.

For practical application of porous liquids, one must understand not only the capacity of gas storage, but also the kinetics of gas storage, i.e., how easy/difficult gas molecules enter/leave the cage. To answer this question, we calculated the potential of mean force (PMF) of gas molecules near and inside a cage molecule. Specifically, the PMF of gas molecules in and near the cage was computed using $\mathrm{PMF}(x,y) = k_B T \times \ln\left(\rho_n^{\infty}/\rho_n(x,y)\right)$ where (x,y) is the position of the gas molecule with respect to the cage's entrance vector (see Fig. 2-1b for definition), $k_B T$ is the thermal energy, ρ_n^{∞} is the number density of gas molecules in bulk solvents and $\rho_n(x,y)$ is the gas density at a position (x,y). Note here the PMF in the bulk solvents is taken as zero. In the present system, the free energy landscape is relatively smooth (this is evident from the facile exchange between gas inside and outside the cage, see below). Hence, very good statistics of gas density and PMF can be obtained from long simulations without the need of steering.

Figure 2-6a shows the PMF of different gas molecules along the cage's entrance vector. When the gas molecule is outside of the cage (i.e., located at distance larger than 0.5 nm from the cage center), the PMFs of the three gases show very little difference. A distinct peak of the PMF exists at a distance of 0.85 nm from the cage center, indicating that an energy barrier exists for the gas molecule entering the cage along its entrance vector. This energy barrier originates from the dense packing of solvent molecules outside the cage's access window, which hinders gas from entering into the cage (see Fig. A-3 in the Appendix A). Inside the cage, the PMFs show a kink/shoulder in the cage's branch regions. For the long CO_2 molecules, this kink originates largely from the entropic penalty of

confining it in the narrow rod-like branch regions. For the shorter N_2 and CH_4 molecules, the shoulder is likely caused by the reduced van der Waals attractions with the cage atoms.

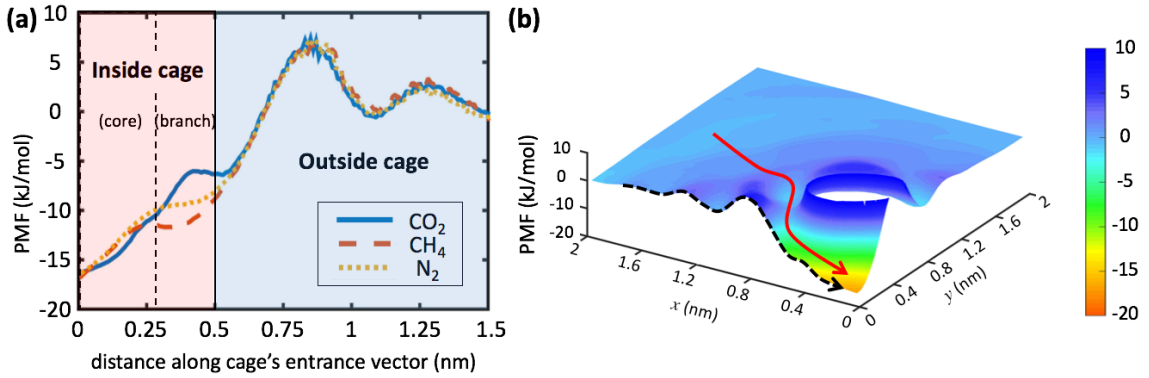

Figure 2-6. The PMF of gas molecules inside and near a cage molecule. (a) The one-dimensional PMF along the cage's entrance vector defined in Fig. 2-1b. (b) The two-dimensional PMF for the CO_2 molecule as a function of the distance along and normal to the cage's entrance vector (*x*- is along the entrance vector and *y*- is normal to the entrance vector, see Fig. 2-1b). The red line denotes a likely pathway for a CO_2 molecule to enter the cage. The black dashed line denotes the PMF along the cage's entrance vector, which was also shown in panel (a) (blue line). The PMF in (a) has an error bar of ~0.2-1.2 kJ/mol, with the largest error occurring at a distance of ~0.8 nm from the cage center.

The PMF shown in Fig. 2-6a indicates that gas molecules entering in the cage along the cage's entrance vector must overcome an energy barrier of ~7 kJ/mol. However, there may exist other pathways with weaker or no energy barrier. To delineate these other possible pathways, we calculated the two-dimensional (2D) PMFs for gas molecules as a function of their distance along and normal to the cage's entrance vector (shown as the *x*- and *y*-directions in Fig. 2-1b). It is found that these PMFs are qualitatively similar for all three gases. Hence only the 2D PMF for the CO_2 molecule is shown in Fig. 2-6b. It can be seen that there indeed exists an energy barrier-free pathway (marked using a red line) for CO_2 gas molecules to enter the cage. Overall, the PMFs shown in Fig. 2-6 indicates that, for all gases studied here, gas molecules can enter the cage essentially without an energy barrier. However, for gas molecules to leave the cage, they must overcome an energy

penalty. This energy penalty depends on the position of the gas molecules inside the cage and can be up to ~16 kJ/mol for each of the gas considered here.

The modest energy penalty for gas molecules to leave a cage suggests that the cage molecule can indeed trap gas molecules. For applications in gas storage, one often needs to know the time scale that a gas molecule can be trapped inside in a cage. To find this time scale, we computed the occupancy autocorrelation function of gas molecules $C_p(t) = \langle p(0)p(t)\rangle$, where the bracket $\langle\cdots\rangle$ denotes the ensemble average, $p(t)$ is defined as 1.0 if the gas molecule inside a cage at t=0 continuously resides in the cage until time t. Figure 2-7 shows that, for all gases, $C(t)$ decays to ~0.1 within ~1 ns. Hence the mean residence time of a gas molecule inside a cage is on the order of nanoseconds, which suggests that the exchange of the gas molecules inside and outside of the cage is rather rapid.

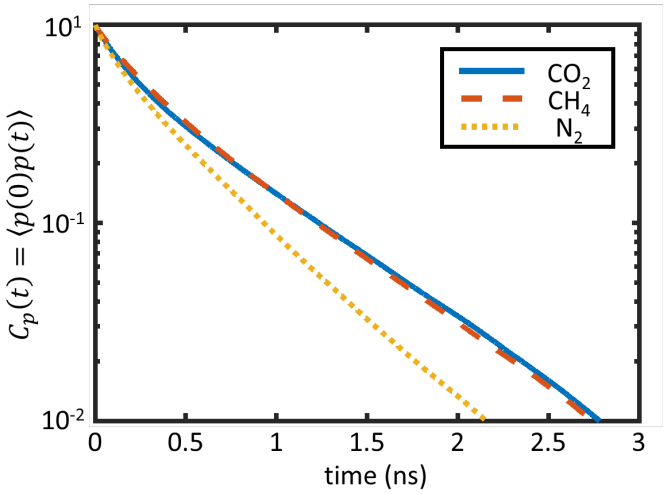

Figure 2-7. The cage occupancy autocorrelation function for three different gases.

2.4 Conclusions

In summary, we have studied the storage of three different gas molecules in a class of porous liquids (crown-ether substituted cage molecules in a 15-crown-5 solvent) using MD

simulations. We have found that the capacity of gas storage in a cage molecule is governed by the non-electrostatic (dispersive) intermolecular interactions between the gas and the cage and the size/shape of the gas molecules. The former controls the affinity of gas molecules to the cage; the latter mainly controls whether the space inside the cage can be utilized effectively (e.g., whether one can store, simultaneously, one gas molecule in the cage's core and a few others in the cage's branch regions). Due to the competition between these two factors, the cage's gas storage capacity does not correlate simply with the gas molecule's size. All gas molecules studied here can enter the cage without noticeable energy barrier. However, gas molecules inside a cage must overcome a modest energy penalty before leaving the cage. Despite this, gas molecules inside the cage can exchange rather rapidly with those in the bulk solvent. The insight gained here on the gas storage in organic cages, along with the knowledge on solubility of gas in the solvents, may help formulate rational design rules for porous liquids for specific applications. For example, for applications targeting N_2/CO_2 separation, our results suggest that increasing the size of the cage molecule's core is desirable. Since the storage of CO_2 molecules inside a cage is limited mainly by the difficulty in packing multiple CO_2 molecules into the cage's core but the storage of N_2 is limited mainly by the weak N_2-cage interactions, this modification of the cage should enhance the storage capacity for CO_2 molecules more greatly than that for the N_2 molecules.

Supporting Information Available in Appendix A: The structural fluctuations of the cage molecules in the porous liquids, the diffusion of solvent molecules in the porous liquids, and the density distribution of solvent molecules along the cage's entrance vector.

Chapter 3: Multi-Component Gas Storage in Organic Cage Molecules

Disclosure

This work has been published by the American Chemical Society: F. Zhang, Y. He, J. Huang, B. G. Sumpter, and R. Qiao, "Multicomponent Gas Storage in Organic Cage Molecules", The Journal of Physical Chemistry C, 121, 22, 2017.

3.1 Introduction

New types of porous materials, ranging from zeolites to metal-organic frameworks (MOFs),[13, 138] have been continuously proposed and synthesized over the past few decades. Owing to their high porosity and large surface area, these materials have found applications in a broad range of fields such as molecular separation, energy storage, and heterogeneous catalysis.[2, 84-85] However, these porous materials including zeolites and MOFs mainly exist as solids, making it more difficult to implement them in a typical flow process than liquids. Due to the challenges toward practical applications posed by the solid nature of these materials, especially at large scales, developing liquid state porous materials has been actively pursued in the past.[83, 87, 90-91, 147-151] In this regard, the synthesis of organic cage-like molecules in 2009[87] is a critical step towards developing such materials[152-154] since it has been considered by some experts in the community as introducing "a new branch in the evolutionary tree of porous materials" beyond zeolites and MOFs.[92] Such cage molecules provide a porous unit that can be dissolved into liquids without breaking any chemical bonds. Since then, rapid progress has been made toward making porous liquids

using organic cage molecules.[88-91, 150] While the initial attempts made by attaching long hydrocarbon chains to the organic cage-like molecules led to a lower melting point, the porosity was easily destroyed in liquid state due to the penetration of hydrocarbon chains into the cage cavities.[91] Most recently, with ingenuity in chemical design and aid of computational tools, Giri and colleagues successfully prepared and characterized the first organic molecular porous liquids.[83] Specifically, they coupled crown ether functionalized diamines with 1,3,5-triformylbeznenes and dissolved the resultant cage molecules at high concentration into a 15-crown-5 solvent. They also reported a porous liquid system with scrambled cage molecule dissolved in hexachloropropene solvents.[83] These porous liquids thus prepared are potentially effective gas absorbents, which can be transported and implemented relatively easily in industrial systems.

The currently available porous liquids have already shown promise in some areas including gas storage and separation.[92] Nevertheless, as with many other revolutionary and novel materials, the best applications of porous liquids may not have been identified, and the development of porous liquids for intended applications is still at an early stage. Despite this, it is safe to expect that the adsorption of small molecules inside the organic cage molecules will play a critical role in most, if not all, applications of porous liquids. Therefore, there is a great need to develop a fundamental understanding for the adsorption of gas molecules in the organic cage molecules dispersed in liquid solvents.[155] Molecular dynamics (MD) simulations can be a powerful tool for this purpose, e.g., MD has been used to show that solvent molecules in the porous liquids synthesized recently must pay a very high free energy cost to enter the organic cage and thus the intrinsic cavity of the organic cage molecules is maintained in the porous liquids.[83, 156] We previously studied the

thermodynamics as well as kinetics for the storage of pure CO_2, CH_4, and N_2 molecules in crown-ether-substituted cage molecules dissolved in a 15-crown-5 solvent using MD simulations.[157] We showed that the storage capacity of gas in a cage molecule is governed by the nonelectrostatic (dispersive) intermolecular interactions between the gas and the cage and by the size/shape of the gas molecules. The gas molecules considered can enter the cage molecule without a notable barrier and exit the cage on a nanosecond time scale.

In this work, we study the adsorption of prototypical small gas molecules including CO_2, CH_4 and N_2 in porous liquids that are in equilibrium with gas-phase reservoirs containing either pure gas or binary mixtures of different gases. We seek to understand how the presence of multiple gas species affects the adsorption of gas molecules inside individual cage molecules, in particular, how different gas molecules compete each other for adsorption inside a cage molecule, and how a cage molecule accommodates more than one molecule inside it. The former aspect is relevant to the application of porous liquids for gas adsorption and separation. The latter aspect is potentially relevant to applications in which the organic cage molecules in the porous liquids are used as a medium for confining small molecules to study their fundamental properties or as a nanoscale reactor. The rest of the manuscript is organized as follows. Section 3.2 describes the simulation system and methods. Section 3.3 presents the results for storage of pure gas and binary mixture in individual cage molecules and the underlying molecular mechanisms. Finally, conclusions are drawn in Section 3.4.

3.2 Simulation System and Methods

We use MD simulations to study the storage of gas molecules in the organic cage molecules dissolved in molecular solvents. Figure 3-1 shows the molecular structures of the cage molecule, the 15-crown-5 solvent molecule, and the CO_2, CH_4, and N_2 gas molecules. The crown-ether-substituted cage molecule (porous unit) consists of an organic cage-like octahedron and 6 looped crown ether tails (see Fig. 3-1a). The cage-like octahedron provides a nonspherical cavity and four access windows allowing gas molecules to get in/out of the cage cavity. Because both the crown ether tails of the cage molecules and the solvent molecules (Fig. 3-1b) have a circular structure that limits their access to the cage's cavity, the liquid mixture of the cage molecules and the solvents together form a porous liquid. The gas molecules considered here (see Fig. 3-1c) are relatively small and thus can be stored inside the cage molecule. These gas molecules differ in both shape and size: the CH_4 molecule, although explicitly modeled by one C atom and four H atoms as a tetrahedron shape, has a rather spherical shape with an effective diameter of 0.42 nm,[158-159] while CO_2 and N_2 molecules are both rod-like. The long and short axes of the CO_2 molecule (0.52 nm and 0.34 nm, respectively) are slightly longer than those of the N_2 molecule (0.41 nm and 0.30 nm, respectively).[160] As shown below, the shape and size of gas molecules play an important role in determining their storage capacity inside the cage molecules and the selectivity of cage molecules toward different gas molecules.

Figure 3-1d shows a snapshot of the MD system used for the simulations. The system consists of a gas bath (the lower gas reservoir and upper gas reservoir are connected because of the periodic boundary condition) and a slab of porous liquids positioned in the middle of the fully periodical simulation box. The porous liquid is made by dissolving one

crown-ether-substituted cage molecule into 170 solvent molecules. Since gas molecules can exchange freely between the liquid phase and gas phase, this setup allows us to study the gas storage under well-controlled partial pressure in the gas phase.

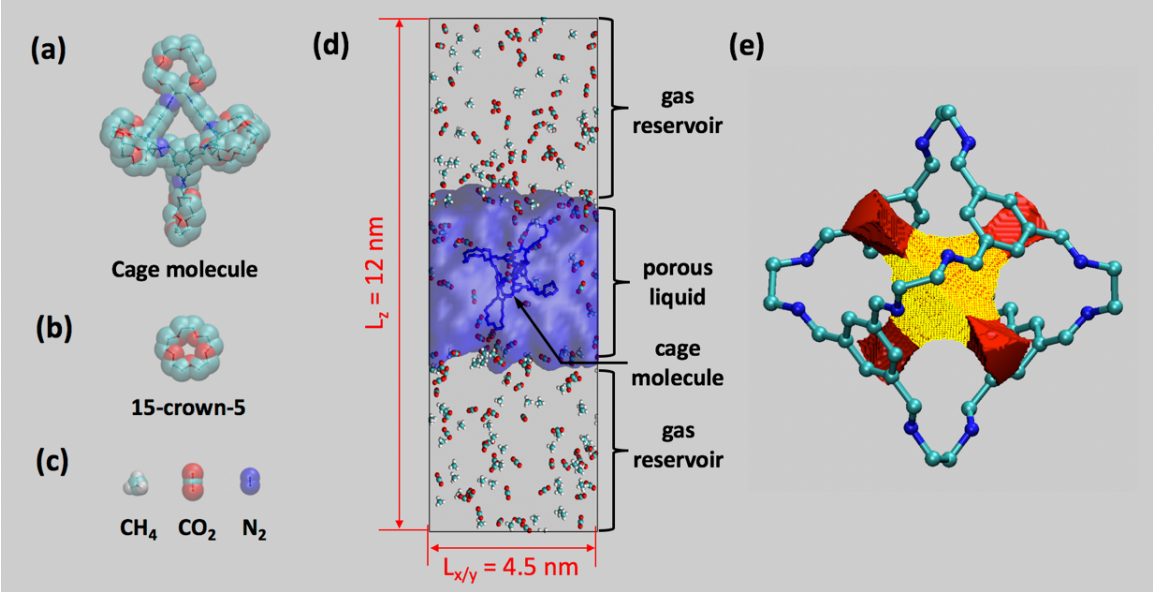

Figure 3-1. Molecular modeling of gas storage in porous liquids. (a-c) Molecular models of the crown-ether-substituted cage molecule (a), the solvent molecule (b), and the gas molecules (c). (d) A snapshot of the simulation system consisting of porous liquids (rendered as isosurface in blue) in equilibrium with a binary mixture of CO_2 and CH_4. (e) Volume rendering of the accessible space in a cage molecule superimposed on the molecular model of the cage. The accessible space is probed using an atom of 0.28 nm in diameter. The accessible space within a radial distance of 0.28 nm from the cage center is shown in yellow; the accessible space within a radial distance of 0.28 to 0.5 nm from the cage center is shown in red. For clarity, the hydrogen atoms of the cage molecule and the solvent molecule are not shown. In (e), crown ether tails are not shown.

Ideally, a systematic study of the gas storage calls for the computation of the gas adsorption isotherm in the cage molecule by systematically varying the partial pressure of different gas species in the gas bath. However, given the very large parameter space that must be explored in such studies, we focused on two sets of studies in this work. In the first set of study, five systems with identical porous liquid but different gas bath compositions (pure CO_2, pure CH_4, pure N_2, CO_2+CH_4 mixture, and CO_2+N_2 mixture) were set up. For

these systems, we examined the gas storage under a fixed partial gas pressure in the gas bath instead of computing the gas adsorption isotherm under many different partial pressures. Specifically, the partial pressure of each gas in the gas bath was controlled to be the same in all simulation systems ($P_b = 27.5 \pm 0.3$ bar, see Fig. B-1 in Appendix B). For example, the pressure of CO_2 in the gas bath for the pure CO_2 simulation is the same as the partial pressure of CO_2 in the gas bath for the CO_2+CH_4 simulation. With a relatively high partial gas pressure to help improve the gas storage statistics inside individual cage molecule, this first set of simulation allows us to gain useful insight on the gas storage by delineating how gas molecules are stored inside a cage and by comparing the results for different gas molecules. In the second set of study, we computed the adsorption isotherm of CO_2 and CH_4 molecules in the cage molecule in equilibrium with gas bath containing CO_2+CH_4 mixture. To this end, five systems with identical porous liquids but different gas baths were studied. The partial pressures of the CO_2 and CH_4 in the gas bath were equal and varied from 9 to 54 bar in different simulations. This set of simulation allows us to examine the effect of partial pressure on the gas storage inside the cage molecule.

The force fields for all molecules were the same as those adopted in our previous work.[157] Briefly, the cage molecule and the solvent molecule were modeled using the OPLS-AA force fields.[139] The CO_2, CH_4, and N_2 molecules were modeled using the EPM2, OPLS-AA, and TraPPE force fields, respectively.[139-141] The force fields for the cage molecule used here is a reasonable choice because they are compatible with the force fields for the solvent and gas molecules. It has been established that the force fields we adopted for the gas molecules can reproduce their thermodynamic properties such as compressibility and phase diagram quite well, and meanwhile are widely used in studying

their adsorption behavior in other porous materials such as MOFs.[161] As shown in the first molecular modeling of porous liquids[83] as well as our previous work,[157] these force fields allow the key properties of the solvents, e.g., their density and solubility, to be predicted quite well. In addition, rapid exchange of gas inside and outside the cage molecule was observed in all simulations, which indicates that the gas molecules studied here can enter without notable energy barrier and leave the cage cavity easily, consistent with recent experimental results.[156]

The MD simulations were performed in the NVT ensemble (T=400 K) using the Gromacs code.[143] Here we adopt a rather high temperature to facilitate both the diffusion of gas molecules in the solvent and the exchange of gas molecules inside and outside the cage molecule. This strategy is often used in the literature, e.g., in the study by Giri et al. MD simulations were performed at 350 K and 400 K,[83] and it helps ensure effective sampling of the phase space. The system's temperature was maintained using the V-rescale thermostat with a time constant of 0.1 ps. Electrostatic interactions were computed using the PME method with a real-space cutoff length of 1.4 nm and an FFT spacing of 0.12 nm. The neighbor list was updated every time step. The Lennard-Jones interactions were computed using direct summation with a cutoff at 1.4 nm. All bonds involving hydrogen atoms were constrained using the LINCS algorithm.[162] A time step of 1 fs was used. The center of mass motion for system was removed every 0.1 ps to avoid the drift of the porous liquids in the simulation box.

The cage molecule and solvent molecules were first packed into the middle section of the system using the Packmol code.[145] For each system studied, after equilibrating the porous liquids for 5 ns, gas molecules were inserted into the vacuum space at the two sides

of the porous liquid. This was followed by another 5 ns equilibration run for the gas molecules to reach equilibrium with the liquid phase. After that a 40 ns production run was performed. The trajectory of the system was saved every 1 ps for analysis (a video showing a sample trajectory of the CH_4+CO_2 system can be found in the Appendix B). To ensure that the gas partial pressure inside the gas bath matches the desired pressure within 2% deviation, we had to iteratively tune the number of gas molecules inside the *entire* system. To obtain reliable statistics, systems in which the partial pressure of gas species in the gas bath is lower than 20 bar were simulated 50 times with independent initial configurations; other systems were simulated 25 times with different initial configurations.

3.3 Results and Discussion

3.3.1 Cage molecule's accessible space.

We first examine the cavity space inside the cage molecule. The functional part of a cage molecule spans a radius of ~0.8 nm from its geometrical center. However, because of the steric exclusion by the cage's atoms, the accessible space for gas molecules within a cage molecule is limited to a radial distance of $\leq$ 0.5 nm from its geometrical center.[157] Figure 3-1e shows the volume rendering of this accessible space obtained by probing the cage's interior using an atom with a diameter of 0.28 nm, which roughly corresponds to the short axis of a N_2 molecule. We observe that, inside a cage molecule, the space available for gas storage consists of a non-spherical central cavity and four corridors connecting its interior to the outside solvents. Following our prior work,[157] we divided the accessible space within a cage molecule into a core region within 0.28 nm from the cage's center

(marked by yellow color in Fig. 3-1e) and a branch region spanning a radial distance of 0.28 to 0.5 nm from the cage's center (marked by red color in Fig. 3-1e).

3.3.2 Storage of pure gas molecules.

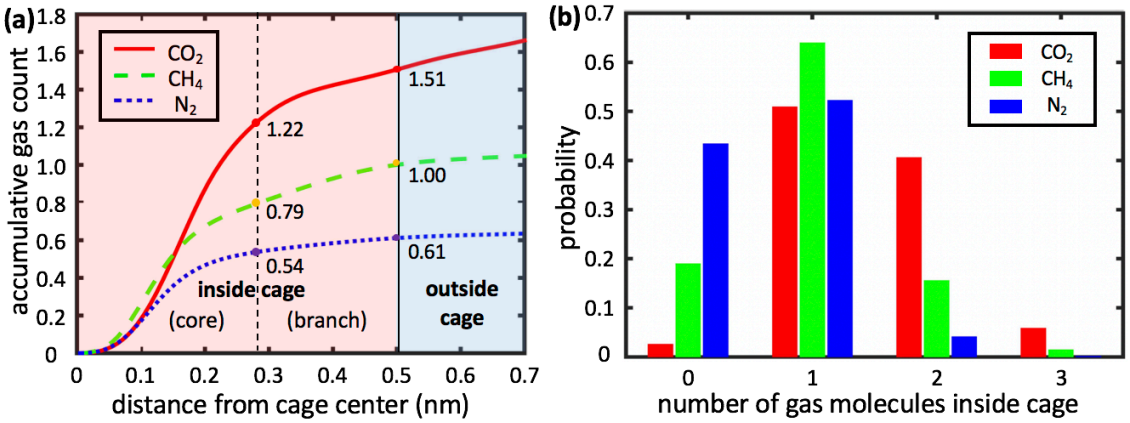

Figure 3-2. Gas storage in cage molecules dispersed in porous liquids exposed to a gas bath containing pure CO_2, CH_4, and N_2 with a pressure of 27.5 bar. (a) Accumulative gas molecule count as a function of the radial distance from the cage center. The vertical dashed line indicates the boundary between the core and branch regions of the cavity and the vertical solid line indicates the cage molecule's accessible space. (b) Probability distribution of the number of gas molecules inside a cage. The probability that four or more gas molecules occupy a single cage is <0.1% and thus not shown. The position of gas molecules is based on its center-of-mass.

Next we examine the storage capacity per cage molecule (CPC) when the porous liquids are in equilibrium with pure gas bath with a pressure of 27.5 bar. CPC is defined by the total accumulative count of gas molecules within the cage molecule's accessible space of 0.5 nm from its center. Figure 3-2a shows the accumulative count of gas molecules as a function of the distance from the cage center. The contribution from the core region toward CPC is found to be 1.22±0.02, 0.79±0.05, and 0.54±0.06, for pure CO_2, CH_4, and N_2, respectively, while the corresponding contribution from the branch region is found to be 0.29±0.01, 0.21±0.02, and 0.07±0.02. The net CPC is 1.51±0.04, 1.0±0.07, and 0.61±0.07, for CO_2, CH_4, and N_2, respectively. The core region contributes greatly to the

overall CPC while the contribution of the branch region is modest and depends on the gas stored. Specifically, for CO_2, CH_4, and N_2, the amount stored in the branch region is ~24%, 27%, and 13% of that stored in the core region, respectively.

As revealed in our earlier studies, the contribution of cage's core region toward CPC is controlled primarily by the nonelectrostatic gas-cage interactions for gas stored there.[157] The potential energy of a gas molecule stored in the core region due to its van der Waals interactions with the cage was found to be -22.2, -17.3, and -13.3 kJ/mol for CO_2, CH_4, and N_2, respectively. Hence, gas molecules are energetically favored in the core region in the order of CO_2 > CH_4 > N_2, in agreement with their core region's contribution. The contribution of the cage's branch region toward CPC is controlled by both the energetics of gas-cage interactions and entropic effects. For a gas molecule residing in the branch region, its potential energy due to interactions with the cage was found to be -19.5, -14.8, and -10.8 kJ/mol for CO_2, CH_4, and N_2, respectively. While the CO_2-cage interaction energy is still the most negative, CO_2 molecules in the branch region also experience the largest entropic penalty, which disfavors its storage in the branch region. The latter effect is caused by the fact that CO_2 molecules are longer than CH_4 and N_2 molecules and thus their rotation is hindered the most in the branch region.

In addition to the location that gas molecules are stored inside a cage molecule, we also examined whether, and how, multiple gas molecules co-exist inside a cage molecule. The histogram in Figure 3-2b shows the probabilities of 0, 1, 2 and 3 pure gas molecules being stored in a single cage. For all three gases, the probability that only one gas molecule is stored in a cage is the highest among all scenarios, while the probability that three (or more) gas molecules reside in the same cage is very low. However, for CO_2, the cage is

rarely empty (probability: 2.6%) and two molecules often reside in the same cage (probability: 40.6%). In contrast, for N_2, the cage is often empty (probability: 43.4%) and rarely filled with two molecules (probability: 4.1%). The situation for CH_4 lies in between N_2 and CO_2.

We note that the order of the cage's CPC for the molecules computed here ($\mathrm{CPC}_{\mathrm{CO}_2} > \mathrm{CPC}_{\mathrm{CH}_4} > \mathrm{CPC}_{\mathrm{N}_2}$) differs from that reported in our prior study ($\mathrm{CPC}_{\mathrm{CH}_4} > \mathrm{CPC}_{\mathrm{CO}_2} > \mathrm{CPC}_{\mathrm{N}_2}$).[157] The difference originates from the different system setups. In our previous work, there was no gas bath and the number of gas molecules in the porous liquids was the same for different gases. Therefore, the gas storage capacity of cage molecules computed from such a setup was affected by the partition of gas molecules between the cage molecule and solvents, and the result is appropriate for closed systems. For open system in which porous liquids are in contact with gas streams, the storage capacity of cage molecules computed in the present study is more practical.

3.3.3 Storage of multi-component gas molecules.

For multi-component gas storage, we start by examining gas adsorption inside the cage molecule when its host porous liquids are exposed to a 1:1 mixture of CO_2 and CH_4. Here the partial pressure of both gas components in the gas bath is 27.5 bar. Figure 3-3a shows the accumulative counts of CO_2 and CH_4 molecules in the cage molecule. From these data, the CPCs of CO_2 molecule is obtained as 1.33 ± 0.03, which is only 12% lower than the situation when the gas bath is filled with pure CO_2 with the same partial pressure. In comparison, the CPC of CH_4 molecule is significantly reduced to 0.31 ± 0.04, i.e., 69% lower than that for pure CH_4. Therefore, the cage molecule exhibits a high selectivity toward these two molecules. To quantify this selectivity, for a cage in equilibrium with a

gas bath containing a mixture of gas molecules A and B, we introduce a selectivity coefficient $S_{A/B}$ for the cage molecule as

$$S_{A/B} = \left(\frac{\mathrm{CPC}_A}{\mathrm{CPC}_B}\right) \Big/ \left(\frac{p_A}{p_B}\right) \tag{3-1}$$

where p_A and p_B are the partial pressure of molecules A and B in the gas bath. It follows that the cage molecule studied here gives a selectivity coefficient of $S_{\mathrm{CO_2/CH_4}} = 4.3$. It should be noted that this $S_{\mathrm{CO_2/CH_4}}$ is specific to the partial pressure of the two gases studied. However, given that the research on the selectivity of cage molecules for different gas molecules is at a very early stage at present, we defer the systematic investigation of how $S_{\mathrm{CO_2/CH_4}}$ varies with the partial pressure of molecules in the gas bath to future studies.

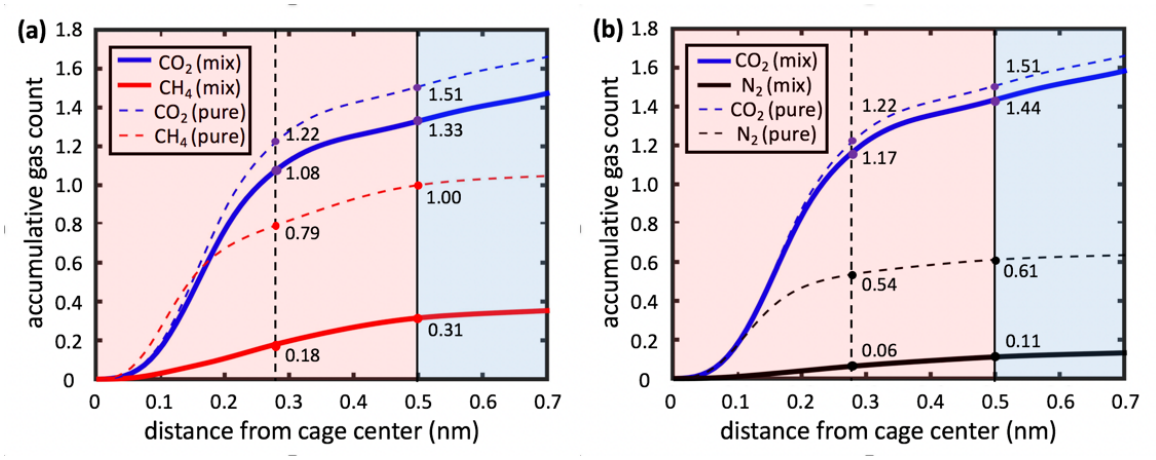

Figure 3-3. Accumulative gas molecule count as a function of radial distance from the center of the cage molecule in equilibrium with a gas bath containing a mixture of CO_2 and CH_4 molecules (a) and a mixture of CO_2 and N_2 molecules (b). Results for a gas bath containing pure CO_2, CH_4, and N_2 gas are shown using thin dashed curves. The vertical dashed line indicates the boundary between the core and branch regions of the cavity and the vertical solid line indicates the cage molecule's accessible space. The partial pressure of all gas in the gas bath is 27.5 ± 0.3 bar.

To understand what contributes to the different storage capacity of the cage for the CO_2 and CH_4, we analyze the density isosurface of these molecules inside the cage. Figure 3-4 shows the results when the cage is in equilibrium with gas baths containing pure CO_2,

pure CH_4 and a mixture of CO_2 and CH_4. The isosurface is set to a density value of 15 nm^{-3}, which is high enough so that the isosurface highlights the region where gas molecules are concentrated. We observe that the high density zone of CO_2 molecules inside the cage changes little when we move from the adsorption of pure CO_2 to CO_2+CH_4 mixtures. However, when we move from adsorption of pure CH_4 to CO_2+CH_4 mixtures, the high density zone of CH_4 in the cage's core region disappears and the high density zone in the cage's branch region shrinks marginally. Therefore, when CO_2 and CH_4 are both present, there is little effect on the adsorption of CO_2 molecules in the cage. The competition from CO_2 molecules drives CH_4 molecules out of the cage's core region, but hardly affects CH_4 adsorption in the cage's branch region. Overall, the cage molecule's selectivity of CO_2 over CH_4 is mostly contributed by the depletion of CH_4 by CO_2 from the cage's core region.

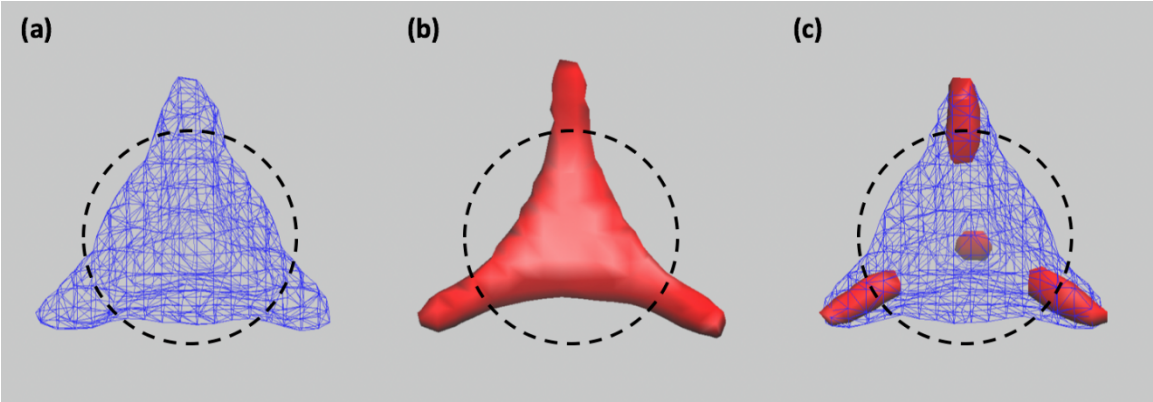

Figure 3-4. Isosurface of CO_2 (blue) and CH_4 (red) gas density inside a cage molecule in equilibrium with a gas bath containing pure CO_2 (a), pure CH_4 (b), and a mixture of CO_2 and CH_4 molecules (c). The isosurface is set to a density of 15 nm^{-3}. The black dashed circle marks the boundary between the cage's core region and branch regions. The partial pressure of all gas in the gas bath is 27.5 ± 0.3 bar.

Next we examine whether, and how, a cage molecule can accommodate more than one molecule. This will not only help understand the gas storage capacity of a cage but also help delineate the state of the gas molecules confined inside the cage. Table 3-1 shows the probability of finding different numbers of CO_2 and CH_4 molecules inside one cage

molecule in equilibrium with a gas bath containing a 1:1 CO_2+CH_4 mixture. With the gas partial pressure adopted here, while a cage molecule most likely accommodates one CO_2 molecule (probability: ~38%), it also frequently hosts two or more gas molecules (probability: ~54%). In particular, the probabilities of finding two CO_2 molecules or one

Table 3-1. The probability of finding different numbers of gas molecules inside a cage in equilibrium with a gas bath containing a mixture of CO_2+CH_4 (P_{CO2}=P_{CH4}=27.5 bar). The shaded cells denote situations in which the cage is occupied by multiple gas molecules.

		N(CH_4) [c]			
		0	1	2	≥3
N(CO_2) [b]	0	1.5	6.3	1.4	x
	1	38.0	13.6	1.5	x
	2	28.5	4.8	x	x
	3	3.8	x	x	x
	≥4	X	x	x	x

a "x" means the probability is less than 0.5%.
b Number of CO2 molecules in the cage.
c Number of CH4 molecules in the cage.

CO_2 molecule and one CH_4 molecule inside a cage are ~29% and ~14%, respectively. To clarify where these molecules are stored inside the cage when double occupancy occurs, we computed their distribution inside the cage as a function of distance from the cage center. As can be seen from the results shown in Figure 3-5a, when two CO_2 molecules reside inside the cage, both molecules favor the cage's core region. On the other hand, when two CH_4 molecules reside in a cage, one of them prefers its core region while the other one prefers its branch region (Fig. 3-5b). When one CO_2 molecule and one CH_4 molecule reside in a cage, the CO_2 molecule occupies predominately the core region while the CH_4 molecule is found both in core and branch regions (Fig. 3-5c). These results are consistent with the accumulated gas count data shown in Figure 3-3a.

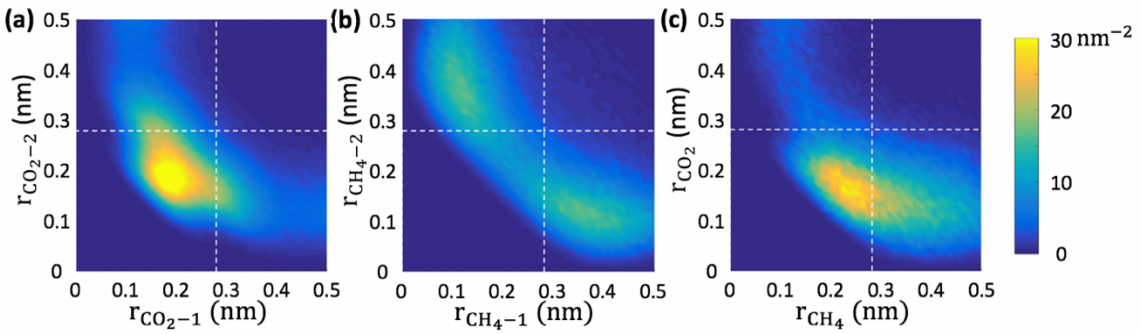

Figure 3-5. Probability density of the radial distribution of gas molecules inside a cage in equilibrium with a gas bath containing a mixture of CO_2 and CH_4 (P_{CO2}=P_{CH4}=27.5 bar). (a) When two CO_2 molecules reside in the cage. (b) When two CH_4 molecules reside in the cage. (c) When one CO_2 molecule and one CH_4 molecule reside in the cage. The axis labels r_A and r_B denote the radial position of molecule A and B inside the cage. The white dashed lines denote the boundary between the core and branch regions inside the cage.

Overall, when a porous liquid is exposed to a mixture of CO_2 and CH_4 gases, CO_2 molecules adsorb more readily into its cage molecules than the CH_4 molecules, often with two or more CO_2 molecules residing in each cage's core region. Displaced by these CO_2 molecules, the adsorption of CH_4 molecules in the core region is greatly reduced while that in the branch is reduced modestly. Hence the contribution of the core region and branch region to the storage of CH_4 molecules in a cage is comparable, which differs greatly from the adsorption of pure CH_4. The high occupancy of CO_2 in the core region and its ability to displace CH_4 from this region can be understood as follows. In the core region, a CO_2 molecule's potential energy due to its interaction with the cage (-22.2 kJ/mol) is considerably more negative than that for a CH_4 molecule (-17.3 kJ/mol). This helps multiple CO_2 molecules to be packed into the core region and effectively displace CH_4 molecules. In the branch region, CO_2 molecules only marginally displace the CH_4 molecules because, although CO_2 molecules are again energetically more favored than CH_4 in this region, they suffer larger entropic penalty because their rotation is restricted in the narrow branch region.[157]

The above discussion suggests that the selectivity of the cage toward different gas molecules is controlled primarily by the gas-cage interaction energies of different gases molecules, and to a lesser extent by the entropic penalty of different molecules in the branch region. While the cage exhibits a modest selectivity for CO_2 over CH_4, we expect that a stronger selectivity can be achieved if the CH_4 molecule is replaced by a molecule that interacts more weakly with the cage and experiences more entropy penalty in the branch region than the CH_4 molecules. The former conditions are satisfied by N_2 molecules. Figure 3-3b shows the accumulative counts of the CO_2 and N_2 molecules in a cage molecule in equilibrium with a gas bath in which the partial pressure of both CO_2 and N_2 are 27.5 bar. From these data, the CPCs of CO_2 and N_2 molecule are obtained as 1.44 ± 0.05, and 0.11 ± 0.05, respectively, which gives a selectivity of $S_{CO_2/N_2} = 13.1$. This very high selectivity is caused mainly by two factors. First, N_2 molecules are almost fully displaced from the core region by the CO_2 molecules (see Fig. 3-3b and Fig. B-2 in Appendix B). Second, the adsorption of N_2 molecules in the branch region is low even without the competition from CO_2 molecules (see Fig. 3-2a).

Thus far, we focused on the gas storage inside cage molecules in equilibrium with gas baths with a specific partial gas pressure. It is also essential to know how the selectivity of the cage varies with partial gas pressure. Using the second set of simulations described in Section 2, we computed the adsorption isotherm of the cage molecule in equilibrium with a gas bath containing 1:1 CO_2+CH_4 mixture (i.e., $P_{CO_2} = P_{CH_4}$). Figure 3-6a shows the CPCs of CO_2 and CH_4 at different partial gas pressures. Over the range of partial pressures explored, CO_2 is always more competitive than CH_4 in adsorbing in the cage, which is consistent with our observation made at gas partial pressure of 27.5 bar. Figure 3-6b shows

the selectivity of the cage molecule for CO_2/CH_4 pair. At partial pressure of 9 ~ 27.5 bar, the variation of the cage's selectivity of CO_2 over CH_4 is within the statistical uncertainty. However, as the partial pressure increases to 54 bar, the selectivity of CO_2 over CH_4 decreases slightly, which we attribute to the entropic effect. Specifically, as the partial pressure increases, the cage becomes packed with more gas molecules, which imposes an entropic penalty for gas adsorption inside the cage. Such an entropic penalty is more significant for the bulkier CO_2 molecules than for the CH_4 molecule. We note that similar mechanism has been used to explain why the bulkier C_2H_6 molecules become less competitive in adsorbing in zeolites compared to the smaller CH_4 molecules.[163-164]

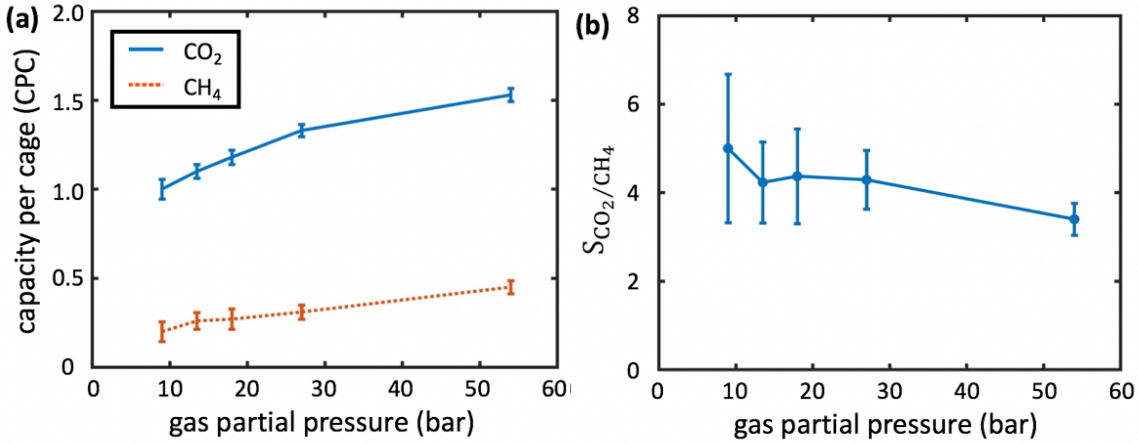

Figure 3-6. (a) The adsorption isotherm of CO_2 and CH_4 molecules in an organic cage molecule in equilibrium with a gas bath containing 1:1 CO_2+CH_4 mixture. (b) The selectivity of the cage molecule for the CO_2/CH_4 pair.

3.4 Conclusion

In summary, we have examined the storage of three prototypical small molecules (CO_2, CH_4, and N_2) and their binary mixtures within organic cage molecules using MD simulations. In all cases, the cage was in equilibrium with a gas bath, and the partial pressure of each type of molecule in the gas bath was kept the same. For a partial pressure

of 27.5 bar, a cage molecule gives a selectivity of 4.3 and 13.1 for the CO_2+CH_4 and CO_2+N_2 pairs, respectively. The selectivity of CO_2 over CH_4 and N_2 is attributed to its stronger van der Waals interactions with the cage, which helps CO_2 molecules displace CH_4/N_2 molecules from the cage's core region. Nevertheless, CO_2 molecules do not effectively displace CH_4/N_2 molecules from the cage's branch region because they suffer a larger entropic penalty due to the restriction of their rotational motion therein. For both CO_2+CH_4 mixture and CO_2+N_2 mixture, the cage was often occupied by more than one gas molecule. While the storage of two CO_2 molecules in the cage's core region occurred most frequently, situations in which one CO_2 molecule occupies the core region and one CH_4/N_2 molecule occupies the branch/core region also occurred. The study of adsorption isotherm for CO_2+CH_4 mixture suggests that the selectivity of CO_2 over CH_4 decreases slightly as gas partial pressure increases because of the entropic effect.

The cage selectivity revealed by our simulations suggests that the existing porous liquids may be effective for separating CO_2 and N_2 and thus useful in carbon capture applications. However, for separating CO_2 and CH_4, which is needed in applications such as shale gas processing, the performance of the current cage molecule remains to be improved. One possible method is to engineer new cage molecules to further enhance their interactions with the CO_2 molecules without notably enhancing the CH_4-cage interactions. Since CO_2 has a large quadrupole moment while CH_4 has zero quadrupole moment, this may be achieved by introducing functional motifs within the cage that carry significant partial charge. However, such motifs must be approached closely by the CO_2 molecules since charge-quadrupole interactions are short-ranged.

Supporting Information Available in Appendix B: The density of gas molecules across the simulation box for all systems studied and the density isosurface of CO_2 and N_2 molecules inside the cage molecule when the cage is in equilibrium with gas baths containing pure CO_2, pure N_2, and 1:1 CO_2+N_2 mixture, and a trajectory video for the simulation of CO_2+CH_4 mixture.

Chapter 4: Effects of Water on Mica-Ionic Liquid Interfaces

Disclosure

This work has been published by the American Chemical Society: F. Zhang, C. Fang, and R. Qiao, "Effects of Water on Mica–Ionic Liquid Interfaces", The Journal of Physical Chemistry C, 122, 216, 2018.

4.1 Introduction

Pure room-temperature ionic liquids (RTILs) consist of only ions but remain in the liquid state at temperature below 100°C.[93-94] Because the molecular structure and combination of the cations and anions in RTILs can be tailored relatively easily and many RTILs offer properties such as wide electrochemical window, low vapor pressure, and excellent thermal stability, RTILs have shown great promise in applications such as capacitive energy storage and lubrication.[2-9] The performance of RTILs in many of these applications depends greatly on the interfacial structures of RTILs near solid surfaces.[93] Therefore, it is essential to gain a fundamental understanding of these interfacial structures.

The interfacial structures of RTILs near solid surfaces have been investigated extensively using experimental,[3, 95-102] theoretical,[81, 103-106] and simulation methods.[9, 78-79, 107-117] For example, it is now established that, near charged solid surfaces, cations and anions form alternating layers extending into the RTILs and the surface charges are often overscreened.[78, 165] Interfacial RTILs also exhibit ordering in the lateral directions, thereby making the electrical double layers near charged surfaces three-dimensional (3D) entities.

The 3D structure of interfacial RTILs can be modified by factors such as surface charge and confinement.[3, 129-133] Few of these studies, however, paid attention to the possible existence of water in RTILs and how the interfacial structures of RTILs are affected by the water. In reality, most RTILs are hygroscopic and can absorb noticeable amount of water from the environment.[118] Since 2014, these issues have received significant attention.[101-102, 105, 119-125] For example, using molecular dynamics (MD) simulations, Feng *et al*. showed that, compared to that in bulk RTILs, water molecules are greatly enriched near electrified graphene surfaces and the level of enrichment depends both on the surface charge and the choice of RTILs (in particular the counterions near the electrified surfaces).[120] On the experimental front, Gong *et al*. showed that RTILs form extended layers on a mica surface in ambient environment with a finite relative humidity (hence there is a finite adsorption of water at RTIL-mica interfaces).[128] Under elevated temperature and when the water on the mica surface are displaced by airborne hydrocarbons, RTILs experience dewetting on the mica surface and form droplets. To explain these observations, they hypothesized that, in presence of water, mica's surface K^+ ions desorb and exchange with the cations in the RTILs, which triggers the ordered packing of alternating layers of cations and anions near the mica surface, and consequently the extended layering of RTILs. Independently, Cheng *et al*. examined how water affects the interfacial structure of $[C_2mim][Tf_2N]$ liquids near mica surfaces and electrified gold surfaces. Based on surface force measurements, they also suggested that the water molecules adsorbed at the mica-RTIL interfaces profoundly alter the interfacial structure of RTILs by enabling the electrification of the mica surfaces. This idea was further developed in a follow-up study,[102] in which the interfacial structure

of RTILs and water was again inferred from the interaction force vs. separation curves obtained using atomic force microscopy (AFM) and surface force apparatus (SFA).

The great impact of water on the interfacial structure of RTILs reported in these studies has been observed in more recent studies,[123-124, 126] and it has been further shown that water also significantly modifies other macroscopic observables such as the capacitance of double layers near electrodes.[105] While the importance of water on interfacial structure of RTILs is generally recognized, difference in opinion does exist. For example, based on a study of mica-propylammonium nitrate (PAN) interfaces using amplitude modulated atomic force microscopy, McDonald *et al*. suggested that the adsorption of water at mica-RTIL interfaces is not essential for the electrification of mica surfaces in contact with some RTILs.[127]

The above experimental and simulation studies triggered many simulation studies of the solid-RTIL interfaces in presence of water. Among all solids, mica offers an ideal model surface and muscovite mica surface is one of the most studied surfaces. Muscovite ($KAl_2Si_3AlO_{10}(OH)_2$) is a phyllosilicate clay with a tetrahedral-octahedral-tetrahedral (TOT) structure. In the muscovite layer, each Al-centered octahedral sheet is sandwiched between two Si-centered tetrahedral sheets, in which every four Si atoms is substituted by Al atoms. The structure thus resulted carries negative charge, which is compensated by the K^+ ions. Neighboring TOT structures are held together by a potassium interlayer and can be cleaved from the (001) plane to form a surface featuring K^+ ions.[166-167]

Previous work suggested that water alter the RTIL structure at mica surfaces.[101-102, 128] However, directly visualizing the change of interfacial RTIL structure experimentally is difficult, and the available experimental insight on such structure change is mostly inferred

indirectly from other macroscopic observables such as the force vs. distance curves. Such a limitation can be addressed using MD simulations. At present, such simulations are rather limited [121, 125] and only two of them deal with mica surfaces. Fajardo *et al.* [121] investigated effect of hydration on interfacial structure of [BMIM][PF_6] confined in a 1.8-nm gap formed by two charged mica surfaces. They found that water is adsorbed at the interface and the orientation of $BMIM^+$ ions changes as the water loading in bulk RTIL increases. Zhang *et al.* [125] studied the effects of different types of RTILs and concentration of water molecules on RTIL-mica interfaces. They found that, with water accumulated at the mica-RTIL interfaces, RTILs are slightly displaced away from the surface. While these studies offered critical insights on how water modifies the structure of mica-RTIL interfaces, they focused mostly on the distribution of ion and water molecules normal to the mica surface and limited attention has been paid to the 3D structure of *RTILs and water* near open mica surfaces. Understanding the 3D structure of RTILs and how it is affected by the water is important because recent experimental and simulation studies revealed that RTILs can exhibit rich 3D structures near solid surfaces.[3, 93, 129-133]

In this work, we investigate the interfacial structure of [BMIM][Tf_2N] near mica surfaces using MD simulations. Using atomistic models, we explore the effects of water and surface charging on the 3D structure of RTIL near the mica surfaces. The rest of this manuscript is organized as follows. Section 4.2 describes the simulation system and methods. Section 4.3 presents the interfacial structure of [BMIM][Tf_2N] and how it is affected by surface charge and water. Finally, conclusions are drawn in Section 4.4.

4.2 Simulation System, Models, and Methods

System. We focus on the interfacial structure of RTILs near muscovite mica surfaces in two types of systems. In the first type, a thick film of [BMIM][Tf_2N] is placed on a slab of mica, whose surface is neutral. The system is either free of water (Fig. 4-1a) or features a small amount of water (Fig. 4-1b). These systems mimic the initial stage of a freshly cleaved mica surface in contact with dry or humid RTILs. Studying these systems can lay foundation for understanding the electrification of mica surfaces, which involves the dissociation of the surface K^+ ions from mica surfaces.

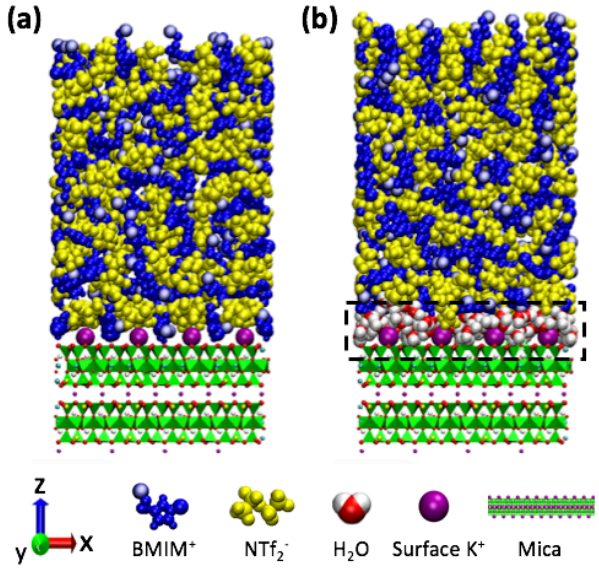

Figure 4-1. Snapshots of the MD systems for studying the structure of [BMIM][Tf_2N] near neutral mica surfaces in absence of (a) and in presence of (b) water in the interfacial zone.

In the second type of system, a thick film of [BMIM][Tf_2N] is placed on a slab of mica, whose surface K^+ ions are all removed and not included in the MD system. The charge of the mica surface is neutralized by an extra number of $BMIM^+$ ions in the liquid film. These systems mimic the situation in which fully electrified mica surfaces (surface charge density σ is -0.33 C/m^2) are in contact with RTIL baths. Note that in this situation, the charge of a mica surface is screened by the ions of the RTILs due to their overwhelming

abundance compared to the K^+ ions dissociated from the mica's surface. Same to the first type of system, this second type of system can be either free of water or contain a small amount of water.

All simulation systems measure 3.15×3.67 nm^2 in the plane of the mica surface (*xy*-directions) and 15nm in the direction normal to the mica surface (*z*-direction). In systems with neutral mica surfaces and dry RTIL, 115 pairs of [BMIM][Tf_2N] ions are placed on the mica slab, resulting in a ~6nm-thick liquid layer. Such a liquid layer is thick enough that the RTILs in the middle of the film is neutral and the structure of the RTILs near the mica surface is not affected by the RTIL-vacuum interface. In simulations with charged mica surface, there are 139 $BMIM^+$ ions and 115 Tf_2N^- ions in the system.

To study the effect of water on the interfacial structure of RTILs, we introduce 160 water molecules into the RTIL-mica interfacial zone (cf. the black box in Fig. 4-1b) for systems with neutral or charged mica surface. Our simulations show that these water molecules remain in the interfacial zone during production runs of tens of nanoseconds in length. The relative humidity of the virtual ambient environment (T=300K) with which the interfacial water is in equilibrium can be computed using (see Appendix C for derivation)

$$\mathrm{RH} = \frac{k_B T \rho(z_0)}{p_0} \exp\left(\frac{\phi(z_0)}{k_B T}\right) \tag{4-1}$$

where $\rho(z_0)$ is the water density at a reference point z_0 in the RTIL film. $\phi(z_0)$ is the potential of mean force (PMF) of a water molecule at this point relative to that at a position outside of the RTIL film. k_B is the Boltzmann constant, and p_0 =3.524kPa is the saturated vapor pressure of water at 300K. $\phi(z_0)$ is obtained by computing the PMF of water molecules in *separate* simulations, where water molecules are constrained at a series of

positions across the RTIL film and the Umbrella sampling method is used to extract their PMF (see Appendix C).

Models. Each mica slab is modeled as two muscovite layers, resulting in a total thickness of ~2nm. The PCFF force fields are used to describe the mica,[168-169] and water molecules are described using the flexible SPC model.[170] [BMIM][Tf_2N] is modeled using the force fields developed in Ref. [171]. The force field parameters for the non-bonded interactions between RTIL and mica/water are summarized in Table C-1.

Simulation protocol and method. To build the simulation system, water molecules are placed on the mica surface and RTILs are packed in the region 1nm above the mica surface using the Packmol code.[145] An equilibrium run of 10ns is then performed, during which the RTILs gradually come into contact with the water molecules and mica surface. This is followed by a production run of 40ns, during which the trajectory is saved every 1ps.

MD simulations are performed in the NVT ensemble using the LAMMPS code.[172] The temperature of the system is maintained at 300K using the Nose-Hoover thermostat.[173] A time step of 2 fs is used and the neighbor list is updated every step. The bonds in the RTILs involving H atoms are constrained using the Shake algorithm. The cutoff for the non-electrostatic interactions is 1.2nm. The electrostatic interaction is computed using the PPPM method.[174] While the system is periodic in all directions, the slab correlation has been applied in the calculation of electrostatic interactions to effectively remove the periodicity in the direction normal to the mica surface.

4.3 Results and Discussion

4.3.1 Interfacial structure near neutral mica surfaces

We first examine the case where the interfacial zone contains no water. Figure 4-2a shows the density profiles of ions near the mica surface. The position of the $BMIM^+$ (Tf_2N^-) ion is based on the geometrical center of its imidazole ring (nitrogen atom). The strong peaks at z=0.39 and 0.48nm indicate that $BMIM^+$ and Tf_2N^- ions adsorb roughly in a single layer on the mica surface, with the $BMIM^+$ ions slightly closer to the mica. The second density peak of the $BMIM^+$ (Tf_2N^-) ion appears at z=1.16nm (1.31nm), which is much lower than its first peak. At larger distance from the mica surface, density peaks of both ions diminish. These results suggest that beyond the first ion adsorption layer, the layering of both ions is weak.

Since the adsorption of the first cation and anion layers on the mica is strong, we examine the organization of these adsorbed ions. Figure 4-2 b-d show the top, bottom, and side views of the $BMIM^+$ and Tf_2N^- ions located in their first density peaks. The $BMIM^+$ ions are mostly adsorbed in the interstitial space between the surface K^+ ions, likely due to their affinity to the mica's negatively charged basal oxygen atoms. The Tf_2N^- ions are primarily located above the surface K^+ ions, which explains why the density peak of the Tf_2N^- ions is slightly further away from the mica surface than that of the $BMIM^+$ ions. The adsorbed $BMIM^+$ ions exhibit some orientation ordering. To quantify this ordering, we compute the probability distribution of the orientation of the $BMIM^+$ ions' imidazole rings and butyl tails, i.e., $P(\cos\theta)$ and $P(\cos\alpha)$, where θ (α) is the angle formed by the normal vector of the imidazole ring (the vector pointing from the first to the last carbon atom of

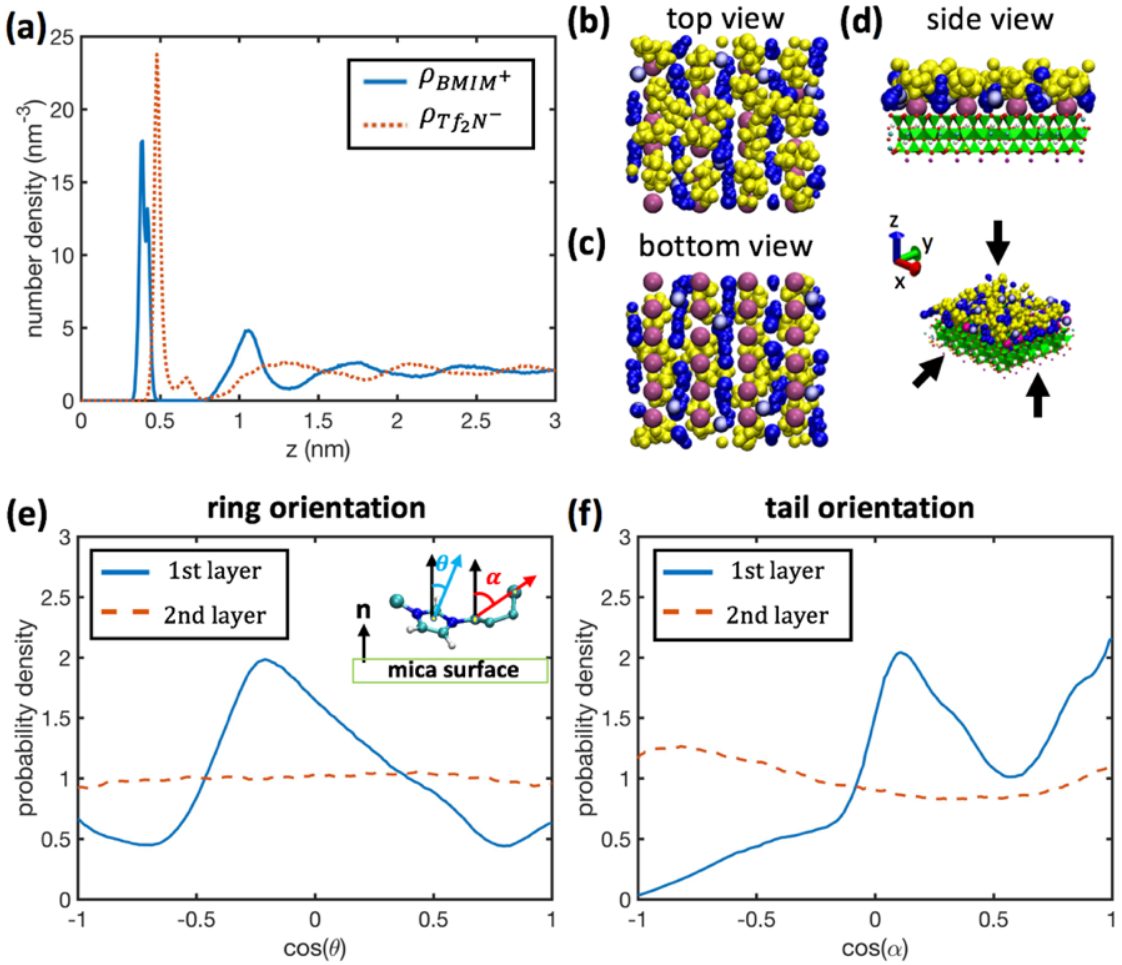

Figure 4-2. *Structure of [BMIM][Tf_2N] liquids near a dry mica surface with a zero net charge density*. (a) The density profiles of the cations and anions. The position of the cation (anion) is based on the geometrical center of its ring (its nitrogen atom). (b-d) The top, bottom and side views of the first layer of cations and anions near the mica surface. The color coding of different species is shown in Fig. 4-1. The last atom on the cation's hydrophobic tail is shown in light blue. (e-f) The probability density distribution of the orientation of the ring (e) and tail (f) of the first and second layer of $BMIM^+$ ions near the mica surface with respect to the normal direction of the mica surface.

the butyl tail) and the normal vector of the mica surface (see Fig. 4-2 e-f). These $BMIM^+$ ions' imidazole rings prefer to orient normal to the mica surface (Fig. 4-2e); their tails prefer to lie parallel to the mica's surface or point into the bulk liquids (Fig. 4-2f). Figure 4-2 e-f also shows that, for the $BMIM^+$ ions in the second layer near the mica, their orientation ordering almost vanishes. These results show that, while the interfacial $BMIM^+$ ions exhibit modest structural ordering, this ordering is limited to the adsorption layer. These observations are in line with the study by Cheng *et al*, in which it was suggested that dry RTILs near freshly cleaved mica exhibit very weak structuring.[101-102]

We next examine the mica-RTIL interface when water is introduced to the interfacial zone. As described above, 160 water molecules are initially placed over the mica surface. Figure 4-3a shows their density distribution near the mica surface during the last 40ns of our 50ns simulation. The water density at z>1.0nm is nearly zero, indicating that all water molecules remain in the interfacial zone. This is expected: since the load of water in the system far exceeds its solubility in the RTILs, water must be phase separated from the bulk RTILs. Here, water molecules are accommodated on the solid substrate as a thin film because they are stabilized by the hydrophilic mica and, to a less extent, the interfacial RTILs (see below). If the substrate is less hydrophilic, water may phase separate from the bulk RTILs in other forms, e.g., if we remove the partial charge on the mica atoms to make the mica less hydrophilic, the water introduced into the system will form a droplet rather than a thin film on the mica surface (see Fig. C-4).

The first and second water peaks appear at z=0.19 and 0.30nm, respectively. The bottom and side views of interfacial zone indicate that the first peak of water corresponds

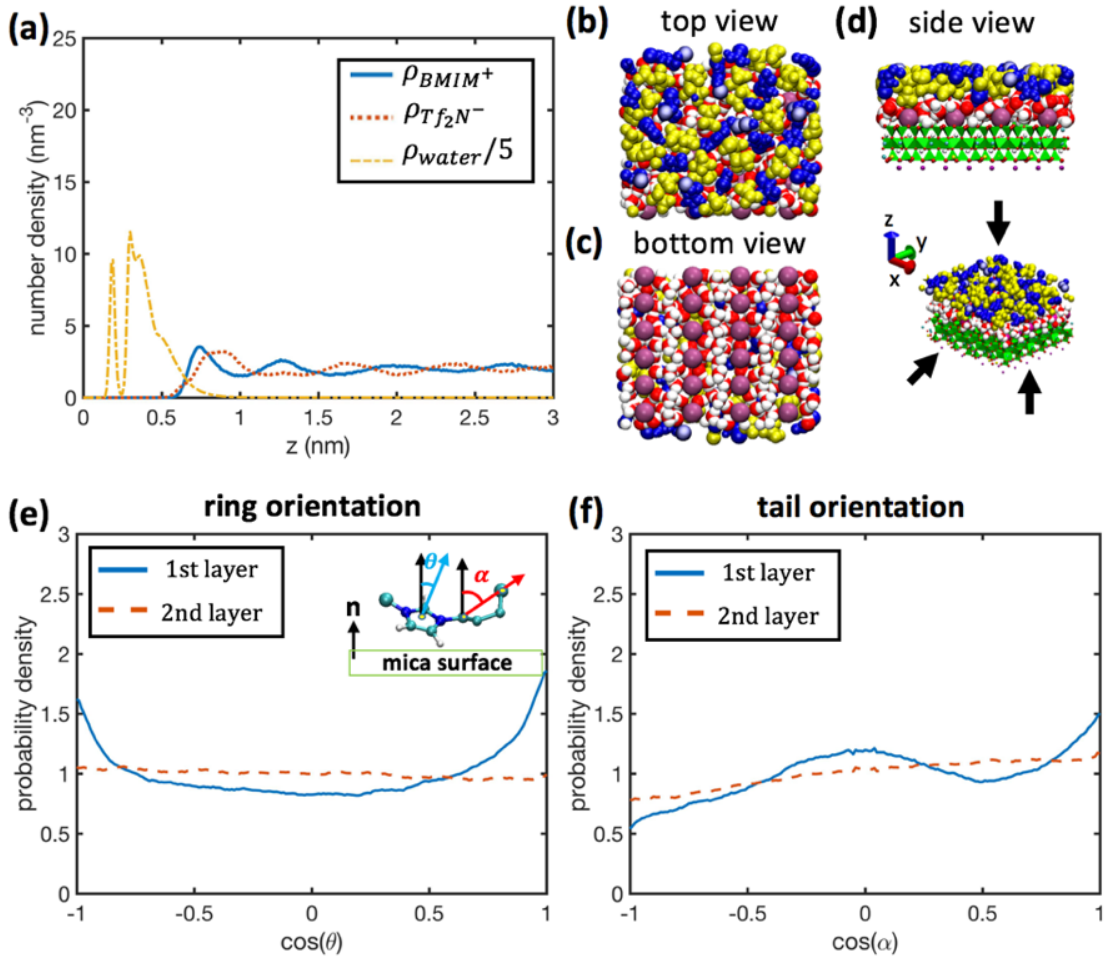

Figure 4-3. *Structure of [BMIM][Tf_2N] liquids and water near a neutral mica surface with a zero net charge density*. (a) The density profiles of the cations, anions, and water molecules. The density of water is scaled by a factor of five, and the position of the water molecules is based on their oxygen atom. (b-d) The top, bottom and side views of the first layer of cations and anions and all water molecules near the mica surface. (e-f) The probability density distribution of the orientation of the ring (e) and tail (f) of the first and second layer of $BMIM^+$ ions near the mica surface with respect to the normal direction of the mica surface.

to the water molecules interacting with the basal oxygen and the second peak of water corresponds to the water molecules hydrating the surface K^+ ions (see Fig. 4-3c and Fig. 4-3d). Figure 4-3a also shows that the layer of $BMIM^+$ and Tf_2N^- ions adsorbed on the dry mica surface disappears. Instead, the first peaks of the $BMIM^+$ and Tf_2N^- ions appear at z = 0.75 and 0.88nm, respectively, and are only modestly higher than the density in bulk liquids. These first peaks are close to each other, suggesting that the charge separation near the mica surface is negligible. The $BMIM^+$ ions in the first density peak exhibits weak orientation ordering, with their ring slightly preferring a co-planar configuration with the mica surface (Fig. 4-3e) and their tail parallel to the mica surface or pointing to the bulk liquids (Fig. 4-3f). The top view of the interfacial zone (Fig. 4-3b) further indicates that the first layer of $BMIM^+$ and Tf_2N^- ions near the mica surface are well mixed, with both ions showing no preferred orientation in the horizontal plane. The comparison of these results with the interfacial structure near dry mica surfaces (see Fig. 4-2) shows that, as water appears at a *neutral* mica-RTIL interface, the layering of RTILs in the z-direction and their lateral structuring are greatly weakened and the interfacial RTILs appear to be bulk-like.

The above results show that, when water molecular are introduced into the interfacial zone, they outcompete the $BMIM^+$ and Tf_2N^- ions in terms of adsorption on the mica surface. In fact, the water molecules completely displace the $BMIM^+$ and Tf_2N^- ions adsorbed on the mica surface and shifted their density peaks away from the mica surface by ~0.4nm. The small size and the dipolar nature of the water molecules are essential for these observations. For a water molecule in the interfacial zone, it shows strong affinity to both the surface K^+ ions (via charge-dipole interactions) and the negatively charged basal oxygen atoms (via hydrogen bonding).[125] The $BMIM^+$ and Tf_2N^- ions, both bulky and

carrying delocalized charge, only show affinity to the basal oxygen and surface K^+ ions, respectively. This difference, along with the fact the ion-mica interactions are screened by the water molecules in the interfacial zone, enables water molecules to displace both ions from the mica surface and become the major molecule solvating the surface K^+ ions. Once water displaces the ionic layers adsorbed on the mica surface, these ions essentially "float" on a molecularly thin film of water. Because the mica surface carries no net charge, neither $BMIM^+$ nor Tf_2N^- ions are attracted to or repelled from it strongly. This, along with the molecular roughness of the thin water film, makes it difficult for these ions to exhibit long-range ordering in both lateral and vertical direction of the mica surface. Consequently, the interfacial ions exhibit much weaker structuring compared to those near dry mica surfaces.

The effects of water on the interfacial structure of RTILs revealed in the above calculations are specific to the water area density at the mica surface adopted here (or equivalently, the relative humidity of the virtual ambient environment, see below). For example, we can expect the first peak of both cations and anions to move closer to the mica surface if a lower water area density is used. Nevertheless, the qualitative aspects of water's effects revealed here should remain, e.g., the weakening of the interfacial structure as water is introduced at the mica-RTIL interfaces.

Using Equation 4-1, the relative humidity of the virtual ambient environment, with which the water molecules of our mica-water-RTIL system is in equilibrium, is found to be $20.5 \pm 11.3\%$ (see Appendix C). Because nearly all water molecules accumulate near the mica surface, the area density of interfacial water in the present mica-water-RTIL system is 13.8 nm^{-2}. For a bare mica surface exposed to an ambient environment, this area density is obtained when its relative humidity is 76%.[167] Introducing a [BMIM][Tf_2N] film

on a mica substrate therefore *enhances* the adsorption of water on its surface. This enhancement is a synergistic effect of two factors. First, water molecules outcompete bulky ions in adsorbing on the mica surface. Second, because the $BMIM^+$ and Tf_2N^- ions near the mica surface can interact with interfacial water molecules via van der Waals and electrostatic forces, these ions provide an energetically more favorable microenvironment for the adsorption of water molecules than the vacuum space above a bare mica surface.

The favorable adsorption of water at mica-RTIL interfaces has practical implications. If not all surface K^+ ions of a mica surface immersed in dry RTILs are dissociated from the mica lattice, then even exposing the RTILs to an environment with low relative humidity will lead to significant adsorption of water on the mica surface. The observation that the surface K^+ ions of mica are readily hydrated by the adsorbed water molecule (Fig. 4-3d) suggests that, similar to the situation of a mica surface immersed in water, surface K^+ ions may dissociate from the mica lattice and thus leaving the mica surface electrified. Hence, we further explore the effect of water on the interfacial structure of RTILs near electrified mica surfaces.

4.3.2 Interfacial structure near charged mica surfaces

We first examine the case where the interfacial zone is free of water. Figure 4-4a shows the ion density profiles near the mica surface. Three closely positioned peaks, corresponding to a layer of adsorbed $BMIM^+$ ions with different orientations, are observed at z=0.30, 0.36, and 0.41nm. This $BMIM^+$ layer is followed by a diffuse Tf_2N^- ion layer centered at z=0.93nm. The clear separation of the first $BMIM^+$ and Tf_2N^- ion layers highlights the strong charge separation near the charged mica surface. Alternating layers

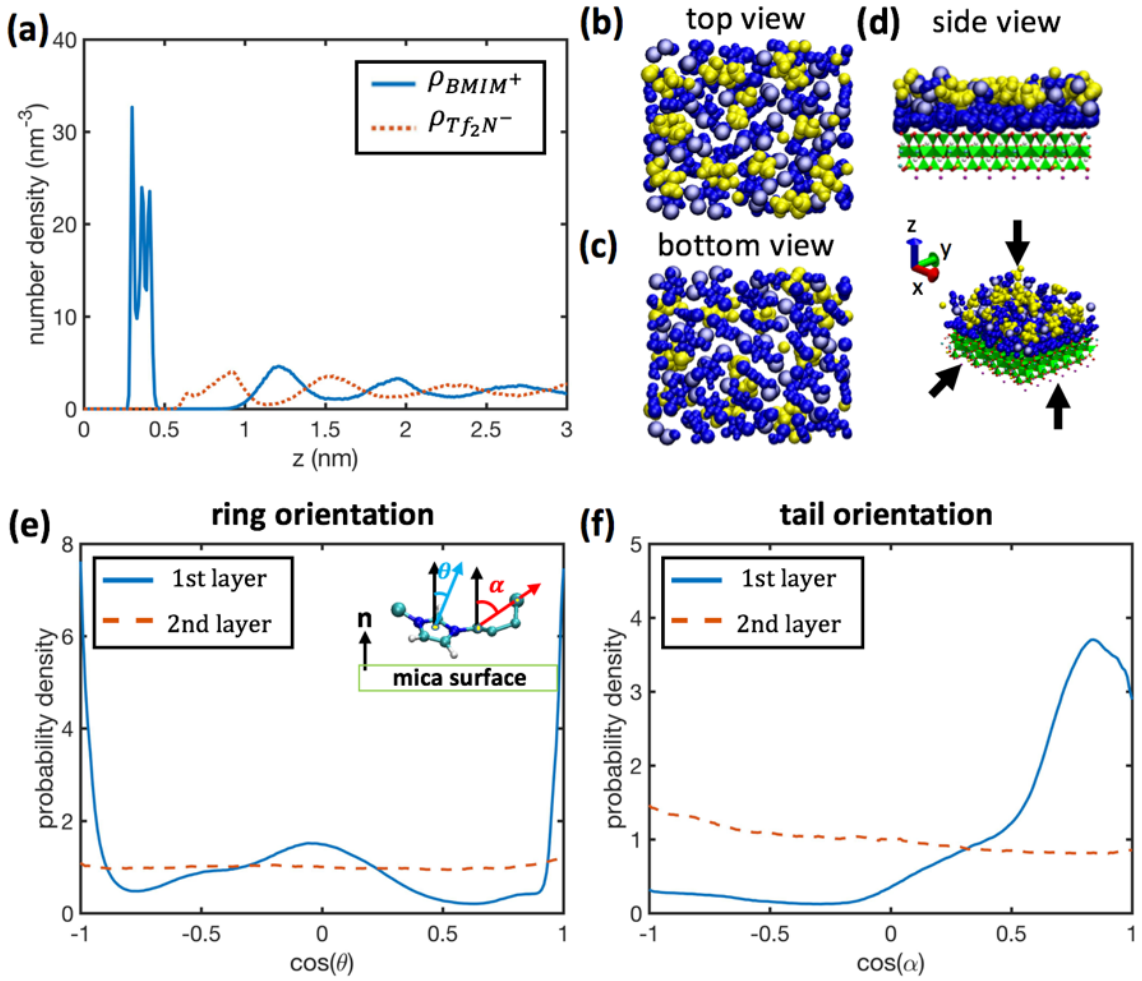

Figure 4-4. *Structure of [BMIM][Tf_2N] liquids near a dry mica surface with a charge density of -0.33C/m^2*. (a) The density profiles of the cations and anions. (b-d) The top, bottom and side views of the first layer of cations and anions near the mica surface. The color coding of different species is shown in Fig. 4-1. (e-f) The probability density distribution of the orientation of the ring (e) and tail (f) of the first and second layer of $BMIM^+$ ions near the mica surface with respect to the normal direction of the mica surface.

of $BMIM^+$ and Tf_2N^- ions are observed at larger distance, but the layering of ions is less distinct and becomes rather weak at z ~ 3.0nm. These interfacial structures are consistent with the generic picture of electrical double layers formed by RTILs near electrified surfaces.[93-94, 171, 175-178]

Beyond ion layering normal to the mica surface, we also examine the lateral and orientation ordering of the interfacial $BMIM^+$ and Tf_2N^- ions. Figure 4-4 b-d show the top, bottom, and side views of the first layer of $BMIM^+$ and Tf_2N^- ions near the mica surface. $BMIM^+$ ions are seen to displace the Tf_2N^- ions completely from the space adjacent to the mica surface (see Fig. 4-4d). While a distinct lateral ordering of $BMIM^+$ and Tf_2N^- ions is not observed (see Fig. 4-4b and Fig. 4-4c), the $BMIM^+$ ions adsorbed on the mica surface do show preferential orientation. From the distribution of the orientation of the $BMIM^+$ ions' imidazole rings shown in Fig. 4-4e, we observe that their rings prefer to lie parallel to the mica surface ($\cos\theta = \pm 1$), and to some extent, to align perpendicular to the mica surface ($\cos\theta = 0$, see Fig. 4-4e). From the distribution of the orientation of the $BMIM^+$ ions' tail shown in Fig. 4-4f, we further observe that the adsorbed $BMIM^+$ ions tend to point their tails toward the liquid phase (i.e., away from the mica surface). This preferred orientation is expected because, by staying away from the mica surface, the nearly neutral tails make more room for the charged ring and the methyl group on the ring to accumulate near the highly charged mica surface.[179-180] This observation is also consistent with the prediction by coarse-grained simulations of $[BMIM][PF_6]$ near charged mica surfaces.[121]

We next examine the interfacial structure near mica when water is introduced at the same area density as in the case of neutral mica surfaces. Figure 4-5a shows the density profiles of water and the ions. Water molecules are again confined within the interfacial

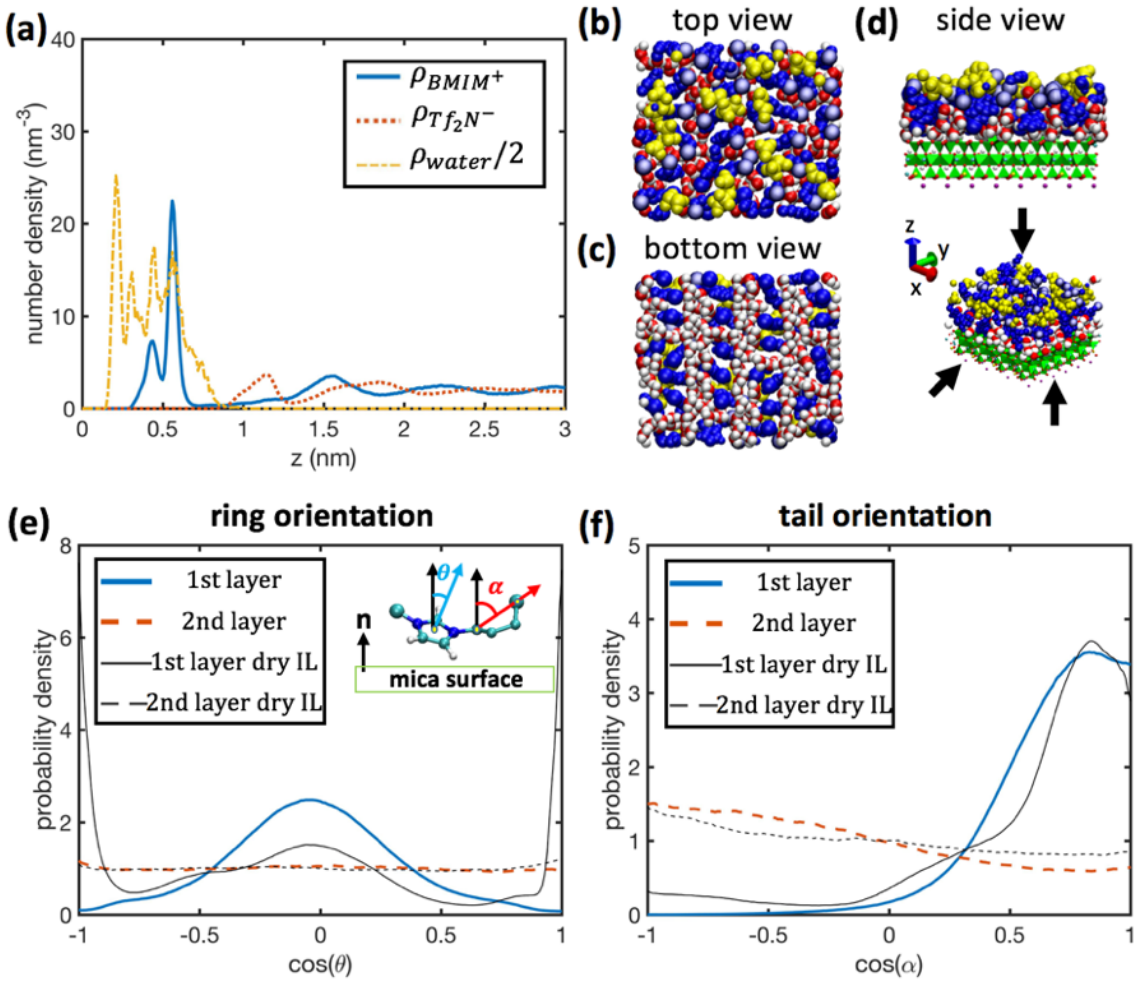

Figure 4-5. *Structure of [BMIM][Tf_2N] liquids and water near a mica surface with a charge density of -0.33C/m^2*. (a) The density profiles of the cations, anions, and water molecules. The density of water is scaled by a factor of two. (b-d) The top, bottom and side views of the first layer of cations and anions and all water molecules near the mica surface. (e-f) The probability density distribution of the orientation of the ring (e) and tail (f) of the first and second layer of $BMIM^+$ ions near the mica surface with respect to the normal direction of the mica surface. In (e-f), the orientation distributions of the ring and tail of the $BMIM^+$ ions near dry mica with the same surface charge density are shown for comparison.

zone, and they approach the mica surface closer than the $BMIM^+$ ions. The first layer of $BMIM^+$ ions near the wall, as indicated by the two closely spaced peaks in Fig. 4-5a (z=0.43 and 0.56nm), appears at a distance of ~0.5nm from the mica surface. The position of this $BMIM^+$ ion layer is similar to the position of the $EMIM^+$ layer revealed in the study of humid [EMIM][BF_4] near charged mica surfaces.[125] Compared to the dry mica case (see Fig. 4-4a), the first $BMIM^+$ layer is shifted away from the mica surface by ~0.2nm, which is similar to that observed in the coarse-grained MD simulations of dry and humid [BMIM][PF_6] confined in a 1.8nm mica gap.[121] Note that although water molecules appears closer to the mica surface than the $BMIM^+$ ions, whose position is shown using the center of its imidazole ring, the first layer of $BMIM^+$ ions mostly stand on the mica surface with the methyl group on their rings sticking on the surface and their tails up in the liquid. Indeed, as shown in the bottom and side view of the first cation, anion, and water layers near the mica surface (Fig. 4-5 c-d), no water molecules get between the first layer of $BMIM^+$ ions and the mica surface. The first $BMIM^+$ layer is followed by a Tf_2N^- layer, whose position is also shifted away from the mica surface by ~0.2nm compared to the dry mica case. Beyond the first cation and anion layers, alternating layers of $BMIM^+$ and Tf_2N^- ions penetrating to ~3nm from the mica surface are again observed, although the heights of the corresponding density peaks are lower than the dry mica case.

The above observations are in line with the results from the few simulation studies of RTIL-water-mica interfaces available now.[121, 125] Further analysis of the MD trajectories reveals additional insight on how water modifies the structure of RTILs near charged mica surfaces, in terms of ion layering, lateral and orientation ordering, and self-assembly of cations near the mica surface.

We first examine the ion accumulation in the interfacial zone in more details. We define an accumulative count of the $BMIM^+$ and Tf_2N^- ions using $\Gamma_{\pm}(z) = \int_0^z \rho_{\pm}(s)ds$ and an accumulative excess of cation using $\Gamma_{ex}(z) = \int_0^z (\rho_+(s) - \rho_-(s))ds$. Γ_{ex} indicates how the charge of a mica surface is screened as we move away from the mica surface: the charge is fully screened when Γ_{ex} reaches σ/e and over-screened when Γ_{ex} exceeds σ/e (σ is mica's surface charge density; e is the electron charge). Figure 4-6 a-b compares $\Gamma_{\pm}(z)$ near mica surface with and without water. It shows that, in presence of water, the adsorption of $BMIM^+$ on the mica surface is reduced by ~12% and the number of anions in the first Tf_2N^- ion layer is reduced by ~27%. As a result, the overscreening of the mica's surface charge by the interfacial ions weakens (see Fig. 4-6c).

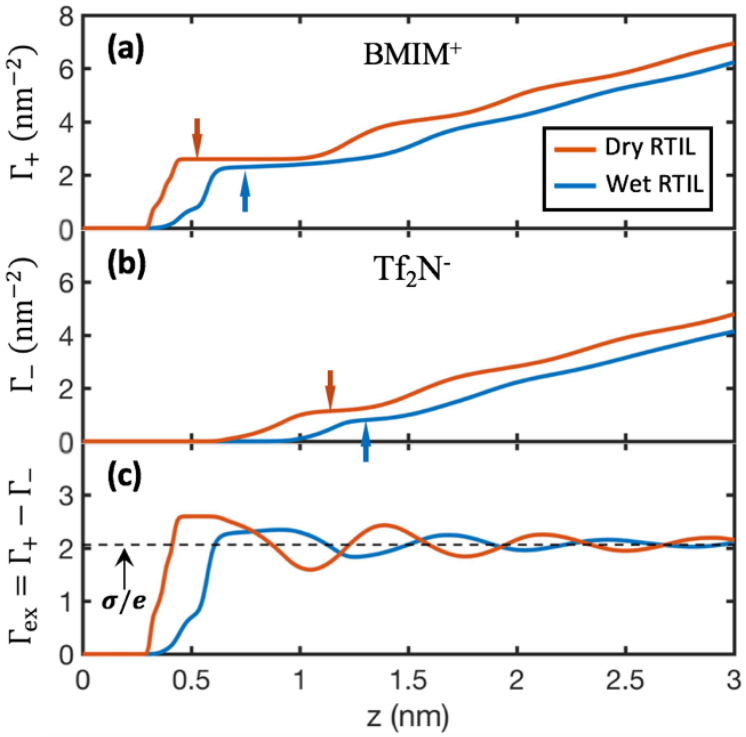

Figure 4-6. *The accumulation of ions near mica surface with a charge density of -0.33C/m² in presence and in absence of water*. (a-b) The accumulative count of the $BMIM^+$ ions (a) and Tf_2N^- ions (b) as a function of the distance from the mica surface ($\Gamma_{\pm}(z) = \int_0^z \rho_{\pm}(s)ds$). (c) The accumulative excess of cations as a function of the distance from the mica surface

($\Gamma_{ex}(z) = \int_0^z (\rho_+(s) - \rho_-(s))ds$). In all panels, the outer boundaries of the first $BMIM^+$ and Tf_2N^- layers are marked using arrows.

Along with the reduced $BMIM^+$ adsorption on the mica surface, the ordering of the adsorbed $BMIM^+$ is also modified by the interfacial water. Comparison of Fig. 4-4c and 4-5c shows that, while the $BMIM^+$ ions adsorbed on dry mica surfaces are largely disordered, those adsorbed on the "wet" mica exhibit strong ordering in the lateral plane. Inspection of the trajectories indicates that these ions are localized at spots where the surface K^+ ions were removed during the electrification of mica surfaces. Figure 4-5e shows that the $BMIM^+$ ions adsorbed on the mica surface tend to orient their rings normal to the surface, in contrast to the situation near charged, dry mica, where the rings of many of the adsorbed $BMIM^+$ ions lie parallel to the surface. Figure 4-5f shows that, as in the case of dry mica, the adsorbed $BMIM^+$ ions mostly point their tails toward the bulk liquids. However, compared to that near dry mica, the tails of the second layer of $BMIM^+$ ions near "wet" mica have slightly more preference to orient their tails toward the mica surface. This tail arrangement, along with the fact that the tails of the first layer of adsorbed $BMIM^+$ ions point toward bulk liquids, suggests that, the tails of the first two $BMIM^+$ ion layers tend to aggregate. This aggregation, a form of self-assembly often encountered in bulk RTILs,[181] is more distinct near "wet" mica surfaces than near dry mica surfaces.

As with the effect of water on the interfacial structure of RTILs near neutral mica surfaces, the effect of water on the structure of RTILs near charged mica surfaces revealed here are specific to the water area density and mica surface charge density we adopted here. However, the qualitative aspects of water's effect revealed here should persist under other water area densities. In particular, the weakening of overscreening by water is likely a universal phenomenon.

The multi-faceted effects of water on the interfacial structure of RTILs near mica surfaces are caused by the small, but finite size of water molecules and the dielectric screening by the water molecules. The interactions between a highly charged mica surface and the $BMIM^+$ ions are stronger than that between the mica surface and water molecules. However, once the number of $BMIM^+$ ions adsorbed on the mica surface can fully screen its charge, the smaller water molecule can compete effectively with the bulky $BMIM^+$ ions for the space near the strongly hydrophilic mica surface. In face of the competition for space by water molecules, the $BMIM^+$ ions must pack more effectively near the mica surface when screening its surface charge. Therefore, $BMIM^+$ ions are adsorbed preferentially on surface spots with more localized negative charge (i.e., the spot below the removed surface K^+ ions) and adsorbed $BMIM^+$ ions align their rings normal to the mica surface. Furthermore, the interfacial water molecules screen the electrostatic interactions between the $BMIM^+$ and Tf_2N^- ions, thus reducing their correlations. Since weaker cation-anion correlations generally reduce the over-screening of surface charge by RTILs,[165] the adsorption of $BMIM^+$ ions on the mica surface and the accumulation of Tf_2N^- ions near the adsorbed $BMIM^+$ ion layer reduces, as observed in Fig. 4-6a and 4-6b. Because the first Tf_2N^- ion layer near "wet" mica surfaces is less dense compared to that near dry mica surfaces, it leaves more space to accommodate the tails of the ions in the second $BMIM^+$ ion layer near the wall. Therefore, more ions in the second $BMIM^+$ ion layer point their tail toward the mica surface.

While water greatly modifies the structure of interfacial RTILs near charged mica surfaces, the interfacial ions also affect the adsorption of water at the mica-RTIL interface. The area density of interfacial water in the charged mica-water-RTIL system is the same

as that in the neutral mica-water-RTIL system. Using Equation 4-1, the relative humidity of the virtual ambient environment, with which the water molecules of our charged mica-water-RTIL system is in equilibrium, is found to be $4.9 \pm 3.9\%$ (see Appendix C), which is lower than that found in the neutral mica system ($20.5 \pm 11.3\%$). Therefore, as a mica surface immersed in RTILs develops net charge, the adsorption of water molecules near it is further enhanced.

4.3.3 A general picture of ionic liquid structure near "wet" surfaces

The above results suggest that interfacial water plays three roles in shaping the structure of RTILs near a mica surface. As a dielectric solvent, water screens the electrostatic ion-ion and ion-mica interactions and thus tends to weaken layering at a given surface charge. At the same time, the dielectric screening and hydration of surface atoms by water can prompt the electrification of mica surfaces and thus enhancing ion layering near them. As a molecular liquid, water competes with the ions for space near the strongly hydrophilic surfaces, prompts the organization of the hydrophobic tails of the ions, and enforces preferential orientation of the cations' rings, all of which can potentially enhance the ordering of the interfacial ions. The interplay of these roles, which depends on the charge of the mica surface, makes the effect of water on the interfacial ion structure rather complicated. Introducing water can either enhance or weaken the layering of interfacial ions depending on the net charge of the mica surface. Likewise, the lateral and orientation ordering of these ions can either be enhanced or weakened by the introduction of interfacial water.

With the results in the previous sections and prior studies of the interfacial structure of humid RTILs, [101-102, 105, 119-125] we can postulate a general picture of the structure of

RTILs near "wet" surfaces (see Fig. 4-7). Specifically, in presence of environmental water, the RTIL structure near a surface, whose charge is not dictated by external means (e.g., gold surfaces connected to a voltage source), is governed by *the three-way coupling* among the self-organization of ions, the interfacial water adsorption, and the electrification of the surface. The importance of each process as well as how it depends on input parameters (e.g., nature of RTILs and solid surface and the availability of water in the environment, see the blue boxes in Fig. 4-7) are reasonably established both experimentally and in simulations.[101-102, 121, 123, 125, 127] Here, we emphasize that these processes are tightly coupled and attention should be paid to their interplay in understanding how input parameters of solid-RTIL-water systems determine the interfacial structure or RTILs. For example, the adsorption of water in the interfacial zone can lead to good hydration of mica's surface K^+ ions and the self-organization of ions near a mica surface can conceivably modify the local dielectric environment experienced by the surface K^+ ions, both of which can prompt the dissociation of these surface ions and thus the electrification of the mica surface. Furthermore, the adsorption of water at solid-RTIL interfaces is strongly coupled with the ion self-organization and surface electrification. Even some level of positive feedback among the three processes may appear during the development of interfacial structures near an initially uncharged solid surface. As pointed out above, the presence of [BMIM][Tf_2N] on mica surfaces enhances the adsorption of water compared to bare mica surfaces. The adsorbed water may initiate/enhance the electrification of the mica surfaces, which in turn modifies the organization of ions near the surface and attracts even more water molecules to the interfacial zone.

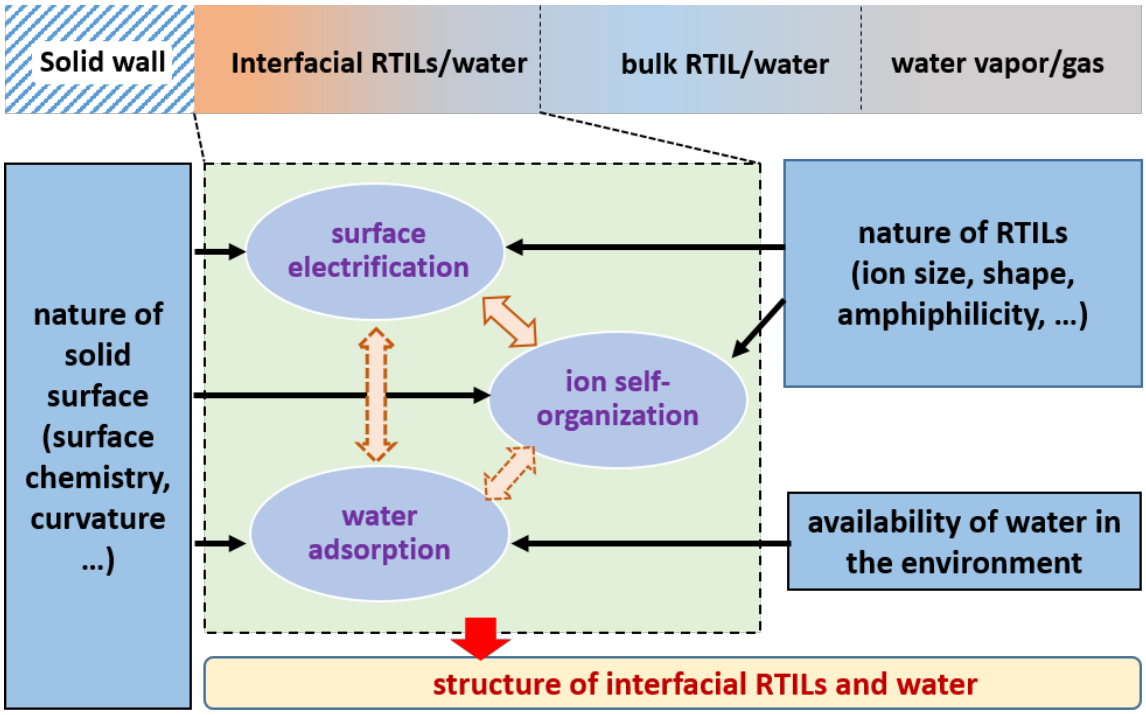

Figure 4-7. A general picture of the structure of room-temperature ionic liquids (RTILs) near solid surfaces that can be electrified by dissociation of the surface atoms. The top panel is a schematic of a solid-RTIL system exposed to the ambient environment. The bottom panel shows the envisioned picture of how the nature of the system (RTILs, solids, and environment) affects the three tightly coupled processes, whose interplay determines the structure of the interfacial RTILs and water.

4.4 Conclusions

We study the structure of [BMIM][Tf_2N] near mica surfaces with a focus on how the interfacial ion structure is affected by the presence of water and the electrification of mica surfaces. Near dry, neutral mica surfaces, $BMIM^+$ and Tf_2N^- ions are adsorbed into closely separated layers with little charge separation. The adsorbed $BMIM^+$ ions exhibit modest lateral and orientation ordering, but ions beyond the first layer shows very modest structuring. The water molecules introduced at the neutral mica-RTIL interfaces displace the ions from the mica surface and the structuring of the interfacial ions nearly diminishes. Near dry, highly charged mica surfaces, strong and alternating layering of $BMIM^+$ and

Tf_2N^- ions is distinct, but the lateral and orientation ordering of the ions is obvious mainly in the first $BMIM^+$ layer. Introducing water into the system weakens the adsorption of $BMIM^+$ ions on the mica surface and the subsequent layering of Tf_2N^- and $BMIM^+$ ions away from the mica surface. Nevertheless, the lateral and orientation ordering of the $BMIM^+$ ions contact adsorbed on the mica surface becomes stronger and modest aggregation of the hydrophobic tails of the first and second layers of $BMIM^+$ ions occurs.

Our simulations and insight from prior works on RTIL-water-mica systems suggest a general picture of how water affects the interfacial structure of RTILs, i.e., in presence of environmental water, the structure of RTILs near a surface electrifiable via surface atom dissociation is governed by *the three-way coupling* between the self-organization of interfacial ions, adsorption of water at RTIL-solid interfaces, and the electrification of the surface. Delineating how these processes and their interplay depend on choice of RTILs, nature of the solid surfaces, and the availability of water in the environment will provide a mechanistic understanding of the interfacial structure of humid RTILs near solid surfaces. Research in this direction, especially on the strong coupling of the three processes, can benefit from the integration of different techniques. For example, in this study, the dissociation of the surface K^+ ions is taken as an input because our simulations cannot handle bond breaking. Density functional theory (DFT) simulations capable of resolving the dissociation of surface K^+ ions may be combined with classical MD simulations (or classical DFT simulations) to address this limitation in the future.

Water is often treated as nuisance in the application of RTILs until most recently. However, at least for water-stable RTILs, water may be leveraged to improve the performance of devices whose function depends on the properties of interfacial RTILs. The

concept of tailoring the molecular design of RTILs to obtain desired interfacial structure is widely practiced in applications of RTILs. The idea of using interfacial water as a new handle to manipulate the interfacial structure (and thus dynamics) of RTILs can potentially complement this widely practiced concept and allow more flexibility in the application of RTILs. In this regard, encouraging results have already been reported for using interfacial water to improve capacitive energy storage and lubrication.[7-9] We hope these results will stimulate new fundamental and applied researches on this idea in the future and the general picture of the interfacial structure of RTIL suggested in this work can help guide these researches.

Supporting Information Available in Appendix C: Method for computing the relative humidity of the virtual ambient environment with which the interfacial water is in equilibrium and force field parameters.

Chapter 5: Adsorption of Molecular Nitrogen in Electrical Double Layers near Planar and Atomically Sharp Electrodes

Disclosure

This work has been published by the American Chemical Society: F. Zhang, A. J. Rondinone, J. Huang, B. G. Sumpter, and R. Qiao, "Adsorption of Molecular Nitrogen in Electrical Double Layers near Planar and Atomically Sharp Electrodes", Langmuir, 34, 48, 2018.

5.1 Introduction

The adsorption of small gas molecules such as N_2 and CO_2 near solid surfaces immersed in liquids is encountered in diverse applications including chemical separations and catalysis.[182-184] Due to the adsorption, gas molecules are enriched at the solid-liquid interfaces, which could be either beneficial or detrimental to the chemical and/or physical processes. The accumulation of gas molecules at the solid-liquid interfaces encompasses both their adsorption on the solid surface and their absorption in the interfacial zone within a few nanometers from the solid surface, where the structure of the liquids differs from that in bulk liquids. Given the molecular-size thickness of the interfacial zone,[185] it is not straightforward to differentiate the gas absorption in this zone and the gas adsorption on the solid surface. Hence, these two forms of gas accumulation are often lumped as just one term of gas adsorption at liquid-solid interfaces.[135-136, 186] It is essential to understand such

gas adsorption phenomena in order to offer insight for diverse applications where desirable gas adsorptions need to be enhanced while unwanted ones need to be suppressed.[183]

The quantification of gas adsorption at solid-liquid interfaces along with the clarification of underlying mechanisms are experimentally challenging because such interfacial phenomenon involves not only adsorbates and adsorbents but also solvent molecules, which makes the problems of gas distribution and liquid structure in the molecularly thin interfacial zone complicated.[185, 187] Molecular simulations, on the other hand, can probe the structure and energetics of gas molecules in the interfacial zone at a molecular resolution and thus serve as a powerful tool to address these challenges. Earlier molecular dynamics (MD) simulations showed that gas molecules modeled as Lennard-Jones particles are enriched near hydrophobic walls immersed in water.[186] Recent Grand Canonical Monte Carlo simulations showed similar enrichment of gas molecules dissolved in water and suggested that the enrichment does not show strong gas specificity.[135] Most recently, the Aluru group systematically examined the adsorption of dissolved gas molecules near graphene walls using MD simulations by computing the potential of mean force (PMF) of these molecules near the wall.[136] Their analysis revealed that, in addition to the gas-wall interactions, the solvent effects play a crucial role in gas adsorption. While the gas adsorption is enhanced by the solvent-induced entropic effects, it is also hindered by the solvent-induced enthalpic effects.

Our interest in the adsorption of gas molecules at solid-liquid interfaces mainly comes from a recent report of electrochemical synthesis of NH_3 from N_2.[134] Song *et al.* showed that N_2 gas dissolved in aqueous electrolytes can be electrochemically reduced on the surface of N-doped carbon electrode materials that exist in the form of carbon nanospikes

with tip sizes as small as ~1 nm. As a result, NH_3 can be synthesized electrochemically with a Faradaic efficiency of 11.5% and a production rate of 97.2 $\mu g\, hr^{-1}\, cm^{-2}$ under ambient conditions.[134] It was found that the reaction is driven by the sharp tips of the carbon nanospikes, since MD simulations in combination with *ab initio* calculations showed that the electrical field near the nanospikes is strongly enhanced to promote the reactivity of the otherwise inert N_2 molecules.[134] This was also corroborated by experiments that etched the sharp carbon nanospikes away, resulting in a dramatic decrease in N_2 electrochemical reduction process. Regardless of the chemical details of the electrochemical reduction of N_2, the adsorption of N_2 at the interface of the carbon nanospikes and electrolyte solutions is an essential step of the electrochemical reactions. Understanding this phenomenon would thus help us further clarify the process of electrochemical N_2 reduction on the carbon nanospikes.

Prior works on the gas adsorption at solid-liquid interfaces can lend some help toward the understanding of the adsorption of N_2 on/near carbon nanospikes. For instance, based on the prior simulations of dissolved N_2 and other similar gas molecules,[135-136] it is expected that N_2 molecules are locally enriched near the carbon nanospikes compared to their distribution in bulk electrolytes. However, the adsorption of N_2 on the carbon nanospikes in the experiments by Song *et al.* exhibits several features not explored in the previous studies of gas adsorption at solid-liquid interfaces, and therefore some important questions remain open. First, during the electrochemical reduction of N_2, the carbon nanospikes are electrified and thus electrical double layers (EDLs) are established at the electrode-electrolyte interfaces. Within the EDLs, the structure of solvent water, which can affect the gas adsorption based on prior research,[137] can deviate strongly from those near neutral solid

surfaces and in bulk electrolytes. However, to our best knowledge, the adsorption of gas molecules near electrified electrodes, or equivalently in EDLs at the electrode-electrolyte interfaces, has not been studied. Second, the carbon nanospikes have tip sizes as small as ~1 nm. How gas adsorption is affected by the large curvature of these surfaces is not clear because most previous studies focused on gas adsorption near planar walls. The advent of electrochemical catalysts with nanotextures has thus opened up new opportunities for applications along with challenges for understandings.

In this work, we investigate the N_2 adsorption in the EDLs formed at the interfaces of solid electrodes and aqueous electrolytes using MD simulations. The effects of electrification of carbon electrodes and their different surface curvatures are examined in detail to address the above raised questions. N_2 enrichment is found near neutral electrodes regardless of the surface curvature. In comparison, N_2 enrichment is further enhanced when the electrode is moderately charged, but is reduced when the electrode is highly charged, especially in the EDLs near a planar electrode. When the electrodes are highly charged, the amount of N_2 molecules available for electrochemical reduction is an order of magnitude higher near spherical electrodes than near planar electrodes. We further studied the potential of mean force for dissolved N_2 and investigated the interfacial water structure along with the hydration shell of N_2 to rationalize the observed gas adsorption behavior.

The rest of this manuscript is organized as follows. Section 5.2 describes the simulation system and method. Section 5.3 presents the N_2 adsorption in EDLs and how it is affected by the charge density and surface curvature of the electrodes. Finally, conclusions are drawn in Section 5.4.

5.2 Simulation Systems, Models, and Methods

System. Two types of systems featuring planar and spherical electrodes were studied. In the first type of system (Figure 5-1a), a slab of aqueous LiCl electrolyte was placed on a graphene bi-layer, where the surface charge density of the top layer in contact with the electrolyte was set to σ =0, -0.08, and -0.16 C/m^2 by assigning small partial charges evenly on the carbon atoms. The dimension of the system box was 4.426×4.486 nm^2 in the direction parallel to the electrode surface and 18 nm in the direction normal to the electrode surface. The electrolyte contained 3700 water molecules, resulting in a ~6 nm-thick liquid layer over the electrode's top surface. In the case of a neutral electrode, 40 pairs of Li^+ and Cl^- ions were dissolved in the water layer giving a concentration of ~0.5 M. When the electrode carried a surface charge density of -0.08 or -0.16 C/m^2, 10 or 20 additional Li^+ ions were added into the water layer to neutralize the charges on the electrode.

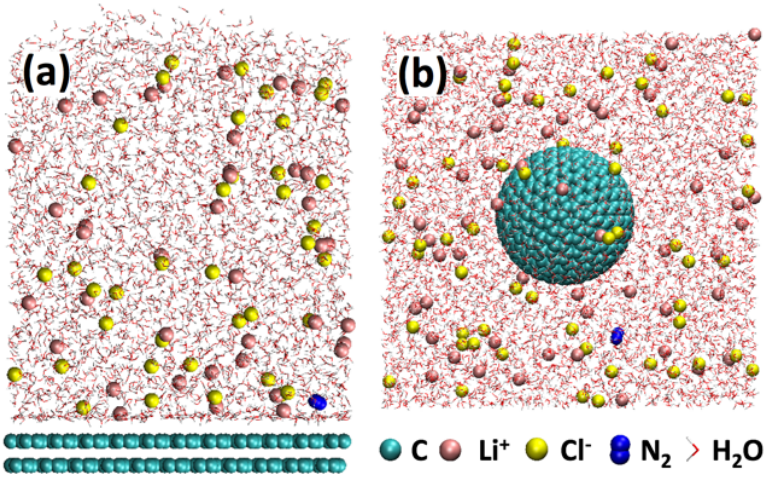

Figure 5-1. Snapshots of the MD systems for studying the adsorption of N_2 in the electrical double layers (EDLs) near planar (**a**) and spherical (**b**) electrodes.

In the second type of system (Figure 5-1b), a spherical electrode consisting of two atom layers was used to represent the strong surface curvature at the sharp tip of carbon nanospikes. The radius of the outer atom layer for the spherical electrode was set to 1 nm.

The electrode was fixed in the middle of the MD box measuring 5.858×5.858×5.858 nm^3 and surrounded by the same electrolyte as in the first type of system. Different surface charge densities were also explored to investigate their effect on the N_2 adsorption in EDLs near electrodes with a strong surface curvature. The spherical electrode was surrounded by 6400 water molecules. For neutral electrode, 58 pairs of Li^+ and Cl^- ions were dissolved in the water solvent giving a concentration of ~0.5 M. An additional 6 or 12 Li^+ ions were added to neutralize the electrode's charge when the electrode carried a surface charge density of -0.08 or -0.16 C/m^2, respectively. For both types of systems, the Debye length of the electrolyte is ~0.4 nm under the studied ion concentration, regardless of the surface charge densities, which produces a nanometer-thick EDL near the electrode surfaces.

Due to the low solubility of N_2 molecules in water, it is challenging to simulate N_2 adsorption in EDLs directly using MD simulations. Instead, we simulated a single N_2 molecule in EDLs. By constraining one N_2 molecule at various distances from the electrode surface in a series of simulations, we studied the N_2 adsorption using the Umbrella sampling method.[188-189] From the distribution of the N_2 molecule obtained in these simulations, we constructed the PMF (ϕ) of a single N_2 molecule as a function of its distance x from the electrode surface using the Weighted Histogram Analysis Method (WHAM) technique.[190] By setting the PMF of N_2 in the bulk electrolyte as a reference, i.e., $\phi_\infty = 0$, the density distribution of N_2 in an EDL in equilibrium with an electrolyte that has a bulk N_2 density of ρ_∞ was then calculated using Boltzmann distribution as[191]

$$\rho(x) = \rho_\infty exp\left(-\frac{\phi(x)}{k_B T}\right) \quad (5\text{-}1)$$

In this work, ρ_∞ was taken as 3.55×10^{-4} nm^{-3}, which is the saturation density of N_2 molecules in water exposed to a pure N_2 gas reservoir under a pressure of 1 atmosphere

(101.325 kPa) at 300 K. In the present method of computing the N_2 density in EDLs in equilibrium with a N_2 gas reservoir, because the PMF was obtained from simulations based on only a single N_2 molecule, it is implicitly assumed that the concentration of N_2 molecules in the EDLs is so low that they do not affect the adsorption of one another. Under the conditions studied here, where ρ_∞ is low and the enrichment of N_2 in the EDLs is modest, the lateral distance between the N_2 molecules adsorbed in the real EDLs in equilibrium with a N_2 gas reservoir would be in the range of 43-167 nm (see Appendix D). Therefore, the above assumption is valid.

Models. Water molecules and N_2 molecules were modeled using the SPC/E model and TraPPE force fields, respectively.[141, 192] With the TraPPE force fields, the N_2 molecule has a dipole moment of zero and a quadrupole moment of -4.67×10^{-40} C·m^2. The Li^+ and Cl^- ions were modeled as charged Lennard-Jones (LJ) spheres.[193] The planar electrodes consisted of two A-B stacked graphene layers separated by 0.33 nm. The spherical electrodes consisted of two layers of carbon atoms separated by 0.33 nm in the radial direction. The carbon atoms in each layer were arranged in a lattice consisting of pentagonal and hexagonal rings, and the distance between neighboring carbon atoms on the outer surface of the carbon nanosphere was 0.14 nm, similar to that in graphene. The LJ parameters for carbon atoms were the same as those used in prior study of H_2 and CO_2 adsorption on graphenes.[7] The Lorentz-Berthelot combination rule was used to obtain the LJ parameters between different types of atoms.

Simulation protocol and method. To build the simulation systems, water molecules and electrolyte ions were placed in the MD box using the Packmol code.[145] One N_2 molecule was then introduced into the systems and located at different distances from the

electrode surface. All simulations were performed using the Gromacs code[143] in the NVT ensemble (T = 300 K). A cutoff radius of 1.3 nm was used for computing the non-electrostatic interactions. To compute the electrostatic interactions, the Particle Mesh Ewald (PME)[194] method was used with an FFT grid spacing of 0.11 nm and a real space cutoff of 1.3 nm. The electrode atoms were fixed in all simulations. The geometry of the water molecules was maintained using the LINCS algorithm.[162] The implementations of the Umbrella sampling and WHAM methods in Gromacs were used to compute the PMFs of the single N_2 molecule at a distance of z = ~0.25 to 1.50 nm from the electrode surface.[143] In the series of Umbrella sampling simulations performed, the spacing between the consecutively constrained N_2 molecules was 0.075 nm. To account for the entropic decrease of the PMF due to the increase of the number of configurations with the radial distance s from the center of the spherical electrodes, the PMF of the N_2 molecules computed using Gromacs was corrected by $k_{\mathrm{B}}T\ln(4\pi s^2)$.[195-196] In each constrained simulation, an equilibrium run of 5 ns was performed first, followed by a production run of 15 ns to gather statistics.

5.3 Results and Discussion

5.3.1 Macroscopic N_2 adsorption behavior in EDLs

To quantify the adsorption of N_2 molecules in the EDLs macroscopically, we define the surface excess of the adsorbed N_2 molecules Γ_{ex} near planar and spherical electrodes by the following two equations, respectively

$$\Gamma_{ex} = \begin{cases} \int_0^{\infty} (\rho(x) - \rho_{\infty}) \mathrm{d}x & (5-2\mathrm{a}) \\ \int_0^{\infty} (\rho(x) - \rho_{\infty})(r(x)^2 \,/\, R^2\,) \mathrm{d}x & (5-2\mathrm{b}) \end{cases}$$

where $\rho(x)$ is the density of N_2 molecules at a distance of x from the electrode surface computed using Equation (5-1), $r(x) = R + x$, and R =1 nm is the radius of the spherical electrode's outer surface. By calculating Γ_{ex}, we can determine to what extent the N_2 molecules in the EDLs are enriched or depleted near the electrode surface compared to that in the bulk electrolyte.

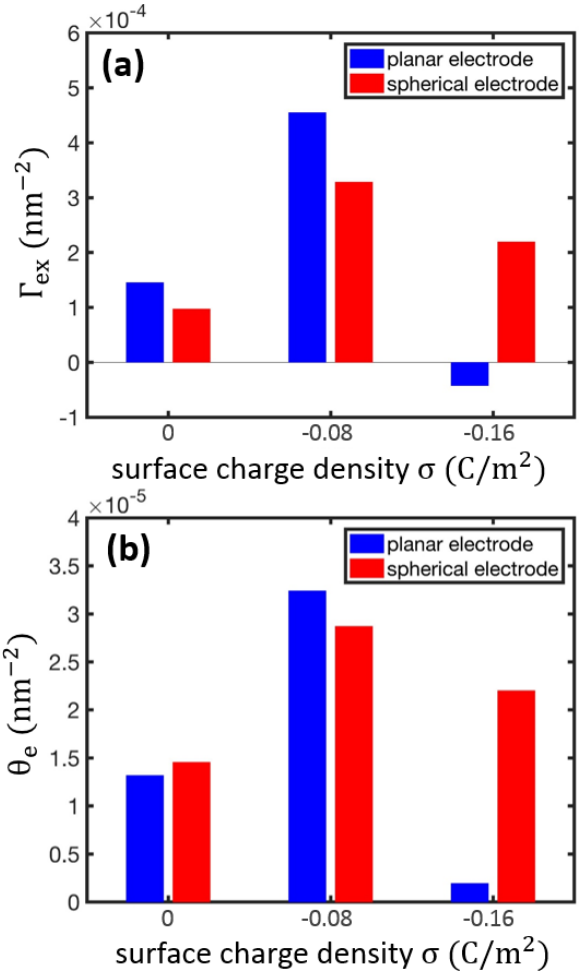

Figure 5-2. *Adsorption of N_2 molecules in the EDLs near planar and spherical electrodes.* (**a**) The variation of the surface excess of adsorbed N_2 molecules with the electrode surface charge density. (**b**) The variation of the electrochemically available N_2 molecules with the electrode surface charge density.

The excess adsorptions of N_2 in EDLs near different electrodes calculated by Equation (5-2) are shown in Figure 5-2a. For both planar and spherical electrodes with zero charge, N_2 molecules are slightly enriched near the electrode surface. In comparison, the adsorption is significantly increased for both electrodes when the electrode surface charge density changes from 0 to -0.08 C/m^2. When the electrodes become highly charged (σ = -0.16 C/m^2), N_2 adsorption in the EDLs is weakened for both electrodes compared to that at the medium charge density. However, compared to the bulk electrolyte, N_2 molecules are still moderately enriched near the spherical electrodes, although they are depleted near the planar electrodes.

The surface excess of N_2 computed above only provides information on the overall enrichment of N_2 molecules in the electrolytes without revealing the effect of their distance from the electrode surface. Whether the electrochemical reduction of a N_2 molecule can occur, however, also depends greatly on its distance from the electrode surface. For example, considering the electron tunneling effect, the probability (P) that a molecule can be reduced electrochemically decreases exponentially as its distance x from the electrode surface increases, i.e., $P(x) \sim e^{-\beta x}$, where β is the electron decay factor that depends on the nature of solvents and is 15.9 nm^{-1} in aqueous electrolytes.[197] Despite the likely complicated mechanisms of N_2 reduction on the sharp tips of the nanospikes in Ref. [134], the reduction of the N_2 molecules adsorbed near the carbon nanospikes should still follow the exponential law shown above once free electrons become available in the EDL. Based on this exponential law, we quantify the electrochemically available N_2 molecules θ_e per unit area of planar and spherical electrodes by the following two equations, respectively

$$\theta_e = \begin{cases} \int_0^\infty e^{-\beta x}\rho(x)\mathrm{d}x & (5-3a) \\ \int_0^\infty e^{-\beta x}\rho(x)(1+x/\mathrm{R})^2\mathrm{d}x & (5-3\mathrm{b}) \end{cases}$$

Figure 5-2b shows the results of θ_e for both planar and spherical electrodes calculated using Equation (5-3). At both the neutral and modest surface charge densities ($\sigma = 0$ and -0.08 C/m^2), the density of electrochemically available N_2 molecules near the planar electrode is comparable to that near a 1.0 nm-radius spherical electrode. However, when electrodes are highly charged ($\sigma = -0.16$ C/m^2), the electrochemically available N_2 molecules near the 1.0 nm-radius spherical electrodes are one order of magnitude higher than those near planar electrodes with the same surface area. The enhanced availability near spherical electrodes originates from the fact that the N_2 adsorption near highly charged spherical electrodes is stronger than that near planar electrodes with the same surface charge density. This suggests that, when operating under high voltages, the electrodes with large surface curvature are able to promote the electrochemical reduction of the N_2 molecules more effectively.

To understand the molecular mechanisms underlying the N_2 adsorption behavior revealed in Figure 5-2, we next examine the PMFs of N_2 molecules in the EDLs of the two electrodes of different charge densities and surface curvatures, and their physical origins.

5.3.2 Molecular details of N_2 adsorption near planar electrodes

Neutral electrodes. The macroscopic adsorption characteristics of N_2 molecules in an EDL depend on the distribution of their density, or equivalently, the PMF across the EDL (see Equation 5-1). Figure 5-3a shows the PMF of a N_2 molecule near a neutral, planar electrode. As the molecule moves away from the electrode surface, a deep valley of -5.33

kJ/mol, which favors the local accumulation of N_2 molecules, is first observed at z = 0.34 nm. It is immediately followed by a high peak of 4.58 kJ/mol at z = 0.54 nm, where N_2 molecules tend to be depleted. Beyond the first valley and peak, the PMF oscillates but the subsequent valleys' depth and peaks' height become less distinct with increasing distances. At $z \gtrsim 1.2$ nm, the PMF is essentially zero, indicating that the effect of the planar electrode on the adsorption of N_2 molecules is limited to within a distance of ~1.2 nm from its surface.

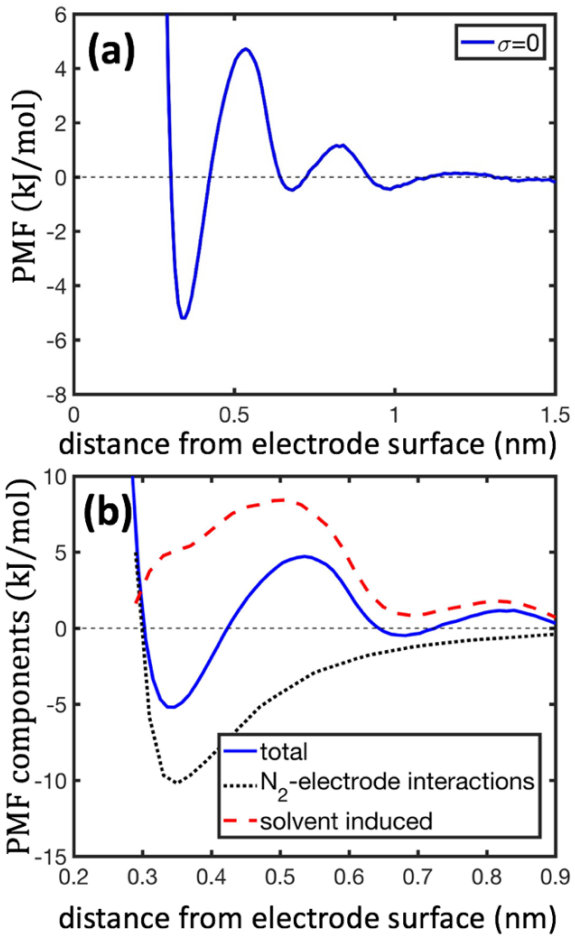

Figure 5-3. The potential of mean force (PMF) of a N_2 molecule near a neutral planar electrode (**a**) and its contribution from the N_2-electrode interactions and the solvent effects (**b**).

To understand the total PMF shown in Figure 5-3a, we decomposed it into two components following the approach adopted in a prior work,[136] i.e., a N_2-electrode interaction component and a solvent-induced component. The former component was determined by computing the non-electrostatic potential between a N_2 molecule and the neutral electrode at various N_2-electrode distances found in our simulation trajectories. This component was subtracted from the total PMF to obtain the solvent-induced component of the PMF. These two components of the PMF are shown in Figure 5-3b. We observed that when $z \gtrsim 0.3$ nm, the N_2-electrode interaction component is always negative while the solvent-induced component is always positive. These observations agree with those reported by Lee and Aluru in their study of H_2 and CO_2 near neutral graphenes.[136] Along with the fact that the valley of the potential due to N_2-electrode interactions ($z = 0.35$ nm) nearly coincides with the first valley of total PMF ($z = 0.34$ nm), these results suggest that the non-electrostatic N_2-electrode attractions contribute to the enrichment of the N_2 molecules near neutral electrodes. However, in the region $z < 0.5$ nm, the solvent-induced PMF also decreases as the molecule moves toward the electrode. This suggests that the solvent-induced effects also partly contribute to the formation of the first PMF valley. In fact, the solvent-induced effects are the main reason for the oscillation of the total PMF at $z > 0.5$ nm because the potential of N_2-electrode interactions only displays a monotonic decrease in magnitude as the molecule moves away from the electrode. Consequently, understanding the solvent-induced effects on the PMF of an interfacial N_2 molecule is essential for understanding the total PMF (and thus the adsorption) of N_2 molecules in the interfacial zone.

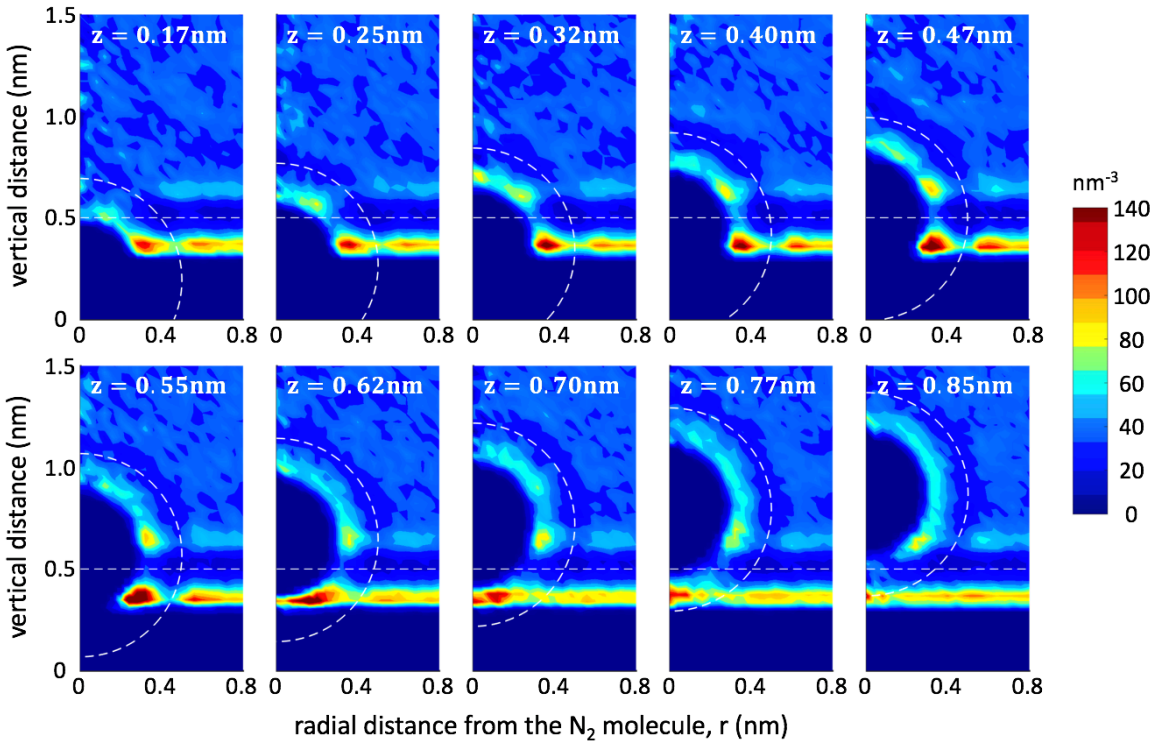

Figure 5-4. The density distribution of water molecules around individual N_2 molecules located at a distance of 0.17-0.85 nm from a neutral planar electrode. *z* is the vertical direction and it points from the electrode's top surface (*z*=0) toward the electrolyte. *r* is the radial direction in the horizontal plane and it emanates from the central N_2 molecule. The upper boundary of the first layer of water molecules on the electrode is marked with a horizontal dashed line. The outer boundary of the first hydration layer of the N_2 molecule is marked using a dashed circle. The positions of the N_2 and water molecules are based on their center-of-mass.

To understand the solvent-induced effects and their contribution to the N_2 molecule's PMF near the electrode, we examine how the N_2 molecule located at different distances away from the electrode is hydrated by water molecules. Figure 5-4 shows the distribution of water molecules as a function of their vertical distance from the electrode surface (*z*) and their radial distance from the interfacial N_2 molecule in the horizontal plane (*r*). The water distribution can be examined from two different perspectives. From the perspective of the electrode, we observe that a distinct water layer centering on $z = 0.34$ nm is formed, with its upper boundary marked by a white dashed line in Figure 5-4 (another, albeit less well-defined, water layer can also be identified at $z = 0.61$ nm). Such a layering of water

molecules is a well-known signature of the solid-liquid interfaces,[198] and can be also clearly seen from the average density profile of water molecules near the electrode (see Figure D-1 in the Appendix D). From the perspective of the interfacial N_2 molecule, a shell of hydration water can be also clearly discerned, with its outer boundary marked by a white dashed circle in Figure 5-4.

Figure 5-4 also shows that, when a N_2 molecule moves away from z = 0 to ~0.5 nm, the evolution of the water structure around it is characterized by a decrease of the electrode-water interfacial area along with an increase of the N_2-water interfacial area. Because, water molecules interact much more weakly with a N_2 molecule than with the electrode (as is evident from the more distinct layering of water near the electrode, see Figure 5-4), this evolution of the N_2-water and electrode-water interfacial areas comes with a free energy penalty and leads to an increase of the solvent-effect component of the PMF shown in Figure 5-2b. Such an energy penalty, together with the increase of the N_2-electrode interaction potential (or decrease of its magnitude) as a N_2 molecule moves away from the electrode, helps explain the increases of the total PMF as z increases from 0.35 to ~0.5 nm.

The situation changes when the N_2 molecule moves further away from the electrode surface. As shown in Figure 5-4, when z is in the range ~0.5 to 0.7 nm, water molecules gradually appear beneath it, thus both the N_2-water and electrode-water interfacial areas increase. However, given the strong interactions between the water molecules and the electrode, the increase of electrode-water area is favorable, while the increase of N_2-water interfacial area is much less favorable. The water molecules at the newly appeared N_2-water interfaces, which are sandwiched between the N_2 molecule and the electrode surface, may interact strongly with the electrode. As such, the evolution of the N_2-water and

electrode-water interfaces as the N_2 molecule moves away is overall a favorable process accompanied by the decrease of the solvent-effect component of the PMF. In the same region, the PMF component due to the N_2-electrode interactions increases but the total PMF gradually decreases. These facts together indicate that the solvent effects dominate over the N_2-electrode interactions, thus causing the PMF of the N_2 molecules to decrease as it moves from z = ~0.5 to 0.7 nm.

Figure 5-4 also shows that as the N_2 molecule moves further from the second valley of PMF (z = 0.68 nm) toward the bulk electrolyte, the N_2-water and electrode-water interfacial areas no longer change, but the PMF of the N_2 molecule still oscillates weakly. This oscillation of the PMF can be understood qualitatively as a result of the interference between the water structure near an individual interfacial N_2 molecule and that near the electrode surface. We note that the similar "interference" concept has been used to rationalize the oscillatory capacitance of nanopores and the oscillatory inter-surface interactions mediated by liquids.[199-200]

In bulk electrolytes, water molecules form a shell around each N_2 molecule and a density peak is observed at a distance of 0.36 nm from the N_2 molecule (see the radial distribution function of water molecule with respect to the N_2 molecule in Figure D-2 of the Appendix D). Near an electrode, as the distance from the electrode surface increases, water also forms increasingly blurred layers with density enhanced at the center of each layer and suppressed at positions between adjacent layers. When a N_2 molecule is positioned near the electrode surface, the water structure around it and near the electrode surface can interfere in two qualitatively different ways: in the positive (negative) interference, the density peak of the water shell near the N_2 molecule overlaps with one of

the density peaks (valleys) of water near the electrode. For example, when a N_2 molecule is positioned at z = 0.70 nm, the density peak corresponding to its first hydration shell is located on the spherical surface 0.36 nm from the N_2 molecule and interferes positively with the first water density peak. As a result, the packing of water near both the N_2 molecule and the electrode surface is optimized, and an enhanced water density is found beneath the N_2 molecule. Therefore, the accumulation of N_2 molecules at this position is favored, which helps explain the fact that the solvent-effect part of N_2's PMF is locally minimized at z = ~ 0.68 nm (see Figure 5-3b). However, when a N_2 molecule is positioned at z = 0.86 nm, a negative interference between its hydration shell with the first water valley near the electrode drives the depletion of water molecules at the south pole of the N_2 molecule, resulting in an unfavorable packing of water locally. Therefore, the N_2 molecule tends to be driven away from this location, which is in line with the observation that the solvent-effect component of the N_2's PMF is maximized at z = ~0.83 nm.

Due to the reasons given above, as the N_2 molecule moves further away from the electrode, positive (negative) interferences between its hydration shell and the second water peak (valley) near the electrode are observed. Consequently, the solvent-effect component of the N_2's PMF shows further oscillation. However, because the second water density peak/valley near the electrode is much less distinct compared to the first water density peak/valley (see Figure D-1 in Appendix D), the oscillation of the solvent-effect component of the PMF (and thus the total PMF) is weak.

Charged electrodes. When the electrode is electrified moderately to a surface charge density of -0.08 C/m^2, the first PMF valley is deepened by 2.30 kJ/mol while the first PMF peak is lowered by 2.04 kJ/mol compared to the PMF of a N_2 molecule near the neutral

electrode (see Figure 5-5a). Beyond the first peak and valley (i.e., $z \gtrsim 0.7$ nm), the PMF deviates weakly from that near the neutral electrode. As the surface charge density increases to -0.16 C/m^2, the change of N_2 molecule's PMF is again mainly limited to within

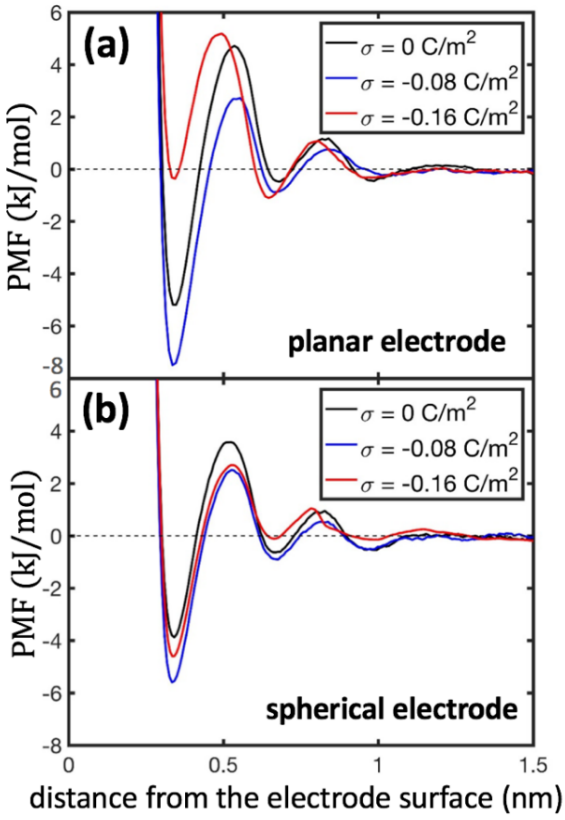

Figure 5-5. Comparison of the PMFs of a N_2 molecule near planar electrodes (**a**) and spherical electrodes (**b**) with different surface charge densities.

z = 0.7 nm from the electrode surface (see Figure 5-5a). However, the first valley rises to nearly zero while the first peak rises weakly by 0.43 kJ/mol. These changes indicate that the enhanced adsorption of N_2 molecules in EDLs with σ = -0.08 C/m^2 and the diminished adsorption of N_2 molecules in EDLs with σ = -0.16 C/m^2 observed in Figure 5-2a are caused mainly by the change of the first valley's depth of N_2 molecule's PMF as the electrode becomes electrified to different degrees. The non-monotonic evolution of the N_2's first PMF valley with increasingly more negative surface charge density is interesting and therefore is further examined below.

Because the N_2 molecule has no dipole moment and the electrical field generated by planar electrodes is uniform, the N_2-electrode interactions and their contribution to the N_2's PMF do not change as the electrode becomes electrified. Thus the non-monotonic variation of the first PMF valley observed in Figure 5-5a should originate from the solvent effects. Hence, we examine the distribution of water molecules near the electrode surface.

Figures 5-6 a-c compares the density profiles of water molecules near electrodes with different surface charge densities. As σ changes from 0 to -0.08 C/m^2 (see Figure 5-6a,b), the height of the first water density peak near the electrode (hereinafter referred to as the contact density) becomes lower while the first water density valley becomes less deep. Meanwhile, an integration of the water density from the electrode surface to the boundary of the first water layer (z = 0.5 nm) shows that the number of water molecules in the first water layer per unit electrode surface area changes from 10.32 to 10.43 nm^{-2}. Together, these results show that, as σ changes from 0 to -0.08 C/m^2, while the number of molecules in the first water layer remains nearly unchanged, the contact density of water decreases (i.e., water molecules are packed less compactly on the electrode). Because a N_2 molecule at the first valley of its PMF (z = 0.34 nm) must first displace the water molecules on the electrode surface to become contact adsorbed, the lower contact water density and less compact packing of water molecules at σ = -0.08 C/m^2 facilitates the adsorption of N_2 molecules at this place and hence the PMF valley is deeper than that when the electrode is neutral. The less compact packing of interfacial water near the moderately charged electrode can be understood as follows. It is very well established that, near a planar surface whose atoms cannot form hydrogen bonds with the water molecules, the interfacial water

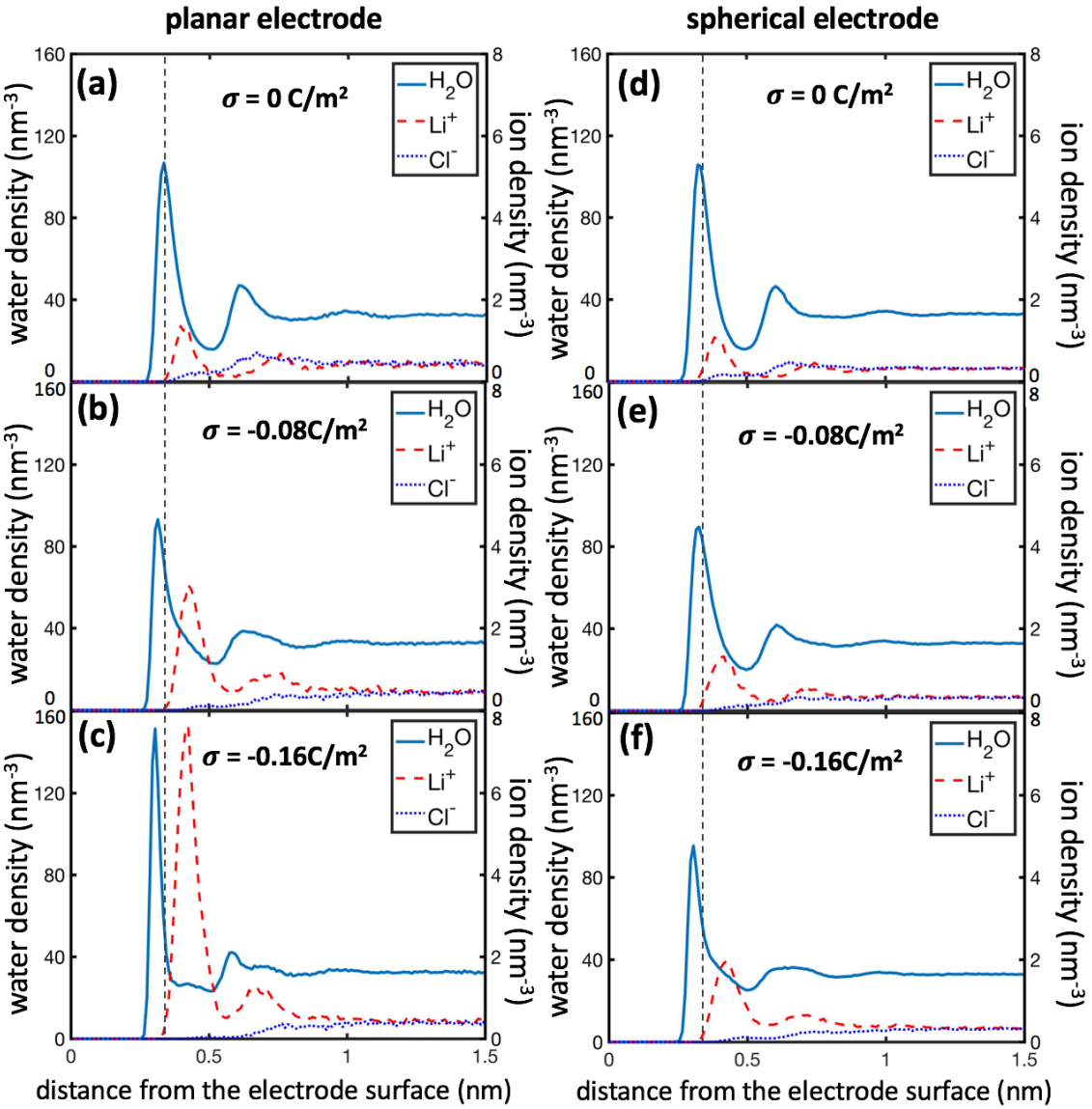

Figure 5-6. Water and ion density profiles near planar electrodes (left panel) with a surface charge density of 0 C/m^2 (**a**), -0.08 C/m^2 (**b**), and -0.16 C/m^2 (**c**); and water and ion density profiles near spherical electrodes (right panel) with a surface charge density of 0 C/m^2 (**d**), -0.08 C/m^2 (**e**), and -0.16 C/m^2 (**f**). The vertical dashed lines denote the location of the first PMF valley of the N_2 molecules (see Figure 5-5).

molecules orient with their O-H bonds parallel to the surface to maximize the hydrogen bonding among themselves.[201-202] Therefore, the interfacial water molecules exhibit strong ordering and are compactly packed. When the surface becomes negatively charged, as shown in Ref. [203], the OH bonds of many water molecules are forced by the electrical field to point toward the electrode. This disrupts some of the hydrogen bonds between the water molecules within the first density peak. As a result, the packing of the water molecules in the first density peak is less compact and more diffusive in the direction normal to the electrode surface. Consequently, the contact water density becomes smaller.

As the surface charge density of the electrode changes further to -0.16 C/m^2, the first water density peak becomes much sharper and the contact water density is ~40% higher than that near the neutral electrode (see Figure 5-6a,c). The first water density valley becomes wider and its height is ~50% higher than that the neutral electrode. These data suggest that the first interfacial water layer consists of an inner sub-layer in which water molecules are highly ordered and tightly adsorbed on the electrode surface and a more loosely packed outer sub-layer. Because inserting a N_2 molecule at the first PMF valley (z = 0.34 nm) must displace the water molecules in the highly ordered inner sub-layer from the electrode surface, such insertion is more difficult compared to that near neutral electrodes, which explains why the first PMF valley is higher than that near the neutral electrodes. The higher contact density of water and the formation of the much thinner and denser inner water sub-layer on the electrode surface can be attributed to two factors. First, the number of water molecules in the first peak increases because many water molecules are brought toward the electrode with σ = -0.16 C/m^2 by the locally increased number of Li^+ ions (see Fig. 5-6b and 5-6c). Second, while the electrical field emanating from the

electrode disrupts the hydrogen bonding between these water molecules, such a field, being much stronger than that near electrodes with σ = -0.08 C/m^2, forces the water molecules in contact with the electrode to become highly ordered in orientation, and thus making their packing more ordered and dense. Consequently, the contact water density is much higher than that near electrodes with σ = 0 and -0.08 C/m^2, and the adsorption of N_2 on the electrodes decreases.

5.3.3 Molecular details of N_2 adsorption near spherical electrodes

Figure 5-5b compares the PMF of N_2 molecules near spherical electrodes with different surface charge densities. Similar to those near planar electrodes, these PMFs oscillate as the N_2 molecule moves away from the electrode and approach zero at ~1.2 nm from the electrode surface. The depth of the first PMF valley, which dominates the net adsorption of N_2 molecules in the EDLs, also varies with the surface charge density in a way similar to that near planar electrodes. It becomes more negative as σ changes from 0 to -0.08 C/m^2 but then become more positive as σ changes from -0.08 to -0.16 C/m^2. However, the increase of the first valley's depth as σ changes from -0.08 to -0.16 C/m^2 is much weaker than that near the planar electrodes, which explains the rather modest reduction of N_2 adsorption in EDLs near spherical electrodes in this surface charge window. Because the evolution of the N_2's PMF near spherical electrodes as the electrode charge density changes from 0 to -0.08 C/m^2 is similar to that near the planar electrodes, below we focus on the evolution of N_2's PMF as σ changes from -0.08 to -0.16 C/m^2.

Figure 5-6 d-f shows the density profiles of water molecules and ions near spherical electrodes with different surface charge densities. As σ increases from -0.08 to -0.16 C/m^2, the first interfacial water layer exhibits only minor changes, i.e., the height of its density

peak only increases by 8%. Because the packing of the interfacial water molecules changes little, the solvent-effect component of N_2's PMF (and thus the total PMF) also has little change. This behavior is in sharp contrast to the situation near planar electrodes, where the density (and thus packing) of interfacial water molecules increases greatly as σ changes from -0.08 to -0.16 C/m^2. This difference originates mainly from the facts that the interfacial Li^+ ion density near spherical electrodes is always lower than that near planar electrodes with the same charge density (see Figure 5-6b,c and Figure 5-6e,f) and the increase of interfacial Li^+ ion density over the same surface charge density window is small (the Li^+ ion peak increases from 1.30 to 1.97 nm^{-3} near the spherical electrode, compared to from 3.06 to 7.63 nm^{-3} near the planar electrode). Consequently, the accumulation of water molecules near spherical electrode brought by the hydration of interfacial ions and their increases in number density when σ changes from -0.08 to -0.16 C/m^2 are both minor.

The lower Li^+ ion density near spherical electrodes and its weaker increase as σ becomes more negative compared to those near planar electrodes are caused mostly by the spherical electrode's small radius. In electrolytes with high ion concentration and hence small Debye length, one can approximate the EDL as a single Helmholtz-like counterion layer adsorbed on the electrode surface at a distance of *d*. For planar electrodes, the area density of the counterions in this layer is $|\sigma|/e$ (e is the elementary charge). For spherical electrodes with a radius of *R*, the area density of the counterions in this layer is reduced by a factor of $(1 + d/R)^2$ to $|\sigma|/e \times (1 + d/R)^{-2}$. In our system, R =1 nm and $d \approx 0.4$ nm (based on the position of the first Li^+ ion density peak, see Figure 5-6e), and therefore the area density of Li^+ ions adsorbed on the spherical electrode can be ~2 times smaller than that on the planar electrode. While this simple analysis neglects the finite thickness of the

EDL and underestimates the reduction of Li^+ ion density on the small spherical electrodes, it captures an essential aspect of the EDLs near electrodes with strong curvatures and thus helps elucidate the difference between Li^+ ion and water molecule accumulation (and ultimately the N_2 adsorption) in the EDLs near the spherical and planar electrodes.

5.4 Conclusions

The recent discovery that N_2 can be electrochemically reduced to NH_3 with excellent selectivity and activity on atomically sharp carbon nanospikes under ambient conditions has revealed a promising strategy for ammonia synthesis alternative to the conventional Haber-Bosch process.[134] It has been shown that the large curvature of the molecularly sharp nanospikes is the key for their superior performance. Elucidating the adsorption of N_2 on carbon nanospikes, an elementary step for N_2's electrochemical reduction, is essential toward the full understanding of the catalytic mechanism of the carbon nanospikes, which will hopefully lend support toward the optimization of material performance. However, the adsorption of small nonpolar molecules on electrodes (or more generally, in the EDLs near electrodes) is rarely studied, let alone the effect of electrode curvature on the adsorption.

In this work, we have studied the adsorption of N_2 molecules in EDLs and have calculated their PMF across the EDLs near planar and atomically sharp electrodes. The effects of surface charge and surface curvature of the electrodes on the gas adsorption behavior were explored in detail. It was found that the density of N_2 molecules in EDLs deviates from that in bulk electrolytes only within ~1.2 nm from the electrode surface, and contact-adsorbed N_2 molecules dominate the adsorption of N_2 in the EDLs. Overall, N_2 is enriched near neutral electrodes. As the electrodes become negatively electrified, the

adsorption of N_2 increases for the moderate surface charge density of -0.08 C/m^2, but decreases for the high surface charge density of -0.16 C/m^2. However, the suppression of N_2 adsorption in EDLs as the electrode becomes highly charged is much less pronounced near the high curvature 1-nm-radius spherical electrodes than near the planar electrodes. The electrochemically available N_2 molecules near highly charged spherical electrodes are one order of magnitude higher than those near similarly charged planar electrodes. This result suggests that, compared to the planar electrodes, electrodes with large curvatures can facilitate the electrochemical reduction of N_2 molecules, which may be one of the mechanisms underlying the extraordinary performance of the carbon nanospikes.

Analysis of the PMF of the N_2 molecules across the EDLs reveals that, while the N_2-electrode interactions contribute to the enrichment of N_2 in EDLs, solvent-induced effects play a profound role in the preferential adsorption of N_2 on the electrode surface, the evolution of N_2 adsorption as electrodes become electrified, as well as the dependence of N_2 adsorption on the curvature of the electrode. In particular, the packing of the first layer of interfacial water molecules on the electrode surface greatly affects the contact adsorption of N_2 molecules on the electrode surfaces. By changing the orientation of interfacial water molecules and drawing counterions toward the electrode surface, the surface charge and curvature of electrodes can modulate the amount of water molecules in this layer and their packing, thereby modulating the adsorption of N_2 molecules in the EDLs, e.g., leading to the non-monotonic variation of N_2 adsorption as the electrode becomes more negatively charged.

The present work focuses on the adsorption of N_2 molecules in EDLs. However, because prior work suggested that the gas adsorption on hydrophobic surfaces immersed

in water exhibits limited gas specificity,[135] the insight gained here should be relevant to the adsorption of other small gas molecules such as CO_2 on charged surfaces that do not form extensive hydrogen bonding with the water molecules. Therefore, the present work may help understand gas behavior on electrodes in other applications, e.g., the nucleation of bubbles on electrodes during electrochemical reactions that release poorly soluble gases. The knowledge acquired could also be applied toward other applications of carbon nanospikes and nanostructured electrodes for the electrochemical reduction of dissolved CO_2 to multi-carbon oxygenates in aqueous electrolytes.[204]

Supporting Information Available in Appendix D: Average spacing of the N_2 molecules adsorbed on electrode surfaces and distribution of water molecules near electrodes and N_2 molecules in bulk water.

Chapter 6: Summary of Contributions

This dissertation focuses on adsorption in three advanced materials systems: porous liquids, room-temperature ionic liquids, and atomically sharp electrodes. Although these materials systems differ from each other in their applications, they share the similarity that the adsorption is governed largely by molecular physics at liquid-solid interfaces. Even though the development and application of these materials systems calls for the adsorption to be quantified and its molecular details to be clarified, achieving these goals using only experimental and theoretical methods is difficult. Hence, in this dissertation, the adsorption of small molecules in these emerging material systems was investigated using molecular dynamics simulations to address these challenges, with the hope that the insights gained in here can be useful for the further development of these materials for applications such as molecule storage/separation, surface modification, and electrochemical catalysis.

The study of gas storage in porous liquids focused on understanding the adsorption of three prototypical small molecules (CO_2, CH_4, and N_2) in the newly synthesized porous liquids (crown-ether substituted cage molecules in a 15-crown-5 solvent). This study addresses the knowledge gap that, although porous liquids are promising materials for gas storage and separation, the adsorption behavior of gas molecules in these materials is little studied. The thermodynamics and kinetics of gas adsorption inside the porous liquids were investigated and the key findings include the following:

1. The capacity of gas storage in a cage molecule is governed by the non-electrostatic (dispersive) intermolecular interactions between the gas and the cage molecule, which decides the affinity of gas molecules to the cage, and size/shape of the gas molecules,

which decides whether the space inside the cage can be accessed. The mechanism clarified here lays foundation for the rational design of porous liquids with higher gas storage capacities.

2. The potential of porous liquids in gas separation was assessed. The selectivity of CO_2 over $CH_4(N_2)$ was observed in simulations with binary gas components, where both gas components are controlled to have same partial pressure in the gas reservoir. In the cage's core region, the strong van der Waals interactions between CO_2 and cage molecule enable CO_2 to outcompete CH_4 and N_2 and contributes to the selectivity of CO_2 over them. The study of adsorption isotherms for CO_2+CH_4 mixture revealed that the entropic effect becomes important as the gas partial pressure increases, which helps explain the reduced selectivity of CO_2 over CH_4 at elevated pressure.

3. Gas molecules can enter the cage molecule without noticeable energy barrier, while a modest energy penalty exists for a gas molecule to leave the cage molecule. Overall, the gas molecules inside the cage can exchange rather rapidly with those in the bulk solution.

The study of water adsorption at mica-ionic liquid interfaces focused on how the structure of adsorbed interfacial ions is affected by the presence water and electrification of the mica surfaces. Interfacial ionic liquids play a crucial role in applications such as lubrication and capacitive energy storage. While water is expected to reach the interfaces between ionic liquids and solid surfaces in practical systems in which water is ubiquitous, the adsorption of water at these interfaces and its impact on the structure of the interfacial ionic liquids are not well understood. This knowledge gap is addressed in this study by

examining the interfacial structure of [BMIM][Tf_2N] near mica surfaces in presence of water using MD simulations. The key insights gained from this study are as follows:

1. Near dry, neutral mica surface, $BMIM^+$ and Tf_2N^- ions are adsorbed into closely separated layers with little charge separation. Only the first layer of adsorbed $BMIM^+$ ions exhibit modest lateral and orientation ordering. Water molecules introduced at the neutral mica-ionic liquid interfaces displace the ions from the mica surface and the structuring of interfacial ions nearly diminishes.

2. Near dry, highly charged mica surfaces, alternating layering of $BMIM^+$ and Tf_2N^- ions is distinct, but the lateral and orientation ordering of the ions is obvious mainly in the first $BMIM^+$ layer. Introducing water into the system weakens the adsorption of $BMIM^+$ ions on the mica surface and the subsequent layering of Tf_2N^- and $BMIM^+$ ions away from the mica surface. Nevertheless, the lateral and orientation ordering of the $BMIM^+$ ions contact adsorbed on the mica surface becomes stronger and modest aggregation of the hydrophobic tails of the first and second layers of $BMIM^+$ ions occurs.

3. In presence of environmental water, the structure of the ionic liquids near a surface electrifiable via surface atom dissociation is governed by the *three-way coupling* between the self-organization of interfacial ions, adsorption of water at solid-ionic liquid interfaces, and the electrification of the surface. Delineating how these processes and their interplay depend on choice of ionic liquids, nature of the solid surfaces, and the availability of water in the environment will provide a mechanistic understanding of the interfacial structure of humid ionic liquids near solid surfaces.

4. Water adsorption at ionic liquids-solid interfaces may be as a new handle for manipulating the interfacial structure of ionic liquids. This approach complements the traditional approach of tailoring the molecular design of ionic liquids to tune their interfacial structure.

The study of adsorption of dissolved N_2 in EDL near planar and atomically sharp electrodes focused on the effect of surface charge and curvature on the gas adsorption behavior. The recent discovery of highly effective electrochemical reduction of N_2 to NH_3 under ambient conditions using atomically sharp carbon nanospikes demonstrated the large curvature of molecularly shape nanospikes is key for their superior performance. Although the adsorption of N_2 on the surface of these nanostructured carbon is a prerequisite for their reduction but little is known about such adsorption. In fact, the adsorption of small nonpolar molecules on electrodes is rarely studied in the past, let alone the effect of electrode curvature on the adsorption. This study seeks to close this knowledge gap and lend support to the optimization of material systems for N_2 adsorption and electrochemical reduction. The key findings of this study are as follows:

1. The density of N_2 molecules in EDLs deviates from that in bulk electrolytes only within ~1.2 nm from the electrode surface, and contact-adsorbed N_2 molecules dominate the adsorption of N_2 in the EDLs. The electrochemically available N_2 molecules near highly charged spherical electrodes are one order of magnitude higher than those near similarly charged planar electrodes. Compared to the planar electrodes, electrodes with large curvatures can facilitate the electrochemical reduction of N_2 molecules, which may be one of the mechanisms underlying the extraordinary performance of the carbon nanospikes.

2. While the N_2-electrode interactions contribute to the enrichment of N_2 in EDLs, solvent-induced effects play a profound role in the preferential adsorption of N_2 on the electrode surface, the evolution of N_2 adsorption as electrodes become electrified, as well as the dependence of N_2 adsorption on the curvature of the electrode. In particular, the packing of the first layer of interfacial water molecules on the electrode surface greatly affects the contact adsorption of N_2 molecules on the electrode surfaces. By changing the orientation of interfacial water molecules and drawing counterions toward the electrode surface, the surface charge and curvature of electrodes can modulate the amount of water molecules in this layer and their packing, thereby modulating the adsorption of N_2 molecules in the EDLs, e.g., leading to the non-monotonic variation of N_2 adsorption as the electrode becomes more negatively charged.

3. Because prior work suggested that the gas adsorption on hydrophobic surfaces immersed in water exhibits limited gas specificity, the insight gained here should be relevant to the adsorption of other small gas molecules such as CO_2 on charged surfaces that do not form extensive hydrogen bonding with the water molecules. The present work may help understand gas behavior on electrodes and application of carbon nanospikes for electrochemical reactions.

The three studies performed in this dissertation are rather different at the first sight but they all feature the adsorption of small molecules on the newly emerged materials. These studies represent the initial attempts to understand the molecular mechanism of adsorption in porous liquids, at mica-ionic liquid interfaces, and near atomically sharp electrodes. The insights gained in this work fill critical knowledge gaps in the understanding of adsorption

in these materials and will help optimize their design and engineering for target applications such as gas adsorption, lubrication, and electrochemical catalysis.

Appendix

Appendix A: Supporting Information for Chapter 2

1. Rigidity of the solvent molecules in porous liquids

Here we examine the rigidity of the cage molecules dispersed inside solvents. To this end, we super-impose the structure of the cage molecules at five representative time instants. Figure A-1 shows that the fluctuation of the cage structure (in particular its gas access window and inner cavity) is much smaller compared to the size of the gas molecules studied here. Therefore, the flexibility of the cage molecule plays a minor role in the gas storage.

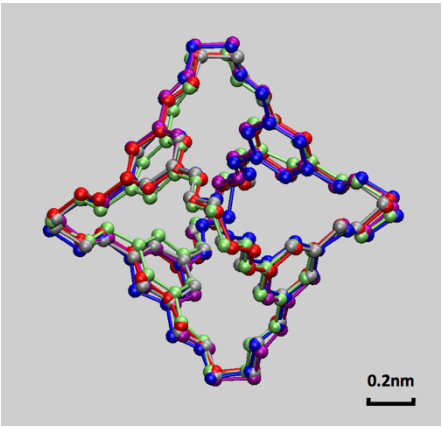

Figure A-1. Superposition of the structure of a cage molecule at five time instants (red: 1ns, blue: 2ns, yellow: 3ns, purple: 4ns, cyan: 5ns). The cage molecule was immersed in the solvent during simulation.

2. Diffusion of solvent molecules in porous liquids

For accurate determination of the gas storage in porous liquids, the solvent and gas molecules in the system must be adequately equilibrated. Since the movement of gas molecules in porous liquids studied in this work is facile, here we examine the movement of the solvent molecules.

Figure A-2 shows the mean-square displacement (MSD) of the solvent and cage molecules in the system with 20 cage molecules, 400 solvent molecules, and 60 CH_4. We observe that, over a time period of 2ns, a solvent molecule diffuses ~1nm on average, which is larger than its size. Since we equilibrated the system for 5ns before production run, solvents should be sufficiently equilibrated in our system.

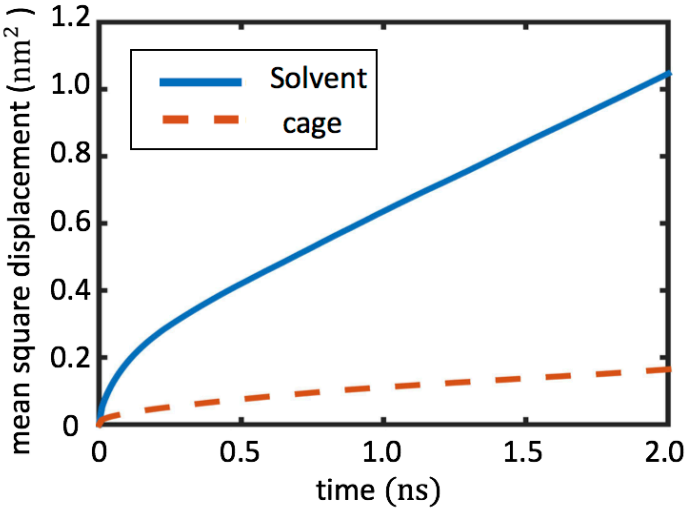

Figure A-2. The mean-square-displacement of solvent and cage molecules in a porous liquids (N_{cage} = 20, N_{CH4}=60, $N_{solvent}$=400, T=400K, P=1bar).

3. Solvent distribution along the cage's entrance vector

Figure 2-6a in the main text shows the PMF profile for gas molecule along the entrance vector of the cage. A distinct peak was observed at a distance of ~0.85nm from the cage center. This peak originates from the dense packing of solvent molecules outside the cage's access window, which hinders gas from entering into the cage. Figure A-3 shows the density profile of the solvent molecules along the cage's entrance vector. A peak is observed at a distance of 0.8nm from the cage center, indicating density packing of solvent molecules near this location. This dense packing, induced by the rigid cage molecules, makes it difficult to insert a gas molecule at the same location. Therefore, a peak is observed for the PMF of the gas molecules at this location.

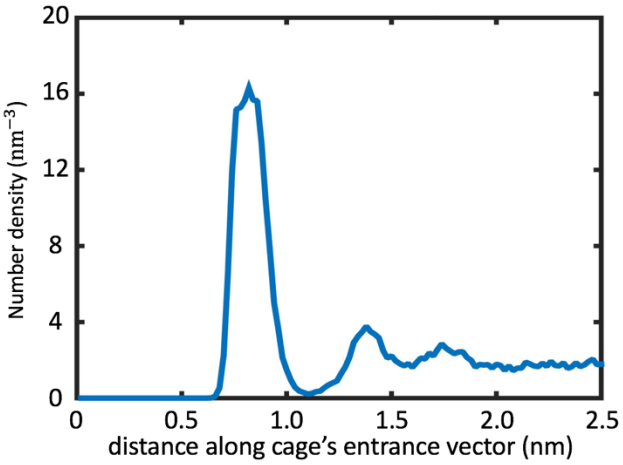

Figure A-3. The density profile of solvent molecules along the entrance vector of a cage molecule. The position of solvent molecules is based on their center-of-mass.

Appendix B: Supporting Information for Chapter 3

1. Distribution of gas molecules in the MD system

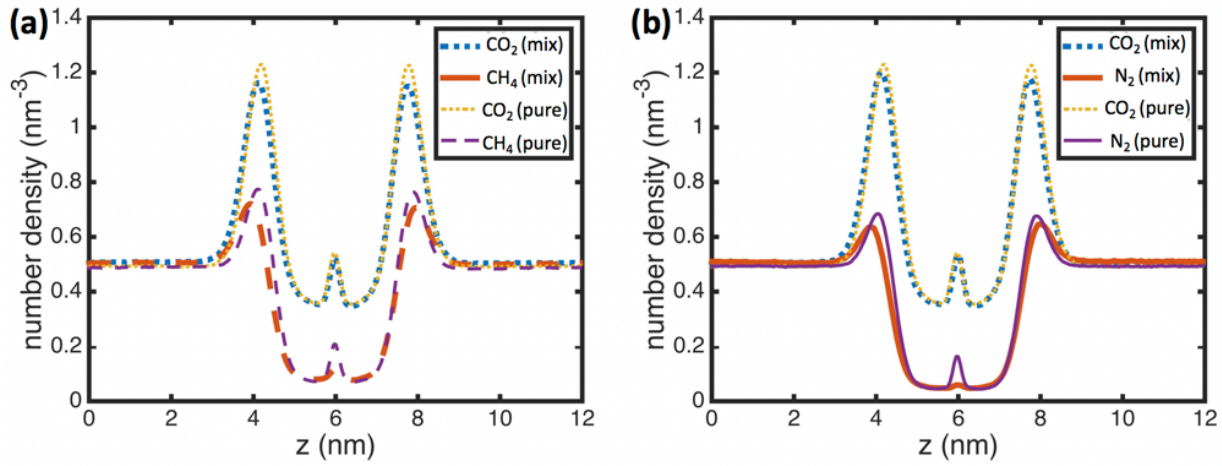

Figure B-1. Distribution of gas molecules across the simulation box in different systems. (a) Systems with gas bath filled with pure CO_2, pure CH_4, and 1:1 CO_2+CH_4 mixture. (b) System with gas bath filled with pure CO_2, pure N_2, and 1:1 CO_2+N_2 mixture.

Since the gas density in the gas bath is rather modest, the partial pressure of each gas component can be calculated from its number density using the ideal gas law:

$$p = \frac{n}{V}RT \qquad (B-1)$$

where p is the partial pressure of the gas component, n is the number of moles for the gas component, V is the volume of the gas component, which makes $\frac{n}{V}$ the number density of the gas component in the gas bath, R is the ideal gas constant ($8.314\ \mathrm{J/(K\cdot mol)}$), and T is the temperature (400 K). The partial pressure of each gas component is thus calculated to be 27.5 bar with an error bar of ± 0.3 bar.

2. Isosurfaces for gas density of CO_2 and N_2 inside cage molecules

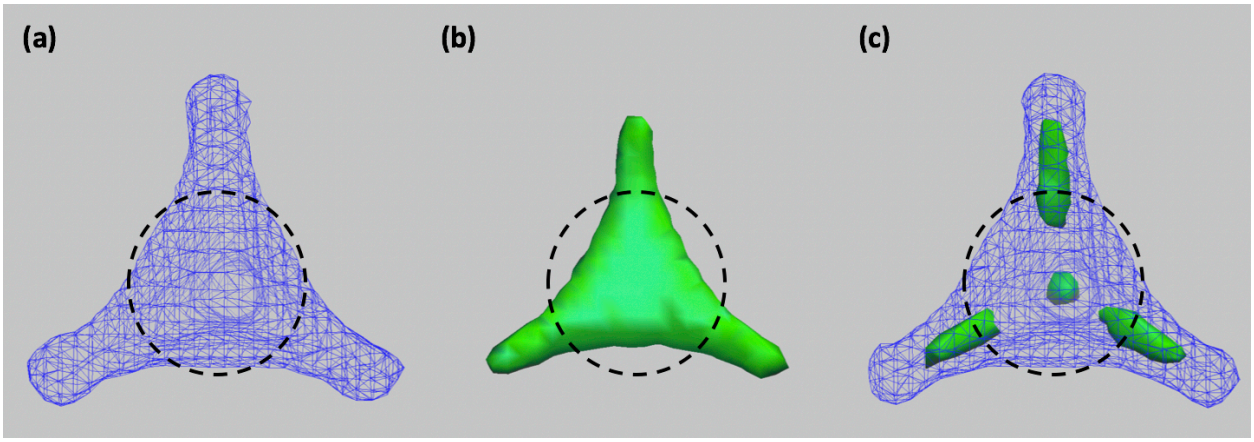

Figure B-2. Isosurface of CO_2 (blue) and N_2 (yellow) gas density inside a cage molecule in equilibrium with a gas bath containing pure CO_2 (a), pure N_2 (b), and mixture of CO_2 and N_2 molecules (c). The isosurface is set to a density of 4 nm^{-3}. The black dashed line marks the boundary between the cage's core region and branch regions. Partial pressure of all gas in the gas bath is 27.5 ± 0.3 bar.

Note that the density of shown isosurface here is 4 nm^{-3}, which is lower than the value of 15 nm^{-3} used in Figure 3-4. The density of N_2 gas molecules is relatively low inside the cage, thus the isosurface needs to be shown with a smaller gas density (otherwise nothing will be visible).

Appendix C: Supporting Information for Chapter 4

1. Force field parameters

Table C-1. The LJ potential parameter for the particles in [BMIM][Tf_2N]

Particle	σ (A)	ε (kCal/mol)	Particle	σ (A)	ε (kCal/mol)
CmU	3.6757	0.2336	H	1.8316	0.0197
C	3.1938	0.0499	Cu1, Cu2	3.9818	0.1100
N1, N2	2.9768	0.0499	Cm	3.4886	0.0855
Cy, Cy*	3.6356	0.0599	S	3.8381	0.1199
CmN	3.7945	0.0596	N-	3.6917	0.0449
H	1.8316	0.0197	F	3.1182	0.0369
Cu1, Cu2	3.9818	0.1100	O	2.9031	0.0899

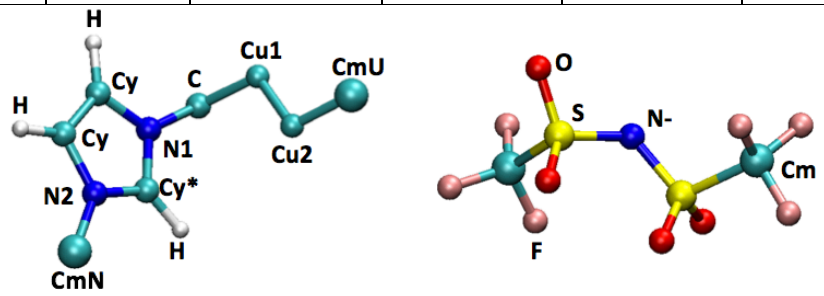

2. Relative humidity of the virtual ambient environment

2.1 Methods

As shown in Fig. C-1, our MD system features mica surface, RTILs, and water molecules. The water molecules in the interfacial zone (zone A) are in equilibrium with the water vapor above the RTIL film (zone C), which has a density of ρ_v. Since the water vapor in zone C has a low density, it is an ideal gas and can be thought to be in equilibrium with a virtual ambient environment (its temperature is 300K as in our system) with a relative humidity RH satisfying

$$p_0 \times \mathrm{RH} = \rho_v k_B T \qquad \text{(C-1)}$$

where $p_0 = 3.525$kPa is the saturated vapor pressure of water at 300K and k_B is the Boltzmann constant. If ρ_v is known, the relative humidity of the virtual ambient environment with which the interfacial water molecules in our MD system are in equilibrium is known via Equation C-1.

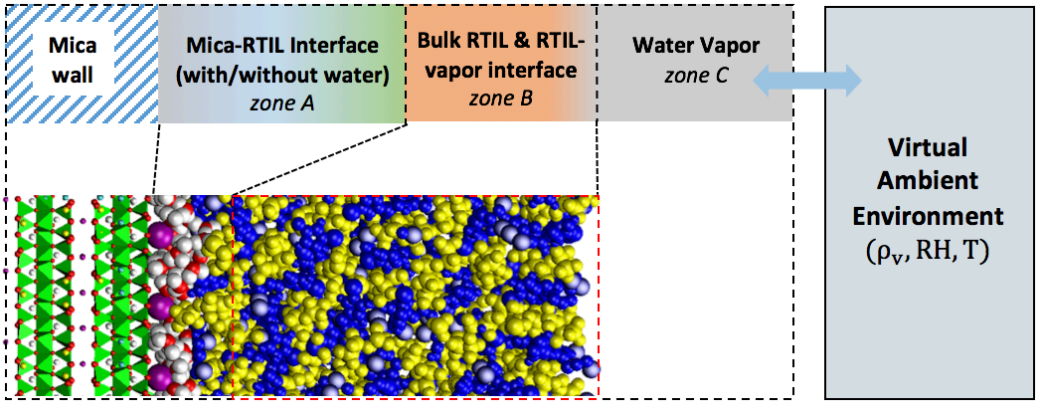

Figure C-1. The setup of the simulation system. Note that a large free space is introduced above the ionic liquid film.

Evaluating ρ_v directly from MD trajectories, however, is difficult. In our simulations, most water molecules remain in the interfacial zone (zone A) and the density of water in zone C is too low to be computed with a small relative error. We thus adopt an alternative method to compute ρ_v. At equilibrium, following the Boltzmann distribution,

$$\frac{\rho(z)}{\rho_v} = \exp\left(-\frac{\phi(z)}{k_B T}\right) \tag{C-2}$$

where $\rho(z)$ is the water density at position z in the interfacial zone. $\phi(z)$ is the potential of mean force (PMF) of a water molecule at position z relative that in the free space above the RTIL film. We use the Umbrella sampling technique to compute $\phi(z)$.[190, 205] Specifically, we randomly select a water molecule in our MD system as a probing molecule and perform a series of simulations in which this molecule is restrained at various z-positions ($z_0 \leq z \leq z_v$; Δz=0.05nm) across the system. Umbrella sampling is a well-established PMF calculation method, and, by constraining the probing molecule at different positions, it enables us to sample the state of water molecules in

the bulk RTIL and water vapor zones easily, which are difficult to access in regular, unconstrained simulations. For the PMF computed using the Umbrella sampling to be valid, two conditions must be met: (1) the probing water molecule is in equilibrium with its local environment and (2) the local environment experienced by a probing water molecule at position z in a constrained simulation must be the same as that by a water molecule at the same position in the unconstrained simulations. Condition 1 is met by running each constrained simulation for a long time (10ns is sufficient in our case). Condition 2 is also met in each of the three zones. For example, in the bulk RTIL and vapor zones, the water density is so low that any water molecule in these zones found in an unconstrained simulation is surrounded only by RTILs, which is exactly the case in our constrained simulations.

In the above Umbrella sampling calculations, z_0 and z_v can, in principle, be any point in the interfacial zone (zone A) and the free space above the RTIL film (zone C), respectively. Practically, z_0 must be a location where water density can be determined accurately in MD simulations so that Equation C-2 can be evaluated accurately later. z_v is chosen to be 7nm above the mica surface (~1nm above the RTIL film) and the PMF here is taken as zero. Combining the PMF calculation and Equations C-1 and C-2, the relative humidity of the virtual ambient environment with which the interfacial water molecules are in equilibrium is

$$\mathrm{RH} = \frac{k_B T \rho(z_0)}{p_0} e^{\phi(z_0)/k_B T} \qquad \text{(C-3)}$$

2.2 Results

Figure C-2 shows the density and PMF of water molecules near the neutral mica surface in the system presented in Fig. 4-3. Using the data in this figure (z_0 = 0.5 nm, $\rho_w(z_o) = 23.2\ \mathrm{nm}^{-3}$, and $\phi(z_0) = -7.1$kCal/mol), the relative humidity of the virtual ambient environment with which

the interfacial water molecules are in equilibrium is calculated as $20.5\% \pm 11.3\%$. Figure C-3 shows the density and PMF of water molecules near the fully electrified mica surface in the system presented in Fig. 4-4. Using the data in this figure (z_0 = 0.5 nm, $\rho_w(z_o) = 23.7\ \mathrm{nm}^{-3}$, and $\phi(z_0) = -7.9$kCal/mol), the relative humidity of the virtual ambient environment with which the interfacial water molecules are in equilibrium is calculated as $4.9\% \pm 3.9\%$.

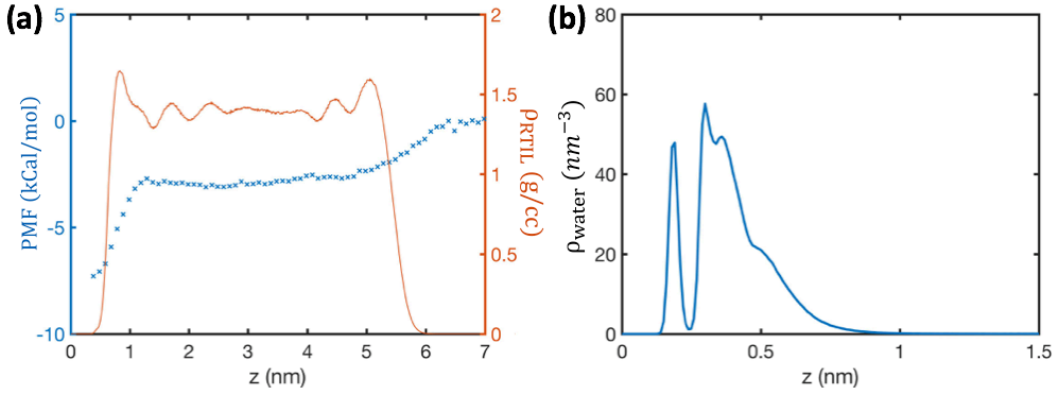

Figure C-2. The potential of mean force (PMF) of water molecules and RTIL mass density (a) and the water density profile (b) across the MD system. The mica surface is neutral. *z*=0 corresponds to the surface of the mica surface.

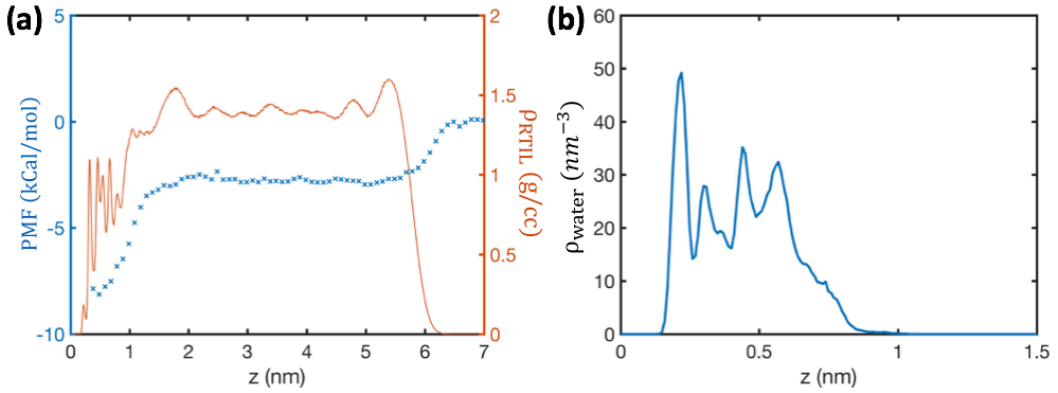

Figure C-3. The potential of mean force (PMF) of water molecules and RTIL mass density (a) and the water density profile (b) across the MD system. The mica surface has a net surface charge density of -0.33C/m^2. *z*=0 corresponds to the surface of the mica surface.

3. Accumulation of water at RTIL-mica interfaces

Water molecules introduced in the mica-RTIL systems exist as a thin liquid film on the mica surface in the main text. The phase separation of water from bulk RTILs is expected since the load

of water in the system far exceeds its solubility in the RTILs. However, whether and how water molecules are accommodated on the solid substrate depend on the substrate's nature. If the substrate is less hydrophilic, water may phase separate from the bulk ILs in other forms. To see this, we removed the partial charge on the mica atoms to make the mica less hydrophilic and re-run the system consisting of neutral mica, water and ILs. Although water initially exists as a thin film on the mica, it becomes a droplet within 3ns (see Fig. C-4).

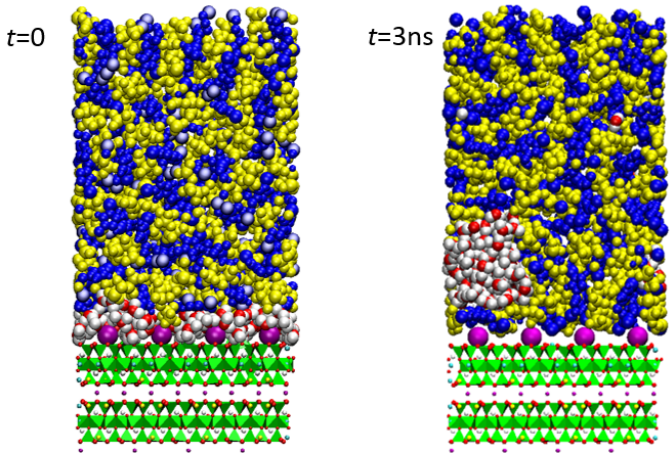

Figure C-4. *Evolution of the water molecules in the system featuring neutral mica and ILs*. The partial charge on all mica atoms are removed at $t = 0$ to make the mica less hydrophilic.

Appendix D: Supporting Information for Chapter 5

1. Average spacing of the N_2 molecules adsorbed on electrode surfaces

The N_2 molecules within a cutoff distance of 0.5nm from the electrode surface (corresponding to the N_2's first PMF peak near the electrode) are considered as adsorbed on the electrode. By integrating the N_2 density determining using Equation (5-1) from the electrode surface to this cutoff distance, the area density of the adsorbed N_2 molecules on the electrodes studied here (curvature: $R = \infty$ and 1 nm; electrode surface charge density: $\sigma = 0, -0.08,$ and $-0.16 C/m^2$) is found to be in the range of 0.36 to 5.33×10^{-4} nm^{-2}. The average spacing between two adsorbed N_2 molecules is thus in the range of 43 to 167 nm.

2. Distribution of water molecules near electrodes and N_2 molecules in bulk water

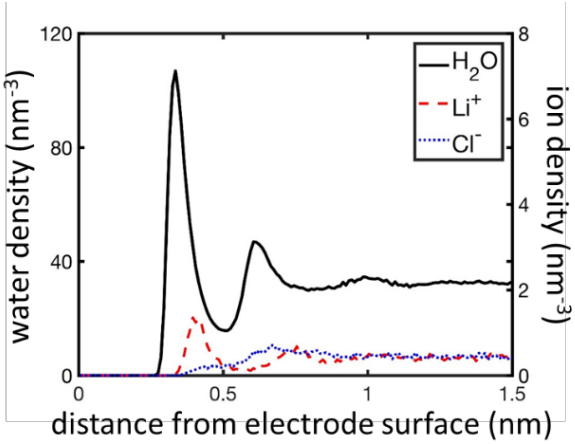

Figure D-1. The density profile of water molecules and ions near a planar electrode with zero charge.

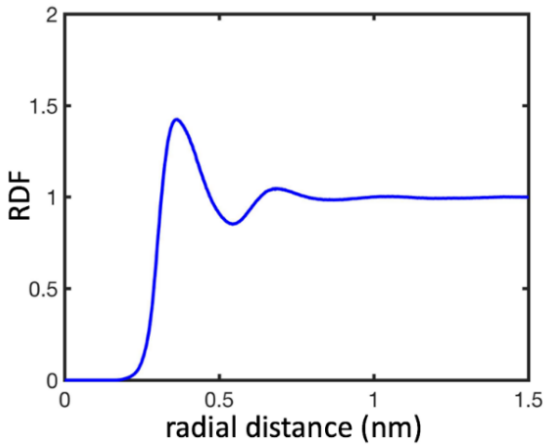

Figure D-2. The radial distribution function (RDF) of water molecules with respect to an isolated N_2 molecule in bulk water.

Reference

(1) Tien, C. *Introduction to Adsorption : Basics, Analysis, and Applications*; 1st edition.; Elsevier: Cambridge, MA, 2018.

(2) Simon, P.; Gogotsi, Y. Materials for Electrochemical Capacitors. *Nat. Mater.* **2008**, *7*, 845-854.

(3) Perkin, S.; Albrecht, T.; Klein, J. Layering and Shear Properties of an Ionic Liquid, 1-Ethyl-3-Methylimidazolium Ethylsulfate, Confined to Nano-Films between Mica Surfaces. *Phys. Chem. Chem. Phys.* **2010**, *12*, 1243-1247.

(4) Li, H.; Rutland, M. W.; Atkin, R. Ionic Liquid Lubrication: Influence of Ion Structure, Surface Potential and Sliding Velocity. *Phys. Chem. Chem. Phys.* **2013**, *15*, 14616-14623.

(5) Eshetu, G. G.; Armand, M.; Scrosati, B.; Passerini, S. Energy Storage Materials Synthesized from Ionic Liquids. *Angew. Chem. Int. Ed.* **2014**, *53*, 13342-13359.

(6) MacFarlane, D. R.; Tachikawa, N.; Forsyth, M.; Pringle, J. M.; Howlett, P. C.; Elliott, G. D.; Davis, J. H.; Watanabe, M.; Simon, P.; Angell, C. A. Energy Applications of Ionic Liquids. *Energy Environ. Sci.* **2014**, *7*, 232-250.

(7) Fajardo, O. Y.; Bresme, F.; Kornyshev, A. A.; Urbakh, M. Electrotunable Friction with Ionic Liquid Lubricants: How Important Is the Molecular Structure of the Ions? *J. Phys. Chem. Lett.* **2015**, *6*, 3998-4004.

(8) Lian, C.; Liu, K.; Liu, H. L.; Wu, J. Z. Impurity Effects on Charging Mechanism and Energy Storage of Nanoporous Supercapacitors. *J. Phys. Chem. C* **2017**, *121*, 14066-14072.

(9) Osti, N. C.; Dyatkin, B.; Thompson, M. W.; Tiet, F.; Zhang, P. F.; Dai, S.; Tyagi, M.; Cummings, P. T.; Gogotsi, Y.; Wesolowski, D. J.; Mamontov, E. Influence of Humidity on Performance and Microscopic Dynamics of an Ionic Liquid in Supercapacitor. *Physical Review Materials* **2017**, *1*, 035402.

(10) Kim, H.; Yang, S.; Rao, S. R.; Narayanan, S.; Kapustin, E. A.; Furukawa, H.; Umans, A. S.; Yaghi, O. M.; Wang, E. N. Water Harvesting from Air with Metal-Organic Frameworks Powered by Natural Sunlight. *Science* **2017**, *356*, 430-432.

(11) Saleh, T. A. *Applying Nanotechnology to the Desulfurization Process in Petroleum Engineering*; Engineering Science Reference: Hershey, PA, 2016.

(12) Middleton, R.; Viswanathan, H.; Currier, R.; Gupta, R. Co2 as a Fracturing Fluid: Potential for Commercial-Scale Shale Gas Production and Co2 Sequestration. *12th International Conference on Greenhouse Gas Control Technologies, Ghgt-12* **2014**, *63*, 7780-7784.

(13) Li, H.; Eddaoudi, M.; O'Keeffe, M.; Yaghi, O. M. Design and Synthesis of an Exceptionally Stable and Highly Porous Metal-Organic Framework. *Nature* **1999**, *402*, 276-279.

(14) Yaghi, O. M.; Li, G. M.; Li, H. L. Selective Binding and Removal of Guests in a Microporous Metal-Organic Framework. *Nature* **1995**, *378*, 703-706.

(15) Perez, E. V.; Karunaweera, C.; Musselman, I. H.; Balkus, K. J.; Ferraris, J. P. Origins and Evolution of Inorganic-Based and Mof-Based Mixed-Matrix Membranes for Gas Separations. *Processes* **2016**, *4*.

(16) Hermes, S.; Schroder, F.; Amirjalayer, S.; Schmid, R.; Fischer, R. A. Loading of Porous Metal-Organic Open Frameworks with Organometallic Cvd Precursors: Inclusion Compounds of the Type [Lnm](a)@Mof-5. *J. Mater. Chem.* **2006**, *16*, 2464-2472.

(17) Millward, A. R.; Yaghi, O. M. Metal-Organic Frameworks with Exceptionally High Capacity for Storage of Carbon Dioxide at Room Temperature. *J. Am. Chem. Soc.* **2005**, *127*, 17998-17999.

(18) Kiselev, V. F.; Krylov, O. V.; Krylov, O. V. *Adsorption and Catalysis on Transition Metals and Their Oxides*; Springer-Verlag: Berlin ; New York, 1989.

(19) Kaneda, T.; Bates, J. B.; Wang, J. C.; Engstrom, H. Effect of H2o on the Ionic-Conductivity of Sodium Beta-Alumina. *Mater. Res. Bull.* **1979**, *14*, 1053-1056.

(20) Freundlich, H. Über Die Adsorption in Lösungen. *Z. Phys. Chem.* **1907**, *57*, 385-470.

(21) Polanyi, M. Adsorption Von Gasen (Dampfen) Durch Ein Festes Nichtfluchtiges Adsorbens. *Verhandlungen der Deutschen Physekalischen Gesellschaft* **1916**, *18*, 55-80.

(22) Chiou, C. T. *Partition and Adsorption of Organic Contaminants in Environmental Systems*; Wiley-Interscience: Hoboken, N.J., 2002.

(23) Manes, M. Activated Carbon Adsorption Fundamentals. *Encyclopedia of environmental analysis and remediation* **1998**, *1*, 26-68.

(24) Langmuir, I. The Adsorption of Gases on Plane Surfaces of Glass, Mica and Platinum. *J. Am. Chem. Soc.* **1918**, *40*, 1361-1403.

(25) Brunauer, S.; Emmett, P. H.; Teller, E. Adsorption of Gases in Multimolecular Layers. *J. Am. Chem. Soc.* **1938**, *60*, 309-319.

(26) Qiu, H.; Lv, L.; Pan, B. C.; Zhang, Q. J.; Zhang, W. M.; Zhang, Q. X. Critical Review in Adsorption Kinetic Models. *Journal of Zhejiang University-Science A* **2009**, *10*, 716-724.

(27) K, L. S. About the Theory of So-Called Adsorption of Soluble Substances. *Sven. Vetenskapsakad. Handingarl* **1898**, *24*, 1-39.

(28) Zeldowitsch, J. Über Den Mechanismus Der Katalytischen Oxydation Von Co an Mno2. *Acta Physicochemical URSS* **1934**, *1*, 364-449.

(29) Ho, Y. S.; McKay, G. A Comparison of Chemisorption Kinetic Models Applied to Pollutant Removal on Various Sorbents. *Process Safety and Environmental Protection* **1998**, *76*, 332-340.

(30) Ho, Y. S. Review of Second-Order Models for Adsorption Systems. *J. Hazard. Mater.* **2006**, *136*, 681-689.

(31) Boyd, G. E.; Adamson, A. W.; Myers, L. S. The Exchange Adsorption of Ions from Aqueous Solutions by Organic Zeolites .2. *J. Am. Chem. Soc.* **1947**, *69*, 2836-2848.

(32) Cooney, D. O. *Adsorption Design for Wastewater Treatment*; Lewis Publishers: Boca Raton, Fl., 1999.

(33) Li, Y.; Yang, R. T. Gas Adsorption and Storage in Metal-Organic Framework Mof-177. *Langmuir* **2007**, *23*, 12937-12944.

(34) Frenkel, D.; Smit, B. *Understanding Molecular Simulation : From Algorithms to Applications*; 2nd ed.; Academic Press: San Diego, 2002.

(35) Adams, D. J. Grand Canonical Ensemble Monte-Carlo for a Lennard-Jones Fluid. *Mol. Phys.* **1975**, *29*, 307-311.

(36) Mccrackin, F. L. Configuration of Isolated Polymer Molecules Adsorbed on Solid Surfaces Studied by Monte-Carlo Computer Simulation. *J. Chem. Phys.* **1967**, *47*, 1980.

(37) Eisenriegler, E.; Kremer, K.; Binder, K. Adsorption of Polymer-Chains at Surfaces - Scaling and Monte-Carlo Analyses. *J. Chem. Phys.* **1982**, *77*, 6296-6320.

(38) Soto, J. L.; Myers, A. L. Monte-Carlo Studies of Adsorption in Molecular-Sieves. *Mol. Phys.* **1981**, *42*, 971-983.

(39) Finn, J. E.; Monson, P. A. Prewetting at a Fluid-Solid Interface Via Monte-Carlo Simulation. *Phys. Rev. A* **1989**, *39*, 6402-6408.

(40) Delville, A. Monte-Carlo Simulations of Surface Hydration - an Application to Clay Wetting. *J. Phys. Chem.* **1995**, *99*, 2033-2037.

(41) Yamakov, V.; Milchev, A.; Borisov, O.; Dunweg, B. Adsorption of a Polyelectrolyte Chain on a Charged Surface: A Monte Carlo Simulation of Sealing Behaviour. *J. Phys. Condens. Matter* **1999**, *11*, 9907-9923.

(42) Lamari, F. D.; Levesque, D. Monte Carlo Simulations of Hydrogen Adsorption in Single-Walled Carbon Nanotubes. *J. Chem. Phys.* **1998**, *109*, 4981-4984.

(43) Darkrim, F.; Vermesse, J.; Malbrunot, P.; Levesque, D. Monte Carlo Simulations of Nitrogen and Hydrogen Physisorption at High Pressures and Room Temperature. Comparison with Experiments. *J. Chem. Phys.* **1999**, *110*, 4020-4027.

(44) Dresselhaus, M. S.; Williams, K. A.; Eklund, P. C. Hydrogen Adsorption in Carbon Materials. *MRS Bull.* **1999**, *24*, 45-50.

(45) Simonyan, V. V.; Diep, P.; Johnson, J. K. Molecular Simulation of Hydrogen Adsorption in Charged Single-Walled Carbon Nanotubes. *J. Chem. Phys.* **1999**, *111*, 9778-9783.

(46) Malbrunot, P.; Vidal, D.; Vermesse, J. Storage of Gases at Room Temperature by Adsorption at High Pressure. *Appl. Therm. Eng.* **1996**, *16*, 375-382.

(47) Darkrim, F.; Aoufi, A.; Malbrunot, P.; Levesque, D. Hydrogen Adsorption in the Naa Zeolite: A Comparison between Numerical Simulations and Experiments. *J. Chem. Phys.* **2000**, *112*, 5991-5999.

(48) Mellot, C. F.; Cheetham, A. K. Energetics and Structures of Fluoro- and Chlorofluorocarbons in Zeolites: Force Field Development and Monte Carlo Simulations. *J. Phys. Chem. B* **1999**, *103*, 3864-3868.

(49) MacKinnon, J. A.; Eckert, J.; Coker, D. F.; Bug, A. L. R. Computational Study of Molecular Hydrogen in Zeolite Na-A. Ii. Density of Rotational States and Inelastic Neutron Scattering Spectra. *J. Chem. Phys.* **2001**, *114*, 10137-10150.

(50) Anderson, C. R.; Coker, D. F.; Eckert, J.; Bug, A. L. R. Computational Study of Molecular Hydrogen in Zeolite Na-A. I. Potential Energy Surfaces and Thermodynamic Separation Factors for Ortho and Para Hydrogen. *J. Chem. Phys.* **1999**, *111*, 7599-7613.

(51) Lee, J.; Farha, O. K.; Roberts, J.; Scheidt, K. A.; Nguyen, S. T.; Hupp, J. T. Metal-Organic Framework Materials as Catalysts. *Chem. Soc. Rev.* **2009**, *38*, 1450-1459.

(52) Cho, S. H.; Ma, B. Q.; Nguyen, S. T.; Hupp, J. T.; Albrecht-Schmitt, T. E. A Metal-Organic Framework Material That Functions as an Enantioselective Catalyst for Olefin Epoxidation. *Chem. Commun.* **2006**, 2563-2565.

(53) Yang, Q. Y.; Zhong, C. L. Understanding Hydrogen Adsorption in Metal-Organic Frameworks with Open Metal Sites: A Computational Study. *J. Phys. Chem. B* **2006**, *110*, 655-658.

(54) Dubbeldam, D.; Galvin, C. J.; Walton, K. S.; Ellis, D. E.; Snurr, R. Q. Separation and Molecular-Level Segregation of Complex Alkane Mixtures in Metal-Organic Frameworks. *J. Am. Chem. Soc.* **2008**, *130*, 10884.

(55) Li, Y. Z.; Wang, H. H.; Yang, H. Y.; Hou, L.; Wang, Y. Y.; Zhu, Z. H. An Uncommon Carboxyl-Decorated Metal-Organic Framework with Selective Gas Adsorption and Catalytic Conversion of Co2. *Chemistry-a European Journal* **2018**, *24*, 865-871.

(56) Severin, E. S.; Tildesley, D. J. A Methane Molecule Adsorbed on a Graphite Surface. *Mol. Phys.* **1980**, *41*, 1401-1418.

(57) Talbot, J.; Tildesley, D. J.; Steele, W. A. Molecular-Dynamics Simulation of Fluid N-2 Adsorbed on a Graphite Surface. *Faraday Discuss.* **1985**, *80*, 91-105.

(58) Sikkenk, J. H.; Indekeu, J. O.; Vanleeuwen, J. M. J.; Vossnack, E. O. Molecular-Dynamics Simulation of Wetting and Drying at Solid-Fluid Interfaces. *Phys. Rev. Lett.* **1987**, *59*, 98-101.

(59) Langel, W.; Parrinello, M. Ab-Initio Molecular-Dynamics of H2o Adsorbed on Solid Mgo. *J. Chem. Phys.* **1995**, *103*, 3240-3252.

(60) Haase, F.; Sauer, J.; Hutter, J. Ab Initio Molecular Dynamics Simulation of Methanol Adsorbed in Chabazite. *Chem. Phys. Lett.* **1997**, *266*, 397-402.

(61) Imamura, Y.; Morikawa, Y.; Yamasaki, T.; Nakatsuji, H. First-Principles Molecular-Dynamics Study of Acetylene Adsorption on the Si(001) Surface. *Surf Sci.* **1995**, *341*, L1091-L1095.

(62) Gross, A.; Scheffler, M. Ab Initio Quantum and Molecular Dynamics of the Dissociative Adsorption of Hydrogen on Pd(100). *Physical Review B* **1998**, *57*, 2493-2506.

(63) Magda, J. J.; Tirrell, M.; Davis, H. T. Molecular-Dynamics of Narrow, Liquid-Filled Pores. *J. Chem. Phys.* **1985**, *83*, 1888-1901.

(64) Garofalini, S. H. Molecular-Dynamics Computer-Simulations of Silica Surface-Structure and Adsorption of Water-Molecules. *J. Non-Cryst. Solids* **1990**, *120*, 1-12.

(65) Yashonath, S.; Demontis, P.; Klein, M. L. Temperature and Concentration-Dependence of Adsorption Properties of Methane in Nay - a Molecular-Dynamics Study. *J. Phys. Chem.* **1991**, *95*, 5881-5889.

(66) Sarkisov, L.; Monson, P. A. Modeling of Adsorption and Desorption in Pores of Simple Geometry Using Molecular Dynamics. *Langmuir* **2001**, *17*, 7600-7604.

(67) Skoulidas, A. I. Molecular Dynamics Simulations of Gas Diffusion in Metal-Organic Frameworks: Argon in Cubtc. *J. Am. Chem. Soc.* **2004**, *126*, 1356-1357.

(68) Yang, Q. Y.; Zhong, C. L. Molecular Simulation of Adsorption and Diffusion of Hydrogen in Metal-Organic Frameworks. *J. Phys. Chem. B* **2005**, *109*, 11862-11864.

(69) Rosenbach, N.; Jobic, H.; Ghoufi, A.; Salles, F.; Maurin, G.; Bourrelly, S.; Llewellyn, P. L.; Devic, T.; Serre, C.; Ferey, G. Quasi-Elastic Neutron Scattering and Molecular Dynamics Study of Methane Diffusion in Metal Organic Frameworks Mil-47(V) and Mil-53(Cr). *Angew. Chem. Int. Ed.* **2008**, *47*, 6611-6615.

(70) Skoulidas, A. I.; Sholl, D. S. Self-Diffusion and Transport Diffusion of Light Gases in Metal-Organic Framework Materials Assessed Using Molecular Dynamics Simulations. *J. Phys. Chem. B* **2005**, *109*, 15760-15768.

(71) Chen, L. J.; Mowat, J. P. S.; Fairen-Jimenez, D.; Morrison, C. A.; Thompson, S. P.; Wright, P. A.; Duren, T. Elucidating the Breathing of the Metal-Organic Framework Mil-53(Sc) with Ab Initio Molecular Dynamics Simulations and in Situ X-Ray Powder Diffraction Experiments. *J. Am. Chem. Soc.* **2013**, *135*, 15763-15773.

(72) Spohr, E.; Heinzinger, K. A Molecular-Dynamics Study on the Water Metal Interfacial Potential. *Berichte Der Bunsen-Gesellschaft-Physical Chemistry Chemical Physics* **1988**, *92*, 1358-1363.

(73) Raghavan, K.; Foster, K.; Motakabbir, K.; Berkowitz, M. Structure and Dynamics of Water at the Pt(111) Interface - Molecular-Dynamics Study. *J. Chem. Phys.* **1991**, *94*, 2110-2117.

(74) Rhee, Y. J.; Halley, J. W.; Hautman, J.; Rahman, A. Ewald Methods in Molecular-Dynamics for Systems of Finite Extent in One of 3 Dimensions. *Physical Review B* **1989**, *40*, 36-42.

(75) Marchesi, M. Molecular-Dynamics Simulation of Liquid Water between 2 Walls. *Chem. Phys. Lett.* **1983**, *97*, 224-230.

(76) Glosli, J. N.; Philpott, M. R. Molecular-Dynamics Simulation of Adsorption of Ions from Aqueous-Media onto Charged Electrodes. *J. Chem. Phys.* **1992**, *96*, 6962-6969.

(77) Philpott, M. R.; Glosli, J. N.; Zhu, S. B. Molecular-Dynamics Simulation of Adsorption in Electric Double-Layers. *Surf Sci.* **1995**, *335*, 422-431.

(78) Fedorov, M. V.; Kornyshev, A. A. Ionic Liquid near a Charged Wall: Structure and Capacitance of Electrical Double Layer. *J. Phys. Chem. B* **2008**, *112*, 11868-11872.

(79) Feng, G.; Zhang, J. S.; Qiao, R. Microstructure and Capacitance of the Electrical Double Layers at the Interface of Ionic Liquids and Planar Electrodes. *J. Phys. Chem. C* **2009**, *113*, 4549-4559.

(80) May, S. Differential Capacitance of the Electric Double Layer: Mean-Field Modeling Approaches. *Current Opinion in Electrochemistry* **2019**, *13*, 125-131.

(81) Kornyshev, A. A. Double-Layer in Ionic Liquids: Paradigm Change? *J. Phys. Chem. B* **2007**, *111*, 5545-5557.

(82) Bazant, M. Z.; Kilic, M. S.; Storey, B. D.; Ajdari, A. Towards an Understanding of Induced-Charge Electrokinetics at Large Applied Voltages in Concentrated Solutions. *Adv. Colloid Interface Sci.* **2009**, *152*, 48-88.

(83) Giri, N.; Del Popolo, M. G.; Melaugh, G.; Greenaway, R. L.; Ratzke, K.; Koschine, T.; Pison, L.; Gomes, M. F. C.; Cooper, A. I.; James, S. L. Liquids with Permanent Porosity. *Nature* **2015**, *527*, 216-220.

(84) Szostak, R. *Molecular Sieves: Principles of Synthesis and Identification*; Springer: Cambridge, U.K., 1989.

(85) Zhou, H. C.; Long, J. R.; Yaghi, O. M. Introduction to Metal-Organic Frameworks. *Chem. Rev.* **2012**, *112*, 673-674.

(86) Simon, P.; Gogotsi, Y. Materials for Electrochemical Capacitors. *Nat Mater* **2008**, *7*, 845-854.

(87) Tozawa, T.; Jones, J. T. A.; Swamy, S. I.; Jiang, S.; Adams, D. J.; Shakespeare, S.; Clowes, R.; Bradshaw, D.; Hasell, T.; Chong, S. Y.; Tang, C.; Thompson, S.; Parker, J.; Trewin, A.; Bacsa, J.; Slawin, A. M. Z.; Steiner, A.; Cooper, A. I. Porous Organic Cages. *Nat. Mater.* **2009**, *8*, 973-978.

(88) Hasell, T.; Zhang, H. F.; Cooper, A. I. Solution-Processable Molecular Cage Micropores for Hierarchically Porous Materials. *Adv. Mater.* **2012**, *24*, 5732-5737.

(89) Brutschy, M.; Schneider, M. W.; Mastalerz, M.; Waldvogel, S. R. Porous Organic Cage Compounds as Highly Potent Affinity Materials for Sensing by Quartz Crystal Microbalances. *Adv. Mater.* **2012**, *24*, 6049-6052.

(90) O'Reilly, N.; Giri, N.; James, S. L. Porous Liquids. *Chemistry-a European Journal* **2007**, *13*, 3020-3025.

(91) Giri, N.; Davidson, C. E.; Melaugh, G.; Del Popolo, M. G.; Jones, J. T. A.; Hasell, T.; Cooper, A. I.; Horton, P. N.; Hursthouse, M. B.; James, S. L. Alkylated Organic Cages: From Porous Crystals to Neat Liquids. *Chemical Science* **2012**, *3*, 2153-2157.

(92) Mastalerz, M. Liquefied Molecular Holes. *Nature* **2015**, *527*, 174-176.

(93) Fedorov, M. V.; Kornyshev, A. A. Ionic Liquids at Electrified Interfaces. *Chem. Rev.* **2014**, *114*, 2978-3036.

(94) Hayes, R.; Warr, G. G.; Atkin, R. Structure and Nanostructure in Ionic Liquids. *Chem. Rev.* **2015**, *115*, 6357-6426.

(95) Atkin, R.; Warr, G. G. Structure in Confined Room-Temperature Ionic Liquids. *J. Phys. Chem. C* **2007**, *111*, 5162-5168.

(96) Hayes, R.; Borisenko, N.; Tam, M. K.; Howlett, P. C.; Endres, F.; Atkin, R. Double Layer Structure of Ionic Liquids at the Au(111) Electrode Interface: An Atomic Force Microscopy Investigation. *J. Phys. Chem. C* **2011**, *115*, 6855-6863.

(97) Segura, J. J.; Elbourne, A.; Wanless, E. J.; Warr, G. G.; Voitchovsky, K.; Atkin, R. Adsorbed and near Surface Structure of Ionic Liquids at a Solid Interface. *Phys. Chem. Chem. Phys.* **2013**, *15*, 3320-3328.

(98) Deyko, A.; Cremer, T.; Rietzler, F.; Perkin, S.; Crowhurst, L.; Welton, T.; Steinruck, H. P.; Maier, F. Interfacial Behavior of Thin Ionic Liquid Films on Mica. *J. Phys. Chem. C* **2013**, *117*, 5101-5111.

(99) Griffin, L. R.; Browning, K. L.; Clarke, S. M.; Smith, A. M.; Perkin, S.; Skoda, M. W. A.; Norman, S. E. Direct Measurements of Ionic Liquid Layering at a Single Mica-Liquid Interface and in Nano-Films between Two Mica-Liquid Interfaces. *Phys. Chem. Chem. Phys.* **2017**, *19*, 297-304.

(100) Gebbie, M. A.; Dobbs, H. A.; Valtiner, M.; Israelachvili, J. N. Long-Range Electrostatic Screening in Ionic Liquids. *Proc. Natl. Acad. Sci. U.S.A.* **2015**, *112*, 7432-7437.

(101) Cheng, H. W.; Stock, P.; Moeremans, B.; Baimpos, T.; Banquy, X.; Renner, F. U.; Valtiner, M. Characterizing the Influence of Water on Charging and Layering at Electrified Ionic-Liquid/Solid Interfaces. *Adv. Mater. Interfaces* **2015**, *2*, 1500159.

(102) Cheng, H. W.; Dienemann, J. N.; Stock, P.; Merola, C.; Chen, Y. J.; Valtiner, M. The Effect of Water and Confinement on Self-Assembly of Imidazolium Based Ionic Liquids at Mica Interfaces. *Sci. Rep.* **2016**, *6*, 30058.

(103) Liu, L.; Li, S.; Cao, Z.; Peng, Y. X.; Li, G. R.; Yan, T. Y.; Gao, X. P. Well-Ordered Structure at Ionic Liquid/Rutile (110) Interface. *J. Phys. Chem. C* **2007**, *111*, 12161-12164.

(104) Wang, S.; Li, S.; Cao, Z.; Yan, T. Y. Molecular Dynamic Simulations of Ionic Liquids at Graphite Surface. *J. Phys. Chem. C* **2010**, *114*, 990-995.

(105) Friedl, J.; Markovits, I. I. E.; Herpich, M.; Feng, G.; Kornyshev, A. A.; Stimming, U. Interface between an Au(111) Surface and an Ionic Liquid: The Influence of Water on the Double-Layer Capacitance. *Chemelectrochem* **2017**, *4*, 216-220.

(106) Lee, A. A.; Perez-Martinez, C. S.; Smith, A. M.; Perkin, S. Underscreening in Concentrated Electrolytes. *Faraday Discuss.* **2017**, *199*, 239-259.

(107) Shim, Y.; Jung, Y.; Kim, H. J. Graphene-Based Supercapacitors: A Computer Simulation Study. *J. Phys. Chem. C* **2011**, *115*, 23574-23583.

(108) Shim, Y.; Kim, H. J.; Jung, Y. Graphene-Based Supercapacitors in the Parallel-Plate Electrode Configuration: Ionic Liquids Versus Organic Electrolytes. *Faraday Discuss.* **2012**, *154*, 249-263.

(109) Li, S.; Feng, G.; Cummings, P. T. Interfaces of Dicationic Ionic Liquids and Graphene: A Molecular Dynamics Simulation Study. *J. Phys. Condens. Matter* **2014**, *26*, 284106.

(110) Uysal, A.; Zhou, H.; Feng, G.; Lee, S. S.; Li, S.; Fenter, P.; Cummings, P. T.; Fulvio, P. F.; Dai, S.; McDonough, J. K.; Gogotsi, Y. Structural Origins of Potential Dependent Hysteresis at the Electrified Graphene/Ionic Liquid Interface. *J. Phys. Chem. C* **2014**, *118*, 569-574.

(111) Tazi, S.; Salanne, M.; Simon, C.; Tury, P.; Pounds, M.; Madden, P. A. Potential-Induced Ordering Transition of the Adsorbed Layer at the Ionic Liquid/Electrified Metal Interface. *J. Phys. Chem. B* **2010**, *114*, 8453-8459.

(112) Merlet, C.; Rotenberg, B.; Madden, P. A.; Salanne, M. Computer Simulations of Ionic Liquids at Electrochemical Interfaces. *Phys. Chem. Chem. Phys.* **2013**, *15*, 15781-15792.

(113) Merlet, C.; Salanne, M.; Rotenberg, B.; Madden, P. A. Imidazolium Ionic Liquid Interfaces with Vapor and Graphite: Interfacial Tension and Capacitance from Coarse-Grained Molecular Simulations. *J. Phys. Chem. C* **2011**, *115*, 16613-16618.

(114) Fedorov, M. V.; Lynden-Bell, R. M. Probing the Neutral Graphene-Ionic Liquid Interface: Insights from Molecular Dynamics Simulations. *Phys. Chem. Chem. Phys.* **2012**, *14*, 2552-2556.

(115) Jiang, J.; Cao, D. P.; Jiang, D. E.; Wu, J. Z. Kinetic Charging Inversion in Ionic Liquid Electric Double Layers. *J. Phys. Chem. Lett.* **2014**, *5*, 2195-2200.

(116) Jiang, D. E.; Meng, D.; Wu, J. Z. Density Functional Theory for Differential Capacitance of Planar Electric Double Layers in Ionic Liquids. *Chem. Phys. Lett.* **2011**, *504*, 153-158.

(117) Wu, J. Z.; Jiang, T.; Jiang, D. E.; Jin, Z. H.; Henderson, D. A Classical Density Functional Theory for Interfacial Layering of Ionic Liquids. *Soft Matter* **2011**, *7*, 11222-11231.

(118) Wasserscheid, P.; Welton, T. *Ionic Liquids in Synthesis*; Wiley Online Library: New York, 2003.

(119) Yu, Z.; Wu, H. Y.; Qiao, R. Electrical Double Layers near Charged Nanorods in Mixture Electrolytes. *J. Phys. Chem. C* **2017**, *121*, 9454-9461.

(120) Feng, G.; Jiang, X. K.; Qiao, R.; Kornyshev, A. A. Water in Ionic Liquids at Electrified Interfaces: The Anatomy of Electrosorption. *Acs Nano* **2014**, *8*, 11685-11694.

(121) Fajardo, O. Y.; Bresme, F.; Kornyshev, A. A.; Urbakh, M. Water in Ionic Liquid Lubricants: Friend and Foe. *Acs Nano* **2017**, *11*, 6825-6831.

(122) Docampo-Alvarez, B.; Gomez-Gonzalez, V.; Montes-Campos, H.; Otero-Mato, J. M.; Mendez-Morales, T.; Cabeza, O.; Gallego, L. J.; Lynden-Bell, R. M.; Ivanistsev, V. B.; Fedorov, M. V.; Varela, L. M. Molecular Dynamics Simulation of the Behaviour of Water in Nano-Confined Ionic Liquid-Water Mixtures. *J. Phys. Condens. Matter* **2016**, *28*, 464001.

(123) Cui, T.; Lahiri, A.; Carstens, T.; Borisenko, N.; Pulletikurthi, G.; Kuhl, C.; Endres, F. Influence of Water on the Electrified Ionic Liquid/Solid Interface: A Direct Observation of the Transition from a Multilayered Structure to a Double-Layer Structure. *J. Phys. Chem. C* **2016**, *120*, 9341-9349.

(124) Zhong, Y. X.; Yan, J. W.; Li, M. G.; Chen, L.; Mao, B. W. The Electric Double Layer in an Ionic Liquid Incorporated with Water Molecules: Atomic Force Microscopy Force Curve Study. *Chemelectrochem* **2016**, *3*, 2221-2226.

(125) Zhang, H.; Zhu, M.; Zhao, W.; Li, S.; Feng, G. Molecular Dynamics Study of Room Temperature Ionic Liquids with Water at Mica Surface. *Green Energy Environ.* **2017**, *doi.org/10.1016/j.gee.2017.11.002*.

(126) Anaredy, R. S.; Lucio, A. J.; Shaw, S. K. Adventitious Water Sorption in a Hydrophilic and a Hydrophobic Ionic Liquid: Analysis and Implications. *Acs Omega* **2016**, *1*, 407-416.

(127) McDonald, S.; Elbourne, A.; Warr, G. G.; Atkin, R. Metal Ion Adsorption at the Ionic Liquid-Mica Interface. *Nanoscale* **2016**, *8*, 906-914.

(128) Gong, X.; Kozbial, A.; Li, L. What Causes Extended Layering of Ionic Liquids on the Mica Surface? *Chemical Science* **2015**, *6*, 3478-3482.

(129) Kornyshev, A. A.; Qiao, R. Three-Dimensional Double Layers. *J. Phys. Chem. C* **2014**, *118*, 18285-18290.

(130) Perkin, S.; Crowhurst, L.; Niedermeyer, H.; Welton, T.; Smith, A. M.; Gosvami, N. N. Self-Assembly in the Electrical Double Layer of Ionic Liquids. *Chem. Commun.* **2011**, *47*, 6572-6574.

(131) Merlet, C.; Limmer, D. T.; Salanne, M.; van Roij, R.; Madden, P. A.; Chandler, D.; Rotenberg, B. The Electric Double Layer Has a Life of Its Own. *J. Phys. Chem. C* **2014**, *118*, 18291-18298.

(132) Ivaništšev, V.; Fedorov, M. V. Interfaces between Charged Surfaces and Ionic Liquids: Insights from Molecular Simulations. *The Electrochemical Society Interface* **2014**, *23*, 65-69.

(133) Kirchner, K.; Kirchner, T.; Ivanistsev, V.; Fedorov, M. V. Electrical Double Layer in Ionic Liquids: Structural Transitions from Multilayer to Monolayer Structure at the Interface. *Electrochim. Acta* **2013**, *110*, 762-771.

(134) Song, Y.; Johnson, D.; Peng, R.; Hensley, D. K.; Bonnesen, P. V.; Liang, L. B.; Huang, J. S.; Yang, F. C.; Zhang, F.; Qiao, R.; Baddorf, A. P.; Tschaplinski, T. J.; Engle, N. L.; Hatzell, M. C.; Wu, Z. L.; Cullen, D. A.; Meyer, H. M.; Sumpter, B. G.; Rondinone, A. J. A Physical Catalyst for the Electrolysis of Nitrogen to Ammonia. *Science Advances* **2018**, *4*.

(135) Bratko, D.; Luzar, A. Attractive Surface Force in the Presence of Dissolved Gas: A Molecular Approach. *Langmuir* **2008**, *24*, 1247-1253.

(136) Lee, J.; Aluru, N. R. Mechanistic Analysis of Gas Enrichment in Gas-Water Mixtures near Extended Surfaces. *J. Phys. Chem. C* **2011**, *115*, 17495-17502.

(137) Chandler, D. Interfaces and the Driving Force of Hydrophobic Assembly. *Nature* **2005**, *437*, 640-647.

(138) Wright, P. A. *Microporous Framework Solids*; Royal Society of Chemistry: New York, 2008.

(139) Jorgensen, W. L.; Maxwell, D. S.; TiradoRives, J. Development and Testing of the Opls All-Atom Force Field on Conformational Energetics and Properties of Organic Liquids. *J. Am. Chem. Soc.* **1996**, *118*, 11225-11236.

(140) Harris, J. G.; Yung, K. H. Carbon Dioxides Liquid-Vapor Coexistence Curve and Critical Properties as Predicted by a Simple Molecular Model. *J. Phys. Chem.* **1995**, *99*, 12021-12024.

(141) Potoff, J. J.; Siepmann, J. I. Vapor-Liquid Equilibria of Mixtures Containing Alkanes, Carbon Dioxide, and Nitrogen. *AlChE J.* **2001**, *47*, 1676-1682.

(142) Liu, B.; Smit, B. Comparative Molecular Simulation Study of Co2/N-2 and Ch4/N-2 Separation in Zeolites and Metal-Organic Frameworks. *Langmuir* **2009**, *25*, 5918-5926.

(143) Hess, B.; Kutzner, C.; van der Spoel, D.; Lindahl, E. Gromacs 4: Algorithms for Highly Efficient, Load-Balanced, and Scalable Molecular Simulation. *Journal of Chemical Theory and Computation* **2008**, *4*, 435-447.

(144) Hess, B.; Bekker, H.; Berendsen, H. J. C.; Fraaije, J. G. E. M. Lincs: A Linear Constraint Solver for Molecular Simulations. *J Comput Chem* **1997**, *18*, 1463-1472.

(145) Martinez, L.; Andrade, R.; Birgin, E. G.; Martinez, J. M. Packmol: A Package for Building Initial Configurations for Molecular Dynamics Simulations. *J. Comput. Chem.* **2009**, *30*, 2157-2164.

(146) Goursot, A.; Papai, I.; Vasilyev, V.; Fajula, F., Modeling of Adsorption Properties of Zeolites. In *Zeolites: A Refined Tool for Designing Catalytic Sites*, Bonneviot, L.; Kaliaguine, S., Eds. Elsevier Science, Québec, Canada, 1995, 109-116.

(147) Yamada, M.; Arai, M.; Kurihara, M.; Sakamoto, M.; Miyake, M. Synthesis and Isolation of Cobalt Hexacyanoferrate/Chromate Metal Coordination Nanopolymers Stabilized by Alkylamino Ligand with Metal Elemental Control. *J. Am. Chem. Soc.* **2004**, *126*, 9482-9483.

(148) Devaux, A.; Popovic, Z.; Bossart, O.; De Cola, L.; Kunzmann, A.; Calzaferri, G. Solubilisation of Dye-Loaded Zeolite L Nanocrystals. *Microporous Mesoporous Mater.* **2006**, *90*, 69-72.

(149) Atwood, J. L.; Barbour, L. J.; Jerga, A.; Schottel, B. L. Guest Transport in a Nonporous Organic Solid Via Dynamic Van Der Waals Cooperativity. *Science* **2002**, *298*, 1000-1002.

(150) Melaugh, G.; Giri, N.; Davidson, C. E.; James, S. L.; Del Popolo, M. G. Designing and Understanding Permanent Microporosity in Liquids. *Phys. Chem. Chem. Phys.* **2014**, *16*, 9422-9431.

(151) Zhang, J. S.; Chai, S. H.; Qiao, Z. A.; Mahurin, S. M.; Chen, J. H.; Fang, Y. X.; Wan, S.; Nelson, K.; Zhang, P. F.; Dai, S. Porous Liquids: A Promising Class of Media for Gas Separation. *Angew. Chem. Int. Ed.* **2015**, *54*, 932-936.

(152) Holst, J. R.; Trewin, A.; Cooper, A. I. Porous Organic Molecules. *Nature Chemistry* **2010**, *2*, 915-920.

(153) Reiss, P. S.; Little, M. A.; Santolini, V.; Chong, S. Y.; Hasell, T.; Jelfs, K. E.; Briggs, M. E.; Cooper, A. I. Periphery-Functionalized Porous Organic Cages. *Chemistry-a European Journal* **2016**, *22*, 16547-16553.

(154) Hasell, T.; Cooper, A. I. Porous Organic Cages: Soluble, Modular and Molecular Pores. *Nature Reviews Materials* **2016**, *1*, 16053.

(155) Zhu, G. H.; Hoffman, C. D.; Liu, Y.; Bhattacharyya, S.; Tumuluri, U.; Jue, M. L.; Wu, Z. L.; Sholl, D. S.; Nair, S.; Jones, C. W.; Lively, R. P. Engineering Porous Organic Cage Crystals with Increased Acid Gas Resistance. *Chemistry-a European Journal* **2016**, *22*, 10743-10747.

(156) Greenaway, R. L.; Holden, D.; Eden, E. G. B.; Stephenson, A.; Yong, C. W.; Bennison, M. J.; Hasell, T.; Briggs, M. E.; James, S. L.; Cooper, A. I. Understanding Gas Capacity, Guest Selectivity, and Diffusion in Porous Liquids. *Chemical Science* **2017**.

(157) Zhang, F.; Yang, F. C.; Huang, J. S.; Sumpter, B. G.; Qiao, R. Thermodynamics and Kinetics of Gas Storage in Porous Liquids. *J. Phys. Chem. B* **2016**, *120*, 7195-7200.

(158) Goodbody, S. J.; Watanabe, K.; Macgowan, D.; Walton, J. P. R. B.; Quirke, N. Molecular Simulation of Methane and Butane in Silicalite. *Journal of the Chemical Society-Faraday Transactions* **1991**, *87*, 1951-1958.

(159) Maitland, G. C.; Rigby, M.; Smith, E. B.; Wakeham, W. A. *Intermolecular Forces : Their Origin and Determination*; Clarendon Press: Oxford, U.K., 1981.

(160) Katagiri, T.; Takahashi, S.; Tanaka, Y.; Kawabata, K.; Hattori, Y.; Kaneko, K.; Uneyama, K. Gas Storage in Soft 1d Nano-Tunnels by the Induced Fit of a Serration Structure. *Crystengcomm* **2009**, *11*, 347-350.

(161) Liu, B.; Smit, B. Comparative Molecular Simulation Study of Co-2/N-2 and Ch-4/N-2 Separation in Zeolites and Metal-Organic Frameworks. *Langmuir* **2009**, *25*, 5918-5926.

(162) Hess, B.; Bekker, H.; Berendsen, H. J. C.; Fraaije, J. G. E. M. Lincs: A Linear Constraint Solver for Molecular Simulations. *J. Comput. Chem.* **1997**, *18*, 1463-1472.

(163) Talbot, J. Analysis of Adsorption Selectivity in a One-Dimensional Model System. *AlChE J.* **1997**, *43*, 2471-2478.

(164) Du, Z. M.; Manos, G.; Vlugt, T. J. H.; Smit, B. Molecular Simulation of Adsorption of Short Linear Alkanes and Their Mixtures in Silicalite. *AlChE J.* **1998**, *44*, 1756-1764.

(165) Bazant, M. Z.; Storey, B. D.; Kornyshev, A. A. Double Layer in Ionic Liquids: Overscreening Versus Crowding. *Phys. Rev. Lett.* **2011**, *106*, 046102.

(166) Ho, T. A. Water and Methane in Shale Rocks: Flow Pattern Effects on Fluid Transport and Pore Structure. *Nanoscale Fluid Transport: From Molecular Signatures to Applications* **2017**, 53-64.

(167) Malani, A.; Ayappa, K. G. Adsorption Isotherms of Water on Mica: Redistribution and Film Growth. *J. Phys. Chem. B* **2009**, *113*, 1058-1067.

(168) Heinz, H.; Koerner, H.; Anderson, K. L.; Vaia, R. A.; Farmer, B. L. Force Field for Mica-Type Silicates and Dynamics of Octadecylammonium Chains Grafted to Montmorillonite. *Chem. Mater.* **2005**, *17*, 5658-5669.

(169) Heinz, H.; Suter, U. W. Atomic Charges for Classical Simulations of Polar Systems. *J. Phys. Chem. B* **2004**, *108*, 18341-18352.

(170) Xu, Y.; Liu, Y. L.; Gao, S.; Jiang, Z. W.; Su, D.; Liu, G. S. Monolayer Adsorption of Dodecylamine Surfactants at the Mica/Water Interface. *Chem. Eng. Sci.* **2014**, *114*, 58-69.

(171) Vatamanu, J.; Borodin, O.; Bedrov, D.; Smith, G. D. Molecular Dynamics Simulation Study of the Interfacial Structure and Differential Capacitance of Alkylimidazolium Bis(Trifluoromethanesulfonyl)Imide [Cnmim][Tfsi] Ionic Liquids at Graphite Electrodes. *J. Phys. Chem. C* **2012**, *116*, 7940-7951.

(172) Plimpton, S. Fast Parallel Algorithms for Short-Range Molecular-Dynamics. *J. Comput. Phys.* **1995**, *117*, 1-19.

(173) Evans, D. J.; Holian, B. L. The Nose-Hoover Thermostat. *J. Chem. Phys.* **1985**, *83*, 4069-4074.

(174) Hockney, R. W.; Eastwood, J. W. *Computer Simulation Using Particles*; crc Press: 1988.

(175) Li, H.; Endres, F.; Atkin, R. Effect of Alkyl Chain Length and Anion Species on the Interfacial Nanostructure of Ionic Liquids at the Au(111)-Ionic Liquid Interface as a Function of Potential. *Phys. Chem. Chem. Phys.* **2013**, *15*, 14624-14633.

(176) Black, J. M.; Walters, D.; Labuda, A.; Feng, G.; Hillesheim, P. C.; Dai, S.; Cummings, P. T.; Kalinin, S. V.; Proksch, R.; Balke, N. Bias-Dependent Molecular-Level Structure of Electrical Double Layer in Ionic Liquid on Graphite. *Nano Lett.* **2013**, *13*, 5954-5960.

(177) Perkin, S. Ionic Liquids in Confined Geometries. *Phys. Chem. Chem. Phys.* **2012**, *14*, 5052-5062.

(178) Mezger, M.; Schroder, H.; Reichert, H.; Schramm, S.; Okasinski, J. S.; Schoder, S.; Honkimaki, V.; Deutsch, M.; Ocko, B. M.; Ralston, J.; Rohwerder, M.; Stratmann, M.; Dosch, H.

Molecular Layering of Fluorinated Ionic Liquids at a Charged Sapphire (0001) Surface. *Science* **2008**, *322*, 424-428.

(179) Fedorov, M. V.; Georgi, N.; Kornyshev, A. A. Double Layer in Ionic Liquids: The Nature of the Camel Shape of Capacitance. *Electrochem. Commun.* **2010**, *12*, 296-299.

(180) Georgi, N.; Kornyshev, A. A.; Fedorov, M. V. The Anatomy of the Double Layer and Capacitance in Ionic Liquids with Anisotropic Ions Electrostriction Vs Lattice Saturation. *J. Electroanal. Chem.* **2010**, *649*, 261-267.

(181) Wang, Y.; Jiang, W.; Yan, T.; Voth, G. A. Understanding Ionic Liquids through Atomistic and Coarse-Grained Molecular Dynamics Simulations. *Acc. Chem. Res.* **2007**, *40*, 1193-1199.

(182) Yang, R. T. *Gas Separation by Adsorption Processes*; Butterworths: Boston, 1987.

(183) Rouquerol, F.; Rouquerol, J.; Sing, K. S. W.; Llewellyn, P. L.; Maurin, G. *Adsorption by Powders and Porous Solids : Principles, Methodology and Applications*; Second edition. ed.; Elsevier Academic Press: Amsterdam, 2014; p xix, 626 pages.

(184) Li, J. R.; Kuppler, R. J.; Zhou, H. C. Selective Gas Adsorption and Separation in Metal-Organic Frameworks. *Chem. Soc. Rev.* **2009**, *38*, 1477-1504.

(185) Woodruff, D. P. *The Solid-Liquid Interface*; Cambridge University Press: London, 1973.

(186) Dammer, S. M.; Lohse, D. Gas Enrichment at Liquid-Wall Interfaces. *Phys. Rev. Lett.* **2006**, *96*.

(187) Paria, S.; Khilar, K. C. A Review on Experimental Studies of Surfactant Adsorption at the Hydrophilic Solid-Water Interface. *Adv. Colloid Interface Sci.* **2004**, *110*, 75-95.

(188) Torrie, G. M.; Valleau, J. P. Non-Physical Sampling Distributions in Monte-Carlo Free-Energy Estimation - Umbrella Sampling. *J. Comput. Phys.* **1977**, *23*, 187-199.

(189) Torrie, G. M.; Valleau, J. P. Monte-Carlo Free-Energy Estimates Using Non-Boltzmann Sampling - Application to Subcritical Lennard-Jones Fluid. *Chem. Phys. Lett.* **1974**, *28*, 578-581.

(190) Kumar, S.; Bouzida, D.; Swendsen, R. H.; Kollman, P. A.; Rosenberg, J. M. The Weighted Histogram Analysis Method for Free-Energy Calculations on Biomolecules .1. The Method. *J. Comput. Chem.* **1992**, *13*, 1011-1021.

(191) Israelachvili, J. N., Intermolecular and Surface Forces. 3rd ed.; Academic Press,: New York, 2015.

(192) Berendsen, H. J. C.; Grigera, J. R.; Straatsma, T. P. The Missing Term in Effective Pair Potentials. *J. Phys. Chem.* **1987**, *91*, 6269-6271.

(193) Gee, M. B.; Cox, N. R.; Jiao, Y. F.; Bentenitis, N.; Weerasinghe, S.; Smith, P. E. A Kirkwood-Buff Derived Force Field for Aqueous Alkali Halides. *Journal of Chemical Theory and Computation* **2011**, *7*, 1369-1380.

(194) Darden, T.; York, D.; Pedersen, L. Particle Mesh Ewald - an N.Log(N) Method for Ewald Sums in Large Systems. *J. Chem. Phys.* **1993**, *98*, 10089-10092.

(195) Hub, J. S.; de Groot, B. L.; van der Spoel, D. G_Wham-a Free Weighted Histogram Analysis Implementation Including Robust Error and Autocorrelation Estimates. *Journal of Chemical Theory and Computation* **2010**, *6*, 3713-3720.

(196) Neumann, R. M. Entropic Approach to Brownian-Movement. *Am. J. Phys.* **1980**, *48*, 354-357.

(197) Sokolov, S. V.; Katelhon, E.; Compton, R. G. Near-Wall Hindered Diffusion in Convective Systems: Transport Limitations in Colloidal and Nanoparticulate Systems. *J. Phys. Chem. C* **2016**, *120*, 10629-10640.

(198) Beskok, A.; Karniadakis, G. E.; Aluru, N. R. *Microflows and Nanoflows - Fundamentals and Simulation*; Springer Science: New York, 2005.

(199) Jiang, D.-e.; Jin, Z.; Wu, J. Oscillation of Capacitance inside Nanopores. *Nano Letters* **2011**, *11*, 5373-5377.

(200) Yu, Z.; Zhang, F.; Huang, J. S.; Sumpter, B. G.; Qiao, R. Ionic Liquids-Mediated Interactions between Nanorods. *J. Chem. Phys.* **2017**, *147*.

(201) The Structure of Liquid Water at an Extended Hydrophobic Surface. *The Journal of Chemical Physics* **1984**, *80*, 4448-4455.

(202) Janeček, J.; Netz, R. R. Interfacial Water at Hydrophobic and Hydrophilic Surfaces: Depletion Versus Adsorption. *Langmuir* **2007**, *23*, 8417-8429.

(203) Qiao, R.; Aluru, N. R. Atomistic Simulation of Kcl Transport in Charged Silicon Nanochannels: Interfacial Effects. *Colloids and Surfaces A: Physicochemical and Engineering Aspects* **2005**, *267*, 103-109.

(204) Song, Y.; Peng, R.; Hensley, D. K.; Bonnesen, P. V.; Liang, L. B.; Wu, Z. L.; Meyer, H. M.; Chi, M. F.; Ma, C.; Sumpter, B. G.; Rondinone, A. J. High-Selectivity Electrochemical Conversion of Co2 to Ethanol Using a Copper Nanoparticle/N-Doped Graphene Electrode. *Chemistryselect* **2016**, *1*, 6055-6061.

(205) Bartels, C. Analyzing Biased Monte Carlo and Molecular Dynamics Simulations. *Chem. Phys. Lett.* **2000**, *331*, 446-454.